Light and Mass Distribution of Pairs of Galaxy Clusters

Diplomarbeit

im Fach Physik

von

Jörg Peter Dietrich

angefertigt am
Institut für Astrophysik und extraterrestrische Forschung

vorgelegt der
Mathematisch–Naturwissenschaftlichen Fakultät
der
Rheinischen Friedrich–Wilhelms–Universität
Bonn

im Mai 2002

Light and Mass Distribution of Pairs of Galaxy Clusters

Jörg Peter Dietrich

Ich versichere, daß ich diese Arbeit selbständig verfaßt, keine anderen als die angegebenen Hilfsmittel verwendet und Zitate kenntlich gemacht habe.

Referent: Prof. Dr. Peter Schneider
Koreferent: Prof. Dr. Johannes Schmid–Burgk

Mai 2002

Light and Mass Distribution of Pairs of Galaxy Clusters

Diplomarbeit

im Fach Physik

von

Jörg Peter Dietrich

angefertigt am
Institut für Astrophysik und extraterrestrische Forschung

vorgelegt der
Mathematisch–Naturwissenschaftlichen Fakultät
der
Rheinischen Friedrich–Wilhelms–Universität
Bonn

im Mai 2002

Contents

Chapter 1

Introduction

The theory of cosmic structure formation predicts through n–body simulations that matter in the universe should be concentrated along sheets and filaments and that clusters of galaxies form where these intersect (Kauffmann et al. 1999; Bond et al. 1996). This filamentary structure, often also dubbed "cosmic web", has been seen in galaxy redshift surveys (Vogeley et al. 1994) and more recently and at higher redshift by Möller & Fynbo (2001). Because of the greatly varying mass–to–light (M/L) ratios between rich clusters and groups of galaxies (Tully & Shaya 1998) it is problematic to convert the measured galaxy densities to mass densities without making further assumptions. Dynamical and X–ray measurements of the filament mass will not yield accurate values, as filamentary structures are probably not virialized. Weak gravitational lensing, which is based on the measurement of shape and orientation parameters of faint background galaxies (FBG), is a model–independent method to determine the surface mass density of clusters and filaments. Due to the random orientation of the unlensed FBG every weak lensing mass reconstruction is unfortunately an inherently noisy process, and the expected surface mass density of a single filament is too low to be detected with current telescopes (Jain et al. 2000).

Cosmic web theory also predicts that the surface mass density of a filament increases towards a cluster (Bond et al. 1996). Filaments connecting neighboring clusters should have surface mass densities high enough to be detectable with weak lensing (Pogosyan et al. 1998). Such filaments may have been detected in several recent weak lensing studies.

Kaiser et al. (1998) found a possible filament between two of the three cluster in the $z = 0.42$ supercluster MS0302+17, but the detection remains somewhat uncertain because of a possible foreground structure overlapping the filament and possible edge effects due to the gap between two of the camera chips lying on the filament. Gray et al. (2002) claim to have found a filament extending between two of the three clusters of the Abell 901/902 supercluster, but the significance of this detection is low and subject to possible edge effects, as again the filament is on the gap between two chips of the camera. Clowe et al. (1998) reported the detection of a filament extending from a high-redshift ($z = 0.809$) cluster. Due to the small size of the image it is unknown whether this filament extends to a nearby cluster.

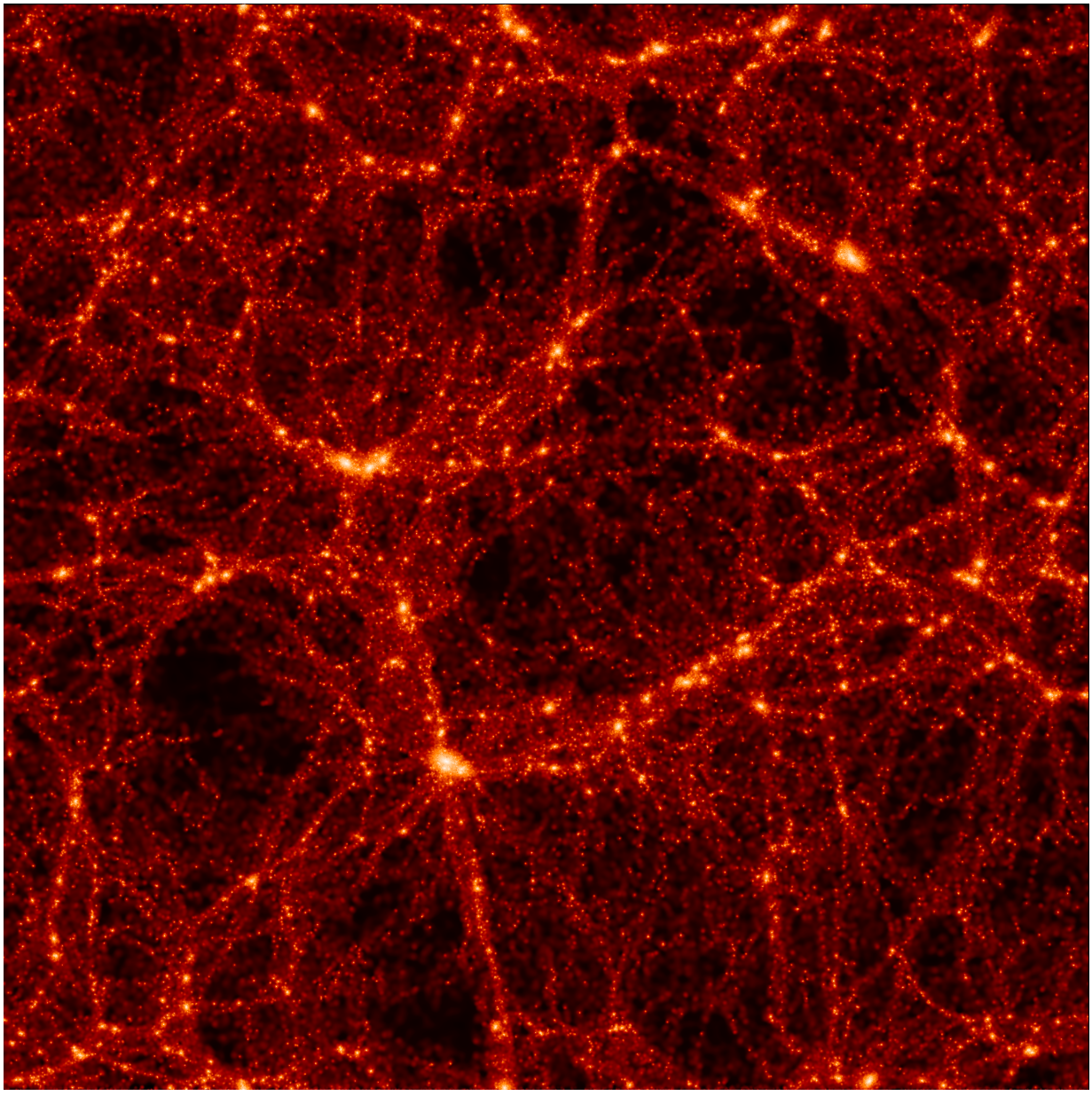

Figure 1.1: N–body simulation showing the cosmic web of sheets and filaments. Taken from `http://www.mpa-garching.mpg.de/Virgo/LCDM.gif` (Jenkins et al. 1998).

A significant detection of a filament between clusters of galaxies and the determination of its surface mass density would be an important step in observational cosmology and would provide important constraints for the theory of structure formation.

This thesis consists of several parts. I start with a brief review of the basics of gravitational lens theory and mass reconstructions in chapter 2. In chapter 3 I try to develop a statistics based on weak gravitational lensing to quantify the presence of a filament between a pair of galaxy clusters using the results of n–body simulations. Although mostly unsuccessful, some results of this chapter are applied to observational data of the Abell 222 and Abell 223 clusters. This and various other weak lensing analyses are presented in chapter 5. A spectroscopic and photometric study of the Abell clusters is described in chapter 4. A discussion of the results of this thesis and their implications for future studies in this field is given in chapter 6.

Chapter 2

Gravitational Lensing

Although already Newton discussed the deflection of a light ray traversing the gravitational field of a massive body, a definite answer to the question whether and how much such a light ray would be deflected could only be given after Einstein developed his *General Theory of Relativity* (GRT). The prediction of GRT that light is indeed deflected when traversing an inhomogeneous gravitational field was confirmed in 1920 by Dyson et al. (1920) who measured the shift of position of stars close to the sun during a solar eclipse. The measurement confirmed not only the existence of a gravitational light deflection but also the value predicted by Einstein's theory which is twice as big as predicted from Newtonian theory. The first gravitational lens on cosmological scales was found in 1979 by Walsh et al., who observed a double image of the quasar 0957 + 561. Since then gravitational lensing has been a flourishing field with many different applications.

In the following I will give a brief overview of the basics of gravitational lensing, and especially weak lensing and mass reconstructions from weak lensing. A much more in–depth treatment of gravitational lenses in general can be found in Schneider et al. (1992) and of weak lensing in particular in Bartelmann & Schneider (2001).

2.1 Cosmological Background

Since gravitational lensing takes place on large scales the effects of space–time curvature and expansion cannot be neglected. I will review a few of the fundamental equations and facts of the standard Friedmann–Lemaître–Robertson–Walker (FLRW) cosmological model. A thorough treatment of this subject can be found in many textbooks, e.g. Peacock (1999).

The FLRW model relies on the two fundamental postulates that (1) the matter distribution and motion is *isotropic* on sufficiently large scales and that (2) every comoving observer observes the same history of the universe. The last property is called *observer homogeneous*.

General Relativity describes space–time as a four dimensional pseudo–Riemannian manifold with a metric $g_{\alpha\beta}$ that depends on time and space. The components of the metric

tensor are determined by solving Einstein's field equations. Robertson and Walker showed that for an isotropic and homogenous universe the metric can be written in the simple form

$$\mathrm{d}s^2 = c^2\mathrm{d}t^2 - a^2(t)\mathrm{d}l^2 \,, \tag{2.1}$$

where $a(t)$ is a scale function that depends only on time because any spatial dependence would violate the requirement of homogeneity. $\mathrm{d}l^2$ is the comoving line element in three–space. The most general form to write the line element in spherical coordinates (w, θ, ϕ) fulfilling the conditions of isotropy and homogeneity is

$$\mathrm{d}l^2 = \mathrm{d}w^2 + f_K^2(w)\left(\mathrm{d}\theta^2 + \sin^2\mathrm{d}\phi^2\right) \,. \tag{2.2}$$

The functional dependence of $f_K(w)$ on the curvature K of the spatial hypersurface, described by the line element $\mathrm{d}l^2$, is given by

$$f_K(w) = \begin{cases} K^{-1/2}\sin(K^{1/2}w) & (K > 0) \,, \\ w & (K = 0) \,, \\ -(K)^{-1/2}\sinh\left[(-K)^{1/2}w\right] & (K < 0) \,. \end{cases} \tag{2.3}$$

I choose the normalization $a_0 = a(t_0) = 1$. Here and in the following any quantity with a subscript 0 denotes the value at the present epoch.

Because spacetime expands, photons traveling from a source to an observer are redshifted on their way. A photon that was emitted at time t_e and is observed today is redshifted by

$$1 + z = \frac{a_0}{a(t_\mathrm{e})} = \frac{1}{a(t_\mathrm{e})} = \frac{\lambda_\mathrm{obs}}{\lambda_\mathrm{e}} \,. \tag{2.4}$$

Here we already made use of the scale function $a(t)$ but have not yet determined how it depends on time. For the simple metric given in eq. (2.1) and (2.2) the stress–energy tensor has to have the form of a perfect fluid with density $\rho(t)$ and pressure $p(t)$. Einstein's field equations then simplify to the two independent equations

$$\left(\frac{\dot{a}}{a}\right)^2 = \frac{8\pi G\rho}{3} - \frac{Kc^2}{a^2} + \frac{\Lambda}{3} \tag{2.5}$$

and

$$\frac{\ddot{a}}{a} = -\frac{4\pi G}{3}\left(\rho + \frac{3p}{c^2}\right) + \frac{\Lambda}{3} \,, \tag{2.6}$$

which together with the normalization $a_0 = 1$ completely determine the scale function $a(t)$. Λ is called the *cosmological constant*. A universe obeying eq. (2.5) and (2.6) is called a *Friedmann–Lemaître* universe.

The geometry of an FLRW universe depends on its energy density. The *critical density* $\rho_{\rm crit}$ of the universe for matter is given by

$$\rho_{\rm crit} = \frac{3H_0^2}{8\pi G} \,. \tag{2.7}$$

and the *density parameter*

$$\Omega_{\rm m} = \frac{\rho_{\rm m}}{\rho_{\rm crit}} \tag{2.8}$$

is the density in units of the critical matter density. In case of vanishing Λ, $\Omega_0 = 1$ corresponds to a universe with flat spatial hypersurfaces ($K = 0$). This case is called *Einstein–de Sitter* (EdS) universe. Likewise we define a density parameter for the cosmological constant:

$$\Omega_\Lambda = \frac{\Lambda}{3H_0^2} \,. \tag{2.9}$$

The ratio

$$H = \frac{\dot{a}}{a} \tag{2.10}$$

is called the *Hubble parameter* and its value at the present epoch is used in the local Hubble law to determine the distance of objects (for $z \ll 1$):

$$\text{distance} = \frac{cz}{H_0} \tag{2.11}$$

The value of the *Hubble constant* H_0 is often given as $H_0 = 100\,h\,\mathrm{km\,s^{-1}Mpc^{-1}}$ with $h = (0.5 - 0.8)$ to reflect the uncertainty in the actual value of H_0.

Generally, the notion of distance is not unique in curved spacetime and the dependence of distance on redshift is more complicated than in eq. (2.11). The *angular diameter distance* relates the cross–section δA of an object to the solid angle $\delta\omega$ under which it appears,

$$D = \left(\frac{\delta A}{\delta\omega}\right)^{1/2} \,. \tag{2.12}$$

In terms of redshifts, the angular diameter distance between to objects of redshift z_1 and z_2 is given by

$$D_{\rm ang}(z_1, z_2) = a(z_2) f_K[w(z_1, z_2)] \,, \tag{2.13}$$

or can be written in terms of the density parameters as

$$D_{\rm ang}(z_1, z_2) = \frac{1}{1+z_2} \int_{z_1}^{z_2} \frac{\mathrm{d}z'}{\sqrt{(1-\Omega_{\rm m}-\Omega_\Lambda)(1+z')^2 + \Omega_{\rm m}(1+z')^3 + \Omega_\Lambda}} \,. \tag{2.14}$$

In an EdS universe with a Hubble constant H_0 (2.14) can be integrated to

$$D_{\rm ang}(z_1, z_2) = \frac{2c}{H_0\,(1+z_2)} \left[(1+z_1)^{-1/2} - (1+z_2)^{-1/2}\right] \,. \tag{2.15}$$

2.2 Basics of Gravitational Lens Theory

2.2.1 The Thin Lens Approximation

Figure 2.1 sketches a typical situation considered in gravitational lensing. A light ray emitted from a source S is deflected when it passes a gravitational lens D. The observer O sees the source at the position angle $\vec{\theta}$ instead of the undeflected position $\vec{\beta}$. The light ray is deflected by the deflection angle $\hat{\vec{\alpha}}$. Angular diameter distances are used because with them the intercept theorems are valid.

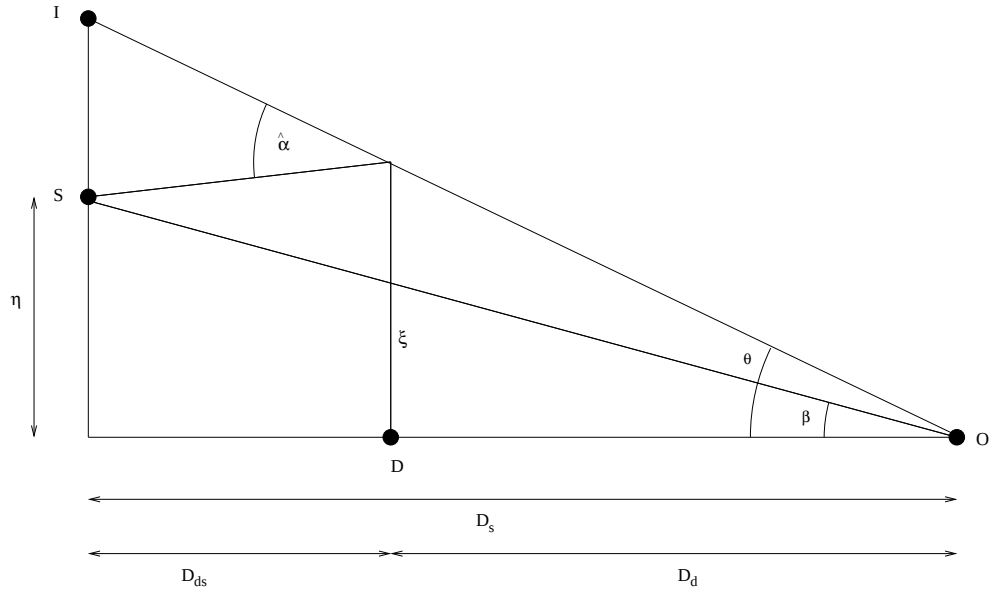

Figure 2.1: Simplified geometry of a gravitational lens system. A light ray emitted from the source S is deflected by the gravitational lens D, and observed at the position angle $\vec{\theta}$ by the observer O. $D_{\rm d}$, $D_{\rm s}$, and $D_{\rm ds}$ are the angular diameter distances from the observer to the lens, from the observer to the source, and from the deflector to the source, respectively. The vector $\vec{\eta}$ denotes the two dimensional position of the source in the source plane.

In most astrophysical cases the spatial extension of the lens along the line of sight is small compared to the travel path of the light ray and the light ray can be considered as a piecewise straight line, even in the vicinity of the lens. If we additionally require that the impact parameter is much bigger than the Schwarzschild radius of a point lens with mass M, $|\vec{\xi}| \gg 2GMc^{-2}$, the field equations of General Relativity can be linearized. The vectorial deflection angle of a lens is then the superposition of the deflection angle of the individual mass elements.

This enables us to write the deflection angle in terms of the surface mass density $\Sigma(\vec{\xi})$, which is the projection of the three–dimensional density distribution of the lens onto a

plane perpendicular to the line of sight:

$$\Sigma(\vec{\xi}) = \int \mathrm{d}r_3 \; \rho(\vec{\xi}, r_3) \; . \tag{2.16}$$

The deflection angle is then given by

$$\hat{\vec{\alpha}}(\vec{\xi}) = \frac{4G}{c^2} \int \mathrm{d}^2\xi' \; \Sigma(\vec{\xi}') \frac{\vec{\xi} - \vec{\xi}'}{|\vec{\xi} - \vec{\xi}'|^2} \; . \tag{2.17}$$

2.2.2 The Lens Equation

We now need an equation to relate the source position to the observed position. From Fig. 2.1 we see that

$$\vec{\eta} = \frac{D_\mathrm{s}}{D_\mathrm{d}} \vec{\xi} - D_\mathrm{ds} \hat{\vec{\alpha}}(\vec{\xi}) \; , \tag{2.18}$$

with the impact parameter $\vec{\xi}$. Introducing the scaled deflection angle

$$\vec{\alpha}(\vec{\theta}) = \frac{D_\mathrm{ds}}{D_\mathrm{s}} \hat{\vec{\alpha}}(D_\mathrm{d}\vec{\theta}) \; , \tag{2.19}$$

and using the relations $\vec{\eta} = D_\mathrm{s}\vec{\beta}$, $\vec{\xi} = D_\mathrm{d}\vec{\theta}$ eq. (2.18) takes the form of the lens equation,

$$\vec{\beta} = \vec{\theta} - \vec{\alpha}(\vec{\theta}) \; . \tag{2.20}$$

Depending on the surface mass density, eq. (2.20) can have multiple solutions $\vec{\theta}$ for a given $\vec{\beta}$. A lens whose surface mass density exceeds the *critical surface mass density*

$$\Sigma_\mathrm{crit} = \frac{c^2}{4\pi G} \frac{D_\mathrm{s}}{D_\mathrm{d} D_\mathrm{ds}} \; , \tag{2.21}$$

which depends on the angular diameter distances between source, lens, and observer, somewhere, will produce multiple images for some source position $\vec{\beta}$. Because the critical surface mass density is a characteristic value for any lens system, the surface mass density is often written in units of Σ_crit:

$$\kappa(\vec{\theta}) = \frac{\Sigma(D_\mathrm{d}\vec{\theta})}{\Sigma_\mathrm{crit}} \; . \tag{2.22}$$

κ is called the dimension–less surface mass density and its value gives a qualitative description of the lens. If $\kappa > 1$ for some region in the lens plane, the lens is said to be 'strong' and it can produce multiple images of the background source. If $\kappa \ll 1$ the lens is called 'weak' and cannot produce several images of a source.

Eq. (2.17) can now also be written in terms of κ

$$\vec{\alpha}(\vec{\theta}) = \frac{1}{\pi} \int \mathrm{d}^2\theta' \, \kappa(\vec{\theta}') \frac{\vec{\theta} - \vec{\theta}'}{|\vec{\theta} - \vec{\theta}'|^2} \; , \tag{2.23}$$

where we used the scaling relation (2.19). From eq. (2.23) we see that the scaled deflection angle can be written as the gradient of a two dimensional deflection potential, $\vec{\alpha} = \nabla\psi$,

$$\psi(\vec{\theta}) = \frac{1}{\pi} \int \mathrm{d}^2\theta' \, \kappa(\vec{\theta}') \ln |\vec{\theta} - \vec{\theta}'| \; . \tag{2.24}$$

In analogy to the three–dimensional Newtonian potential, ψ satisfies a Poisson equation $\nabla^2\psi(\vec{\theta}) = 2\kappa(\vec{\theta})$.

2.2.3 Properties of the Lens Mapping

Because eq. (2.20) is non–linear a gravitational lens will not only change the position of the source image, but also its shape. The local properties of the lens mapping are described by its Jacobian matrix

$$\mathcal{A} = \frac{\partial\vec{\beta}}{\partial\vec{\theta}} = \left(\delta_{ij} - \frac{\partial^2\psi(\vec{\theta})}{\partial\theta_i\theta_j} \right) = \begin{pmatrix} 1 - \kappa - \gamma_1 & -\gamma_2 \\ -\gamma_2 & 1 - \kappa + \gamma_1 \end{pmatrix} \; , \tag{2.25}$$

where in the last step we defined the complex shear $\gamma = \gamma_1 + \mathrm{i}\gamma_2 = |\gamma|\mathrm{e}^{2\mathrm{i}\varphi}$ as the trace–free part of $\mathcal{A}$, which is related to the deflection potential via

$$\gamma_1 = \frac{1}{2}(\psi_{,11} - \psi_{,22}) \; , \qquad \gamma_2 = \psi_{,12} \; . \tag{2.26}$$

Additionally, from Liouville's theorem we can conclude that gravitational lensing conserves surface brightness. Let $I^{(s)}(\vec{\beta})$ be the intensity of a source in the source plane. An observer then sees the intensity

$$I(\vec{\theta}) = I^{(s)}[\vec{\beta}(\vec{\theta})] \; , \tag{2.27}$$

which locally linearized around a point $\vec{\beta}_0 = \vec{\beta}(\vec{\theta}_0)$ becomes

$$I(\vec{\theta}) = I^{(s)} \left[\vec{\beta}_0 + \mathcal{A}(\vec{\theta}_0) \cdot (\vec{\theta} - \vec{\theta}_0) \right] \; . \tag{2.28}$$

Equation (2.28) has a geometric interpretation. Assuming a circular background source, the image will be an ellipse with semi–axes

$$\begin{aligned} a &= r \cdot (1 - \kappa - |\gamma|)^{-1} \; , \\ b &= r \cdot (1 - \kappa + |\gamma|)^{-1} \; , \end{aligned} \tag{2.29}$$

r being the radius of the unlensed background source. From eq. (2.29) we see that the convergence κ magnifies the image, while the shear γ distorts the image. The magnification factor of an image is given by computing the ratio of the integrated lensed and unlensed intensity distribution $I(\vec{\theta})$ and $I^{(s)}(\vec{\theta})$, respectively. From equation (2.28) we determine this to be

$$\mu = \frac{1}{\det \mathcal{A}} = \frac{1}{(1-\kappa)^2 - |\gamma|^2} \ . \tag{2.30}$$

Thus, not only the convergence but also the tidal distortions of the shear contribute to the magnification. We call a lens *sub–critical* if it cannot produce multiple images, i. e. $\det \mathcal{A}(\vec{\theta}) > 0, \forall\ \vec{\theta}$.

Two competing effects can change the number density of background objects by gravitational lensing. We will look at this for sub–critical lenses. First, lensing magnifies while leaving the surface brightness constant. Hence, the flux of background objects changes such that fainter objects can become visible in a flux–limited sample. Second, the magnification locally stretches the sky and thus decreases the number density of a fixed set of sources by a factor μ.

Let $n_0(> S, z)\mathrm{d}z$ be the unlensed number density of objects with redshift between z and $z + \mathrm{d}z$ and a minimum flux S. Then the observed number density is given by

$$n(> S, z) = \frac{1}{\mu(z)} n_0 \left(> \frac{S}{\mu(z)}, z \right) . \tag{2.31}$$

Generally, no redshift information for the FBG will be available and only the redshift–integrated count

$$n(> S) = \int \mathrm{d}z \ \frac{1}{\mu(z)} n_0 \left(> \frac{S}{\mu(z)}, z \right) \tag{2.32}$$

will be observed. It is known from observations that the number counts of faint galaxies closely folllow a power law,

$$n_0(> S, z) = a S^{-\alpha} p_0(z; S), \tag{2.33}$$

where the exponent α depends on the observed pass band (Smail et al. 1995), and $p_0(z; S)$ is the (currently unknown) redshift probability distribution of galaxies with flux $> S$. Combining (2.32) and (2.33) we get

$$\frac{n(> S)}{n_0(> S)} = \int \mathrm{d}z \ \mu^{\alpha-1}(z)\, p_0 \left(z; \frac{S}{\mu(z)} \right) . \tag{2.34}$$

For small lens redshifts ($z_\mathrm{d} \lesssim 0.3$) this can be approximated by

$$\frac{n(> S)}{n_0(> S)} = \mu^{\alpha-1} \ , \tag{2.35}$$

because for all background sources the redshift dependent magnifaction is approximately equal to the magnification of a fiducial source at infinity (see Bartelmann & Schneider 2001, section 4.3.2).

As κ determines the deflection potential, and the shear is given by second partial derivatives of the deflection potential, we can suspect that a relation between κ and γ exists. Combining equations (2.24) and (2.26), we find that γ can be written as the convolution of the surface mass density with a kernel $\mathcal{D}(\vec{\theta})$,

$$\begin{aligned} \gamma(\vec{\theta}) &= \frac{1}{\pi}\int \mathrm{d}^2\theta'\, \mathcal{D}(\vec{\theta}-\vec{\theta}')\kappa(\vec{\theta}')\ , \\ \mathcal{D}(\vec{\theta}) &= \frac{\theta_2^2-\theta_1^2-2\mathrm{i}\theta_1\theta_2}{|\theta|^4} = \frac{-1}{(\theta_1-\mathrm{i}\theta_2)^2}\ . \end{aligned} \tag{2.36}$$

Equation (2.36) implies that by Fourier–transforming and applying the convolution theorem, the surface mass density can be determined from measuring the shear alone.

2.2.4 Weak Gravitational Lensing

Weak gravitational lensing makes use of the fact that the surface mass density κ of a lens can be reconstructed from measuring its shear γ.

The shape of the FBG is changed as their light passes by a gravitational lens. If the population of FBG were intrinsically circular, measuring the ellipticity of their images would immediately provide information on the shear of a gravitational lens at the position of each galaxy. As galaxies are intrinsically elliptical, measuring the shape of individual galaxies does not provide significant information about the tidal gravitational field. If we, however, assume that the ellipticity distribution of FBG galaxies is intrinsically random, the shear can be estimated from the net ellipticity of a local galaxy sample.

Many FBG are of rather irregular shape and cannot be well approximated by elliptical isophotes. Moreover, on CCD images we do not measure a continuous brightness distribution, but brightness on CCD pixels. We thus have to develop a measure of ellipticity that is well adapted to observational data of not only elliptical galaxies, but also of more irregular objects.

First we define the center $\bar{\vec{\theta}}$ of an object with brightness distribution $I(\vec{\theta})$,

$$\bar{\vec{\theta}} = \frac{\int \mathrm{d}^2\theta\ q_I[I(\vec{\theta})]\vec{\theta}}{\int \mathrm{d}^2\theta q_I[I(\vec{\theta})]}\ , \tag{2.37}$$

with $q_I(I)$ being a weight function. E.g. if $q_I = \mathrm{H}(I-I_{\mathrm{lim}})$ is the Heaviside step function, $\bar{\vec{\theta}}$ is the center of the area enclosed by the limiting isophote I_{lim}. If q_I is fixed we define the tensor of second brightness moments,

$$Q_{ij} = \frac{\int \mathrm{d}^2\theta\ q_I[I(\vec{\theta})](\theta_i-\bar{\theta}_i)(\theta_j-\bar{\theta}_j)}{\int \mathrm{d}^2\theta\ q_I[I(\vec{\theta})]}\ ,\ i,j\in\{1,2\}\ , \tag{2.38}$$

(Blandford et al. 1991). The shape of an image can now be quantified in terms of the components of the tensor Q_{ij}. We define the complex ellipticity[1],

$$\varepsilon = \frac{Q_{11} - Q_{22} + 2\mathrm{i}Q_{12}}{Q_{11} + Q_{22} + 2(Q_{11}Q_{22} - Q_{12}^2)^{1/2}} \ , \tag{2.39}$$

(Bonnet & Mellier 1995). For elliptical isophotes with axis ratio $r \leq 1$, $\varepsilon = (1-r)(1+r)^{-1}\exp(2\mathrm{i}\vartheta)$, where ϑ is the angle of the major axis with respect to the 1–axis. The factor 2 on the exponential function ensures that the ellipticity is invariant under a rotation by π, reflecting the symmetry of an ellipse.

The relation between source ellipticity $\varepsilon^{(s)}$ and image ellipticity ε is given by

$$\varepsilon^{(\mathrm{s})} = \begin{cases} \frac{\varepsilon - g}{1 - g^*\varepsilon} & |g| \leq 1 \ , \\ \frac{1 - g\varepsilon^*}{\varepsilon^* - g^*} & |g| > 1 \ . \end{cases} \tag{2.40}$$

where the asterisk denotes complex conjugation and we have defined the reduced shear

$$g(\vec{\theta}) = \frac{\gamma(\vec{\theta})}{1 - \kappa(\vec{\theta})} \ , \tag{2.41}$$

(Seitz & Schneider 1997). As the expectation value of $\varepsilon^{(s)}$ is zero, the expectation value of of the observed ellipticity is

$$\left\langle \varepsilon(\vec{\theta}) \right\rangle = g(\vec{\theta}) \ , \tag{2.42}$$

for $|g| < 1$. In the case of weak lensing, $\kappa \ll 1$, $|\gamma| \ll 1$, and thus $|g| \ll 1$, (2.40) becomes $\varepsilon \approx \varepsilon^{(s)} + g$, under the condition that $|\varepsilon| \approx |\varepsilon^{(s)}| \lesssim 1/2$.

The reduced shear g does not change under the following transformation:

$$1 - \kappa'(\vec{\theta}) = \lambda \left[1 - \kappa(\vec{\theta}) \right] \ , \qquad \gamma'(\vec{\theta}) = \lambda\gamma(\vec{\theta}) \ , \tag{2.43}$$

or

$$\kappa'(\vec{\theta}) = \lambda\kappa(\vec{\theta}) + (1 - \lambda) \ . \tag{2.44}$$

This means that replacing κ by a rescaled κ minus a mass sheet of constant surface mass density does not change the observed ellipticities. The invariance transformation (2.43) is the so–called "mass–sheet degeneracy" and implies that from observing image shapes alone, $(1-\kappa)$ can be determined only up to a multiplicative constant. Recalling eq. (2.30), we see that the magnification transforms as

$$\mu'(\vec{\theta}) = \frac{\mu(\vec{\theta})}{\lambda^2} \ . \tag{2.45}$$

Thus, taking magnification effects in to account, the mass–sheet degeneracy can be lifted.

[1] This is not the only measure of the shape of an image that is dubbed *complex ellipticity*. In the literature one finds for example $\chi = \frac{Q_{11} - Q_{22} + 2\mathrm{i}Q_{12}}{Q_{11} + Q_{22}}$ under the same name.

2.3 Mass Reconstruction

As stated in the previous section, the surface mass density of a lens can be reconstructed (up to an additive constant) from the observed shapes of the background galaxies. One way to achieve a measurement of κ, the inversion method of Kaiser & Squires (1993, KS93), was already mentioned in section 2.2.3. By Fourier–transforming eq. (2.36) and applying the convolution theorem, the surface mass density can be computed from the integral

$$\kappa(\vec{\theta}) - \kappa_0 = \frac{1}{\pi} \int_{\mathbb{R}^2} \mathrm{d}^2\theta' \, \mathcal{R} \left[\mathcal{D}^*(\vec{\theta} - \vec{\theta}')\gamma(\vec{\theta}') \right] \, , \tag{2.46}$$

where the constant κ_0 is due to the mass–sheet degeneracy. For applying (2.46) to observational data, the integral is replaced by a sum,

$$\kappa(\vec{\theta}) = \frac{1}{\overline{n}\pi} \sum_i \mathcal{R} \left[\mathcal{D}^*(\vec{\theta} - \vec{\theta}_i)\varepsilon_i \right] \, , \tag{2.47}$$

where the summation is carried out over galaxies at position θ_i, and $\overline{n}$ is the number density of galaxies. Unfortunately, as already noticed by KS93, this estimator has an infinite variance, because of the sampling noise introduced by the random position of galaxies. This problem can be overcome by spatially smoothing the shear data. While the form of eq. (2.47) stays the same if the shear estimate is smoothed, the expression for the kernel $\mathcal{D}$ changes. For the case of Gaussian smoothing with smoothing length θ_s the new kernel reads

$$\tilde{\mathcal{D}}(\vec{\theta}) = \left[1 - \left(1 + \frac{|\vec{\theta}|^2}{\theta_\mathrm{s}^2} \right) \exp\left(-\frac{|\vec{\theta}|^2}{\theta_\mathrm{s}^2} \right) \right] \, , \tag{2.48}$$

(Seitz & Schneider 1995). While the smoothing allows estimates for κ with finite noise it also introduces a strong spatial correlation of errors. van Waerbeke (2000) showed under the assumption of no lensing, i.e. $\gamma = 0$, that the covariance of a κ–map obtained with the kernel (2.48) is

$$\mathrm{Cov}(\kappa(\vec{\theta}), \kappa(\vec{\theta}')) = \frac{\sigma_\varepsilon^2}{4\pi\theta_\mathrm{s}^2\overline{n}} \exp\left(-\frac{|\vec{\theta} - \vec{\theta}'|^2}{2\theta_\mathrm{s}^2} \right) \, , \tag{2.49}$$

meaning that the correlation extends to scales of the order of the smoothing scale. It should be noted that in the presence of shear, the random galaxy distribution contributes shot–noise. This effect is studied in detail in Lombardi et al. (2002). It turns out that smoothing the shear data and applying eq. (2.46) results in less noisy mass maps than using (2.47) with the kernel $\tilde{\mathcal{D}}$ (Seitz & Schneider 1995), because eq. (2.47) contains the shot–noise contribution.

2.3.1 Finite Field Inversion as a von Neumann Boundary Problem

The obvious disadvantage of the KS93 method is that the integration (2.46) has to be carried out over $\mathbb{R}^2$ while the observed field will always have a finite size. KS93 avoid this problem by setting $\gamma = 0$ outside the observed field. While this allows to do the integration, it invents data, that is not actually there. The result is that KS93 reconstructions are dominated by systematic errors in the corner of observed fields, where the influence of regions on which γ is set to zero is largest.

To avoid this problem inversion methods on finite fields have been developed. I will in the following discuss the method of Seitz & Schneider (2001, hereafter SAS) in more detail.

We first define the quantity

$$K(\vec{\theta}) = \ln\left[1 - \kappa(\vec{\theta})\right] \ . \tag{2.50}$$

Due to the mass–sheet degeneracy, K can only be determined up to an additive constant. Kaiser (1995) showed that the following relation for the gradient of K holds:

$$\vec{u}(\vec{\theta}) = \nabla K = \frac{-1}{1-|g|^2} \begin{pmatrix} 1-g_1 & -g_2 \\ -g_2 & 1+g_1 \end{pmatrix} \begin{pmatrix} g_{1,1}+g_{2,2} \\ g_{2,1}-g_{1,2} \end{pmatrix} \ . \tag{2.51}$$

Eq. (2.51) can be solved (up to an additive constant caused by the mass–sheet degeneracy) by line integration, and several methods have been developed (Schneider 1995; Kaiser et al. 1995; Bartelmann 1995; Squires & Kaiser 1996) to do this.

Observational noise is present in the vector field $\vec{u}(\vec{\theta})$ for all real data. Thus, in general, $\vec{u}(\vec{\theta})$ will not be a gradient field but will have an additional rotational part ,

$$\vec{u}(\vec{\theta}) = \nabla\tilde{K} + \nabla \times s(\vec{\theta}) = \nabla\tilde{K} + \begin{pmatrix} \partial s/\partial\theta_2 \\ -\partial s/\partial\theta_1 \end{pmatrix} \ , \tag{2.52}$$

where $s(\vec{\theta})$ is a scalar field (Seitz & Schneider 1996). Although this decomposition is not unique, it can be uniquely fixed by setting $s = \text{const}$ on the boundary $\partial\mathcal{U}$ of the observed field $\mathcal{U}$. This implies that the mean of $\nabla \times s(\vec{\theta}) = 0$ on $\mathcal{U}$, as is expected for a noise contribution, and that $\nabla \times s(\vec{\theta}) = 0$ if $\vec{u}(\vec{\theta})$ is a gradient field. Then, if we identify $\nabla\tilde{K}$ with ∇K, eq. (2.51) can be solved to (Seitz & Schneider 1996)

$$K(\vec{\theta}) - \bar{K} = \int_{\mathcal{U}} \mathrm{d}^2\theta' \ \vec{H}(\vec{\theta}', \vec{\theta}) \cdot \vec{u}(\vec{\theta}) \ , \tag{2.53}$$

where $\vec{H}(\vec{\theta}', \vec{\theta})$ is a vector field obtained from the Greens function of a Laplace equation with Neumann boundary conditions, and $\bar{K}$ is the average of K over the data field $\mathcal{U}$.

Taking the divergence of eq. (2.52) we arrive at

$$\nabla^2 K(\vec{\theta}) = \nabla \cdot \vec{u}(\vec{\theta}) \ , \tag{2.54}$$

and since we required $s = \text{const}$ on $\partial\mathcal{U}$, $\nabla \times s(\vec{\theta})$ is perpendicular to the normal vector $\vec{n}$ on $\partial\mathcal{U}$. Thus, on $\partial\mathcal{U}$

$$\vec{n} \cdot \nabla K = \vec{n} \cdot \vec{u} \tag{2.55}$$

holds. K can now be computed by solving the Neumann problem given by eqs. (2.54) and (2.55). SAS provide a FORTRAN–77 implementation of this method that uses the successive overrelaxation algorithm of Press et al. (1992b, p. 857).

The practical implementation of the method described above employs the following steps:

1. The galaxy ellipticities are spatially smoothed. The reduced shear at the position $\vec{\theta}$ is calculated from

$$g(\vec{\theta}) = \frac{\sum_{i=1}^{N_g} w(|\vec{\theta} - \vec{\theta}_i|)\varepsilon_i}{\sum_{i=1}^{N_g} w(|\vec{\theta} - \vec{\theta}_i|)} \ , \tag{2.56}$$

   where ε_i is the ellipticity of the ith galaxy at position $\vec{\theta}_i$. N_g is the number of all galaxies and $w(\theta)$ is a suitably chosen weight function. SAS set

$$w(\theta) = \begin{cases} \exp\left(-\frac{\theta^2}{(\Delta\theta)^2}\right) - \exp(-q) & \theta \leq \sqrt{q}\Delta\theta \ , \\ 0 & \text{otherwise.} \end{cases} \tag{2.57}$$

   with $\Delta\theta$ being the smoothing scale and q a constant fixed at $q = 9$, so that the smoothing is nearly Gaussian and w is continuous at $\theta = \sqrt{q}\Delta\theta$. From eq. (2.56) the reduced shear can then be calculated on a regular grid.

2. Employing eq. (2.51) the vector field $\vec{u}(\vec{\theta})$ is obtained from the smoothed $g(\vec{\theta})$ by finite differencing.

3. The Neumann problem (eqs. (2.54), (2.55)) is solved using successive overrelaxation.

2.4 The Aperture Mass Statistic

A statistic that is not affected by the mass–sheet degeneracy is the aperture mass M_{ap}, which is a generalization of Kaiser's (Kaiser 1995) ζ–statistic,

$$\zeta(\vec{\theta}_0; \vartheta_1, \vartheta_2) = \bar{\kappa}(\vec{\theta}_0; \vartheta_1) - \bar{\kappa}(\vec{\theta}_0; \vartheta_1, \vartheta_2) \ , \tag{2.58}$$

which is the difference of the mean surface mass density in circle of radius ϑ_1 around $\vec{\theta}$ and in an annulus of inner and outer radii ϑ_1 and ϑ_2, respectively. Because the invariance transformation (2.44) corresponds to an unknown additive constant in κ, it drops out of equation (2.58).

The aperture mass at a point $\vec{\theta}_0$ is defined to be

$$M_{\rm ap}(\vec{\theta}_0) = \int {\rm d}^2\theta\, \kappa(\vec{\theta}) U(\vec{\theta} - \vec{\theta}_0) \ , \tag{2.59}$$

where $U(\vec{\theta})$ is a weight function. For instance if

$$U(\vartheta) = U(|\vec{\theta} - \vec{\theta}_0|) = \begin{cases} \frac{1}{\pi\vartheta_1^2} & 0 \le \vartheta \le \vartheta_1 \ , \\ -\frac{1}{\pi(\vartheta_2^2 - \vartheta_1^2)} & \vartheta_1 < \vartheta \le \vartheta_2 \ , \\ 0 & \text{otherwise.} \end{cases} \tag{2.60}$$

the ζ–statistic (2.58) is recovered.

Now let the weight function be constant on closed curves $\vec{c}(\lambda)$, $\lambda \in I$, where I is a finite interval. Without loss of generality we require $\vec{c} \times \dot{\vec{c}} = c_1\dot{c}_2 - c_2\dot{c}_1 > 0$. We then define a new coordinate system (b, λ) around the point $\vec{\theta}_0$ by $\vec{\theta} = \vec{\theta}_0 + b\vec{c}(\lambda)$. U now only depends on b, and (2.59) is transformed to

$$M_{\rm ap}(\vec{\theta}_0) = \int_0^\infty {\rm d}b\, b\, U(b) \oint_I {\rm d}\lambda\, (\vec{c} \times \dot{\vec{c}})\, \kappa[\vec{\theta}_0 + b\vec{c}(\lambda)] \ , \tag{2.61}$$

where we used the Jacobian $b\vec{c} \times \dot{\vec{c}}$ of the coordinate transformation. Integrating (2.61) by parts with respect to b gives

$$M_{\rm ap}(\vec{\theta}) = -\int_0^\infty {\rm d}b\, b\, u(b) \oint_I {\rm d}\lambda\, (\vec{c} \times \dot{\vec{c}}) \frac{\partial\kappa}{\partial b}[\vec{\theta}_0 + b\vec{c}(\lambda)] \ , \tag{2.62}$$

where we set

$$u(b) = \frac{1}{b}\int_0^b {\rm d}b'\, b'\, U(b') \ , \tag{2.63}$$

and required that the weight function is compensated:

$$\int_0^\infty {\rm d}b\, b\, U(b) = 0 \ , \tag{2.64}$$

so that the boundary terms vanish.

We note that by partially differentiating eq. (2.26) and combining suitable terms we find

$$\nabla\kappa = \begin{pmatrix} \gamma_{1,1} + \gamma_{2,2} \\ \gamma_{2,1} - \gamma_{1,2} \end{pmatrix} \ . \tag{2.65}$$

Using this relation we transform the partial derivative $\partial\kappa/\partial b$ to

$$\begin{aligned} \frac{\partial\kappa}{\partial b} &= c_1\frac{\partial\kappa}{\partial\theta_1} + c_2\frac{\partial\kappa}{\partial\theta_2} = c_1\left(\frac{\partial\gamma_1}{\partial\theta_1} + \frac{\partial\gamma_2}{\partial\theta_2}\right) + c_2\left(\frac{\partial\gamma_2}{\partial\theta_1} - \frac{\partial\gamma_1}{\partial\theta_2}\right) \\ &= \frac{1}{\vec{c} \times \dot{\vec{c}}}\left[(c_1\dot{c}_2 + \dot{c}_1c_2)\frac{\partial\gamma_1}{\partial b} + (c_2\dot{c}_2 - c_1\dot{c}_1)\frac{\partial\gamma_2}{\partial b}\right] \\ &\quad + \frac{1}{b\vec{c} \times \dot{\vec{c}}}\left[-2c_1c_2\frac{\partial\gamma_1}{\partial\lambda} + (c_1^2 - c_2^2)\frac{\partial\gamma_2}{\partial\lambda}\right] \ . \end{aligned} \tag{2.66}$$

We insert (2.66) into eq. (2.62) and integrate the terms containing partial derivatives to b and λ by part to b and λ, respectively. We then have an expression for $M_{\rm ap}$ that depends only on the observable γ:

$$M_{\rm ap}(\vec{\theta}) = \int_0^\infty {\rm d}b\ [2u(b) - bU(b)] \oint_I {\rm d}\lambda\ [-(c_1\dot{c}_2 + \dot{c}_1 c_2)\gamma_1 + (c_1\dot{c}_1 - c_2\dot{c}_2)\gamma_2]\ . \qquad (2.67)$$

We can write this in more compact form by defining

$$Q(b) = \frac{1}{b^2}\,[2bu(b) - U(b)] = \frac{2}{b^2}\int_0^b {\rm d}b'\ b'U(b) - U(b)\ , \qquad (2.68)$$

and writing $\vec{c}(\lambda)$ in complex notation $C(\lambda) = c_1(\lambda) + {\rm i}c_2(\lambda)$. The final result then is

$$M_{\rm ap}(\vec{\theta}) = \int {\rm d}^2\theta\ Q[b(\vec{\theta})]\frac{\mathcal{I}[\gamma(\vec{\theta})C^*\dot{C}^*]}{\mathcal{I}[C^*\dot{C}^*]}\ . \qquad (2.69)$$

In most cases circular apertures will be of interest. Then $(b,\lambda) = (\vartheta,\varphi)$, $C(\varphi) = \exp({\rm i}\varphi)$, $\mathcal{I}(C^*\dot{C}^*) = 1$, and

$$\begin{aligned}\mathcal{I}(\gamma C^*\dot{C}^*) &= \gamma_{\rm t}(\vec{\theta};\vec{\theta}_0) = -[\gamma_1\cos(2\varphi) + \gamma_2\sin(2\varphi)] \\ &= -\mathcal{R}[\gamma(\vec{\theta}+\vec{\theta}_0){\rm e}^{-2{\rm i}\varphi}]\ , \end{aligned} \qquad (2.70)$$

where we have defined the tangential shear $\gamma_{\rm t}$ relative to a point $\vec{\theta}_0$. Eq. (2.69) then becomes

$$M_{\rm ap} = \int {\rm d}^2\theta\ Q(\vartheta)\gamma_{\rm t}(\vec{\theta};\vec{\theta}_0)\ . \qquad (2.71)$$

For use on real data the integral in (2.71) is replaced by a sum over background galaxies

$$M_{\rm ap}(\vec{\theta}_0) = \frac{1}{\overline{n}}\sum_{i=1}^N Q(\vartheta_i)\varepsilon_{{\rm t}i}\ , \qquad (2.72)$$

where $\overline{n}$ is the number density of FBG in the aperture and we define $\varepsilon_{{\rm t}i}$ in analogy to $\gamma_{\rm t}$, as the tangential ellipticity of the ith background galaxy with respect to the point $\vec{\theta}_0$,

$$\varepsilon_{{\rm t}i} = -\mathcal{R}(\varepsilon_i{\rm e}^{-2{\rm i}\varphi})\ . \qquad (2.73)$$

The significance of the $M_{\rm ap}$ statistic can either be assessed analytically or numerically. We calculate the rms dispersion $\sigma(M_{\rm ap}) = \left(\left\langle M_{\rm ap}^2\right\rangle - \left\langle M_{\rm ap}\right\rangle^2\right)^{1/2}$ for the case of no lensing, i. e. the expectation value $\langle M_{\rm ap}\rangle$ of the aperture mass vanishes. This is a valid approximation for weak gravitational lensing. The analytic expression of the rms dispersion for background galaxies with intrinsic two–dimensional ellipticity dispersion σ_ε is given by

$$\sigma(M_{\rm ap}) = \frac{\sigma_\varepsilon}{\sqrt{2\overline{n}}}\left[\sum_{i=1}^N Q^2(\vartheta_i)\right]^{1/2}\ , \qquad (2.74)$$

where we used the fact that

$$\langle \varepsilon_{\mathrm{t}i} \varepsilon_{\mathrm{t}j} \rangle = \frac{\sigma_\varepsilon^2}{2} \delta_{ij} \ . \tag{2.75}$$

Numerically the signal–to–noise ratio is determined by randomizing the orientation of background galaxies within the aperture while keeping their position and absolute value of the ellipticity fixed. The dispersion is obtained from many realizations of the randomization. If σ_i denotes the randomized aperture mass value for the ith randomization, the signal–to–noise ratio is given by

$$\frac{S}{N} = \frac{M_{\mathrm{ap}}}{\sqrt{\frac{1}{n}\sum_{i=0}^{n} \sigma_i^2}} \ . \tag{2.76}$$

The weight function is arbitrary at this point. However, it can be shown that the signal–to–noise ratio is maximized if the weight function $U(\vec{\theta})$ follows the surface mass density. A common choice for circular apertures is

$$U(\vartheta) = \frac{(l+2)^2}{\pi \vartheta_{\mathrm{max}}^2} \left[1 - \left(\frac{\vartheta}{\vartheta_{\mathrm{max}}} \right)^2 \right]^l \left[\frac{1}{l+2} - \left(\frac{\vartheta}{\vartheta_{\mathrm{max}}} \right)^2 \right] \ , \tag{2.77}$$

(Schneider et al. 1998), for $\vartheta \leq \vartheta_{\mathrm{max}}$ and zero elsewhere.

2.5 Aperture Multipole Moments

The idea of integrating over the shear in a circle to compute the weighted mass within an aperture can be modified to yield multipole moments of the mass distribution within an aperture (Schneider & Bartelmann 1997). Contrary to the aperture mass statistics the aperture multipole statistics does not require that the weight function is compensated.

We define the complex nth multipole in a circular aperture by

$$Q^{(n)} = \int_0^\infty \mathrm{d}\theta \ \theta^{n+1} U(\theta) \int_0^{2\pi} \mathrm{d}\varphi \ \mathrm{e}^{n\mathrm{i}\varphi} \kappa(\vec{\theta}_0 + \vec{\theta}) \ , \tag{2.78}$$

where $U(|\vec{\theta}|)$ is a radially symmetric weight function.[2] Integrating (2.78) by parts with respect to φ yields

$$Q^{(n)} = \frac{\mathrm{i}}{n} \int_0^\infty \mathrm{d}\theta \ \theta^{n+1} U(\theta) \int_0^{2\pi} \mathrm{d}\varphi \ \mathrm{e}^{n\mathrm{i}\varphi} \frac{\partial \kappa}{\partial \varphi} \ . \tag{2.79}$$

[2]Contrary to the statement made in a footnote in Bartelmann & Schneider (2001), the aperture multipole moment statistics is limited to radially symmetric filters. This can be easily understood, if one e.g. tries to calculate the quadrupole moment in an elliptic aperture on a field with constant surface mass density κ_0. The quadrupole moment will then depend on κ_0 which, due to the mass–sheet degeneracy, is only fixed up to a constant.

Transforming (2.65) into polar coordinates we get

$$\frac{\partial\kappa}{\partial\varphi} = -\theta\frac{\partial\gamma_1}{\partial\theta}\sin(2\varphi) - \frac{\partial\gamma_1}{\partial\varphi}\cos(2\varphi) + \theta\frac{\partial\gamma_2}{\partial\theta}\cos(2\varphi) - \frac{\partial\gamma_2}{\partial\varphi}\sin(2\varphi) \ , \tag{2.80}$$

which we insert into (2.79). Partially integrating terms that contain derivatives with respect to θ and φ with respect to θ and φ, respectively, leads to

$$\begin{aligned} Q^{(n)} &= \int_0^\infty \mathrm{d}\theta\ \theta^{n+1}U(\theta)\int_0^{2\pi}\mathrm{d}\varphi\ \mathrm{e}^{n\mathrm{i}\varphi}\gamma_\mathrm{t}(\vec{\theta};\vec{\theta}_0) \\ &\quad + \frac{\mathrm{i}}{n}\int_0^\infty \mathrm{d}\theta\ \left[n\theta^{n+1}U(\theta) + \theta^{n+2}U'(\theta)\right]\int_0^{2\pi}\mathrm{d}\varphi\ \mathrm{e}^{n\mathrm{i}\varphi}\gamma_\mathrm{r}(\vec{\theta};\vec{\theta}_0) \ . \end{aligned} \tag{2.81}$$

Here $U'(\theta)$ is the derivative of $U(\theta)$, $U(\theta)$ has to be continuous and piecewise differentiable and we define the radial shear at position $\vec{\theta}$ relative to position $\vec{\theta}_0$ in analogy to eq. (2.70) by

$$\gamma_\mathrm{r}(\vec{\theta};\vec{\theta}_0) = -\left[\gamma_2\cos(2\varphi) - \gamma_1\sin(2\varphi)\right] = -\mathcal{I}\left[\gamma(\vec{\theta}+\vec{\theta}_0)\mathrm{e}^{-2\mathrm{i}\varphi}\right] \ . \tag{2.82}$$

For the boundary terms to vanish in the integration leading to (2.81), the weight function has to fulfill the conditions

$$|\gamma|\theta^{n+2}U(\theta) \to 0 \text{ for } \theta \to 0 \text{ and } \theta \to \infty \ . \tag{2.83}$$

To simplify notation we define

$$\begin{aligned} g_\mathrm{t}(\theta) &= \int_0^{2\pi}\mathrm{d}\varphi\ \mathrm{e}^{n\mathrm{i}\varphi}\gamma_\mathrm{t}(\vec{\theta};\vec{\theta}_0) \\ g_\mathrm{r}(\theta) &= \int_0^{2\pi}\mathrm{d}\varphi\ \mathrm{e}^{n\mathrm{i}\varphi}\gamma_\mathrm{r}(\vec{\theta};\vec{\theta}_0) \ . \end{aligned} \tag{2.84}$$

We then can get a local estimate of the aperture multipole moment in a circle of radius R from

$$Q^{(n)} = \int_0^R \mathrm{d}\theta\ \theta^{n+1}U(\theta)g_\mathrm{t}(\theta) + \frac{\mathrm{i}}{n}\int_0^R \mathrm{d}\theta\ \theta^{n+1}\left[nU(\theta) + \theta U'(\theta)\right]g_\mathrm{r}(\theta) \ . \tag{2.85}$$

As in the case of the aperture mass statistics the integral is replaced by a sum over galaxy ellipticities to compute the aperture multipole statistics from real data.

$$Q^{(n)}(\vec{\theta}_0) = \frac{1}{\overline{n}}\sum_{i=1}^{N}\mathrm{e}^{n\mathrm{i}\varphi_i}\left\{\theta_i^n U(\theta_i)\varepsilon_{\mathrm{t}i} + \mathrm{i}\frac{\theta_i^n[nU(\theta_i) + \theta U'(\theta_i)]}{n}\varepsilon_{\mathrm{r}i}\right\} \ , \tag{2.86}$$

where $\overline{n}$ is the number density of galaxies in the circle, (θ_i, φ_i) are the polar coordinates of the ith galaxy with respect to $\vec{\theta}_0$, and $\varepsilon_{\mathrm{r}i} = -\mathcal{I}(\varepsilon_i\mathrm{e}^{-2\mathrm{i}\varphi_i})$ is the radial component of the ellipticity of the ith galaxy with respect to the origin of the coordinate system.

As is the case for the $M_{\rm ap}$ statistics, the significance of a multipole moment measurement can in the no–lensing limit either be computed from an analytic expression,

$$\sigma^{(n)} = \frac{\sigma_\varepsilon}{\sqrt{2\overline{n}}} \left\{ \sum_{i=1}^{N} \left[\left(\theta_i^n U(\theta_i) \right)^2 + \left(\frac{\theta_i^n (nU(\theta_i) + \theta U'(\theta_i))}{n} \right)^2 \right] \right\}^{1/2} , \tag{2.87}$$

where in addition to (2.75) we used

$$\langle \varepsilon_{{\rm r}i} \varepsilon_{{\rm r}j} \rangle = \frac{\sigma_\varepsilon^2}{2} \delta_{ij} \quad \text{and} \quad \langle \varepsilon_{{\rm t}i} \varepsilon_{{\rm r}j} \rangle = 0 \ , \tag{2.88}$$

or from randomizing the orientation of the FBG.

Chapter 3

Quantifying Filaments

In order to quantify the presence of a filament and the significance of its detection three problems must be solved. First, due to the correlation of error bars described in section 2.3 the significance of a filament in a reconstructed mass map cannot be assessed directly from the reconstruction. Statistics like the aperture mass (section 2.4) and aperture multipole moments (section 2.5) allow the calculation of signal–to–noise ratios for a limited spatial region and are thus well suited to quantify the presence of a structure in that region. Aperture statistics, however, integrate over the weighted surface mass density in an aperture. Hence, to quantify the presence of a structure between two galaxy clusters, the aperture has to be chosen such that it avoids the clusters and is limited to the filament candidate. This is the second problem. The third and most fundamental question that has to be answered is, "What is a filament?". How for instance can we distinguish the overlapping halos of two close galaxy clusters from a filament? While in some cases the question whether a structure between two cluster indeed constitutes a filament is easy to answer intuitively, it can be difficult to quantify in many other cases.

3.1 N–Body Simulations

I used results of n–body simulations of close pairs of galaxy clusters in an attempt to solve these problems. These results were provided to me by Emilio Romano–Díaz. The simulations use 64^3 particles in box with 50 h^{-1} Mpc side length in a standard CDM, $\Omega_\Lambda = 0$, $\Omega_\mathrm{m} = 1$, $h = 0.5$ cosmology. The mass of an individual particle is $3.308 \times 10^{10} M_\odot$. The simulations were carried out using a particle–particle–particle–mesh ($\mathrm{P^3M}$) code. $\mathrm{P^3M}$ codes use a particle–mesh (PM) code for calculating long–range interactions, while the interaction of particles at smaller separations is directly computed as particle–particle (PP) interaction. Direct evaluation of the forces between all particles would scale with the square of the number of particles. For large n–body simulations the computational resources needed would become prohibitively large. PM codes interpolate the density distribution onto a grid and solve the Poisson equation for the gravitational potential using a Fast–Fourier–Transformation (FFT). The force acting on each particle is then computed

by evaluation of the gravitational field at the respective particle position. While the latter operation scales linearly with the number of particles, the FFT scales with $N_g \log N_g$, N_g being the number of grid points. For sufficiently large grids the speed of PM codes is thus determined by the number of grid points. Particle–particle interaction, however, is directly calculated when particles come close to each other, as the spatial resolution of the PM method is limited by the size of the grid cells.

The discrete particle distribution in the simulation represents a smooth mass distribution, which we need for lensing simulations. The simulated particle distribution thus has to be smoothed to gain an estimate of the underlying smooth distribution. Instead of choosing a Gaussian smoothing with a fixed smoothing length I decided to adopt the adaptive kernel density estimate described by Pisani (1996, 1993).

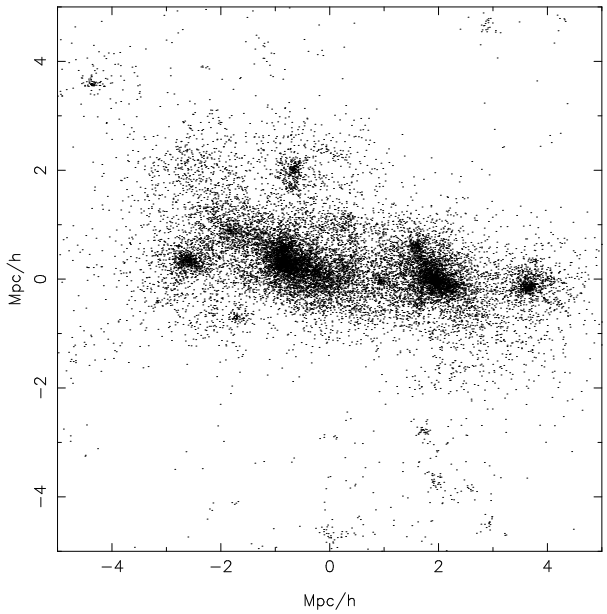

Figure 3.1: Zoom in on the central 10×10 Mpc$^2/h^2$ of an n–body simulation. Displayed is the projection of a slice of 2.5 Mpc/h thickness.

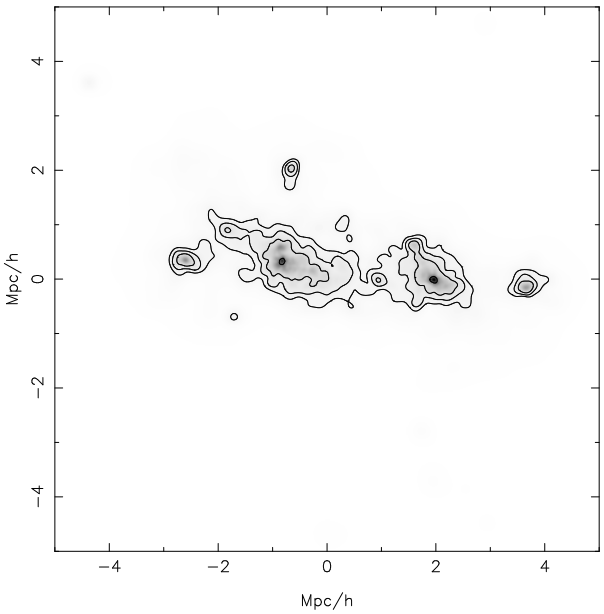

Figure 3.2: Smooth density distribution of the data in the left panel from the adaptive kernel density estimate. The contours are at $\kappa = \{0.03, 0.05, 0.1, 0.5\}$.

To get density estimates in a reasonable time I applied the adaptive kernel method usually not to the full simulation output, but only to an interesting subsample of the simulation showing the galaxy clusters and the filament connecting them. Figures 3.1 and 3.2 show such a subsample and the corresponding smooth density distribution. The subsample is a $10 \times 10 \times 2.5$ Mpc$^3/h^3$ slice of the n–body simulation at a redshift $z = 0.21$. The surface mass density in the right panel was not calculated from the mass of the particles but linearly scaled, such that the surface mass density in the cluster center is just undercritical.

3.2 Lensing Simulations using N–Body Data

The next step in employing the results of the n–body simulations in a gravitational lens study has to be the derivation of the lensing properties of the simulated mass distribution. While it is in principle possible to gain the deflection potential and from that the shear by finite integration and differentiation via eqs. (2.24) and (2.26), this is a cumbersome and time consuming method. It is much faster and simpler to calculate the shear directly from the simulated surface mass density using eq. (2.36) and the convolution theorem. The Fourier transformation of the complex kernel $\mathcal{D}$ (eq. (2.36)) reads,

$$\hat{\mathcal{D}}(\vec{k}) = \pi \frac{k_1^2 - k_2^2 + 2\mathrm{i}k_1k_2}{|\vec{k}|^2} \ , \tag{3.1}$$

and thus the Fourier transformed shear is given by

$$\hat{\gamma}(\vec{k}) = \frac{1}{\pi}\hat{\mathcal{D}}(\vec{k})\hat{\kappa}(\vec{k}) \ , \qquad \text{for } \vec{k} \neq 0 \ . \tag{3.2}$$

The shear is then calculated via the inverse Fourier transformation and the magnification is easily computed from the right hand side of eq. (2.45).

The Fourier transformation is calculated with the Fast Fourier Transformation (FFT) algorithm. A description of FFT can be found for example in Press et al. (1992b). An implementation that readily computes lensing quantities like the shear and magnification on a grid from discrete κ–maps as outlined above is the `kappa2stuff` program from Nick Kaiser's `IMCAT` package (`http://www.ifa.hawaii.edu/~kaiser/imcat/`). To account for the finite field size, FFT uses periodic boundary conditions. The surface mass density at the edges of the simulated fields is small enough to not lead to any artifacts due to the boundary conditions.

For the lensing simulation, catalogs of background galaxies were produced. Galaxies were randomly placed within a predefined area until the specified number density was reached. To each galaxy an intrinsic ellipticity was assigned from two Gaussian random deviates. Until noted otherwise all simulations have 30 galaxies/arcmin^2 and a one dimensional ellipticity dispersion of $\sigma_\varepsilon = 0.2$.

Since the shear and magnification is only known on a grid, they were linearly interpolated between the four grid points neighboring each galaxy to compute these quantities at the galaxy position. To simplify the program, galaxies at the edges that have less than four neighboring grid points were removed from the catalog. The "observed" ellipticity of each galaxy was calculated according to eq. (2.40) while the number density of galaxies was adjusted following eq. (2.35) with $\alpha = 0.5$. For each galaxy a uniformly distributed random deviate from the interval $[0; 1)$ was drawn. If the random deviate was bigger than $\mu^{-0.5}$ the galaxy was deleted from the catalog.

Figure 3.3 shows a mass reconstruction of the simulated density map in Fig. 3.2 with the method of SAS described in section 2.3. The lensing properties of the simulation were calculated as described above on a 2048×2048 points grid and the computed shear and

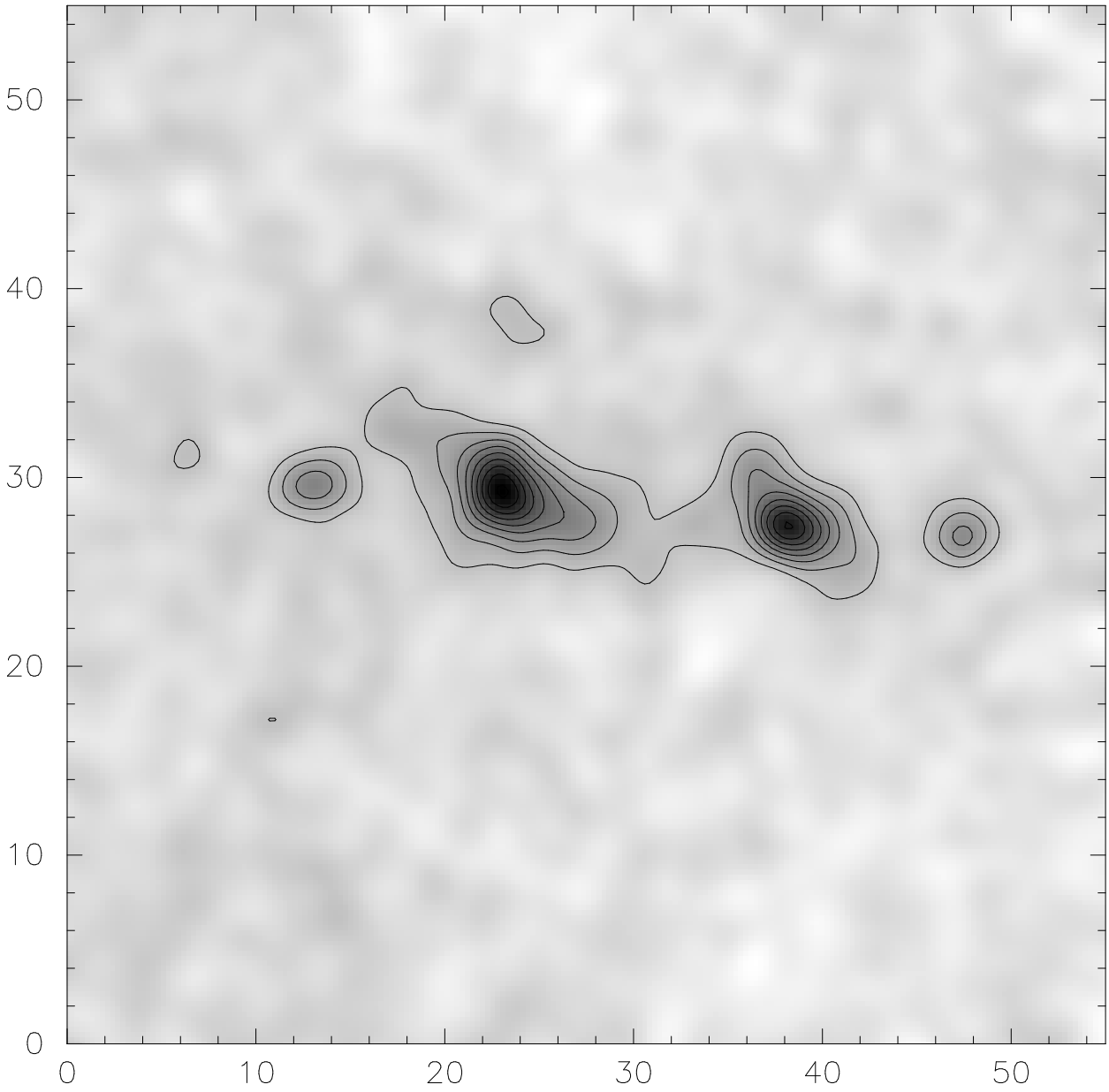

Figure 3.3: Reconstruction of the mass distribution in Fig. 3.2 on a 206×206 points grid. The scale of the axes is given in arcminutes. The contours mark an increase of κ in steps of 0.025 above the mean of the edge of the field.

magnification were applied to a random catalog of background galaxies. The reconstruction was performed on a 206×206 points grid with a $1\farcm3$ smoothing scale.

The quality of the reconstruction is much higher than one would expect for real observational data for a number of reasons.

1. All galaxies in the catalog are indeed background objects. In real data, the catalog of background galaxies would inevitably be contaminated by stars and faint foreground galaxies (mainly dwarf galaxies in the cluster one observes).

2. No effects like atmospheric smearing and distortions of the image by the telescope and/or camera optics deteriorate the determination of the observed galaxy ellipticity.

3. The intrinsic ellipticity dispersion of the background galaxies is too low compared with real data, which suggests $\sigma_\varepsilon = 0.3$ or even higher.

4. Likewise, the assumed number density of background objects is at the high end of what one typically can achieve with ground–based observations.

The few differences between the original mass distribution and the reconstruction thus indicate systematic deviations due to the smoothing and not due to noise caused by the intrinsic ellipticities of galaxies and their random distribution. Of course, some degree of noise is still present in the reconstructed mass distribution but it is not the dominant feature of the reconstruction.

It is immediately obvious that many small scale features present in the simulation are not recovered in the reconstruction. This is due to the smoothing done to the shear data. One can show that in the absence of Poisson noise and under the assumption $g = \gamma$ the smoothing of the shear data is equivalent to a convolution of the mass distribution with the smoothing kernel (van Waerbeke 2000). This also explains that the density peaks in the reconstruction are broader and not as high as in the original mass map.

3.3 Fitting Elliptical Profiles to Galaxy Clusters

With all the tools needed to simulate the weak gravitational lens effect at hand, we can now concentrate on the quantification of a filament. In a first attempt we try to represent the galaxy clusters by elliptical mass profiles. We then define the filament as the part of the mass distribution which is in excess of the mass fitted by the ellipses.

Two different approaches can be used when fitting elliptical profiles to the clusters. First, the fitting can be done to the reconstructed mass distribution. Second, the fitting can be done adjusting the elliptical profiles so that their shear matches the observed shear.

The first method has the advantage that the surface mass density is a much more intuitive quantity than the shear. Problems in the fitting procedure are easier to understand when working with the surface mass density. On the other hand, κ is not an observable. The only observable is the reduced shear and the surface mass density has to be reconstructed from the shear first. As we have seen in the previous section, even in the absence of strong

observational noise, the reconstructed mass profile deviates systematically from the true mass profile.

Fitting directly to the shear avoids the additional intermediate step of mass reconstruction and is thus not susceptible to the broadening of the core radius introduced by the smoothing of the shear data. Directly using the shear as the quantity to which the elliptical profiles of the clusters are fitted also has disadvantages. First, the shear at a given position is determined by the surface mass density on the whole field. This makes it much harder to control the fitting process by chosing suitable weight functions that guide the fitting process in the right direction. Second, the profiles for which the shear can be computed analytically are very limited. While fitting to the surface mass density allows one to have a flexible radial profile, one is limited to radial profiles for which analytic expressions for the shear are known, when fitting directly to the shear.

Common to all fitting procedures is that they try to minimize a quantity

$$\chi^2 = \int \mathrm{d}^2\theta \, \left[f_{\mathrm{true}}(\vec{\theta}) - f_{\mathrm{sim}}(\vec{\theta}) \right]^2 w(\vec{\theta}) \; . \tag{3.3}$$

For example if one fits to the reconstructed surface mass density, $f_{\mathrm{true}}(\vec{\theta})$ is $\kappa(\vec{\theta})$ from the reconstruction, while $f_{\mathrm{sim}}(\vec{\theta})$ is the surface mass density of the fitted ellipses. $w(\vec{\theta})$ is a weight function that can be chosen to guide the minimization procedure in the right direction.

Various methods for multidimensional minimization are available. All programs used for fitting either used the Downhill Simplex or Powell's Direction Set algorithms discussed in detail in Press et al. (1992a). I could not find any systematic differences between the results of the two methods. In general, their results agreed quite well if the same starting values were used.

Common to all algorithms for multidimensional minimization is the problem that they cannot guarantee to find the global minimum but only a local one. One has to choose the starting parameters so that they are already close to the suspected global minimum to help the minimization procedure find the right minimum.

3.3.1 Fitting Elliptical Profiles to the Simulated Surface Mass Density

As a first test to see how well clusters could be represented by elliptical profiles, I fitted two ellipses with a King profile directly to the simulated data. The surface mass density of a circular King profile is given by

$$\Sigma(\theta) = \Sigma_0 \left[1 + \left(\frac{\theta}{\theta_{\mathrm{c}}} \right)^2 \right]^{-1} \; , \tag{3.4}$$

where Σ_0 is the surface mass density in the center, θ_{c} is the core radius of the profile, and θ is the distance from the cluster center. There are 12 parameters that have to be

determined in the minimization procedure, 6 for each cluster. The parameters are position of the cluster center, Σ_0, θ_c, axis ratio of the ellipse, and orientation of the ellipse. As the position of the clusters in the simulation is well known, the central position can be used as a starting value. This is necessary to avoid that the minimization procedure puts both ellipses on one cluster or even on a small mass peak away from the clusters because this might very well be a local minimum in which we are not interested. It is sufficient to set the starting values of the other parameters to values in the right order of magnitude to achieve reasonable fits.

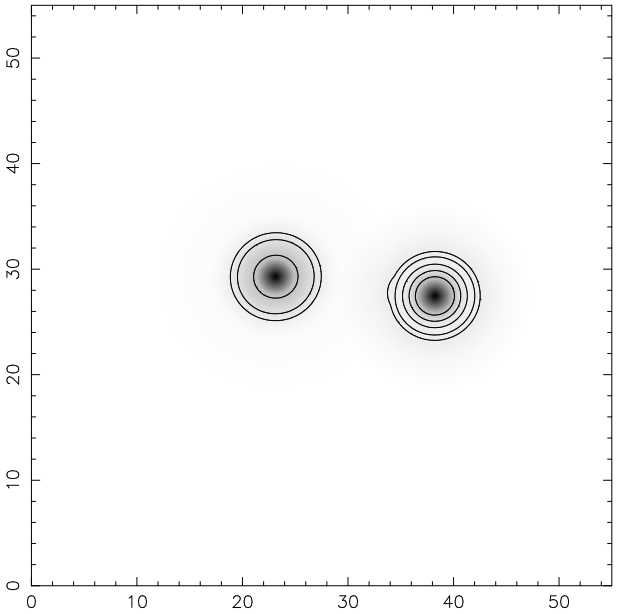

Figure 3.4: Fit of two elliptical King profiles to the simulation data in Fig. 3.2. The contours are at the same levels as in Fig. 3.2.

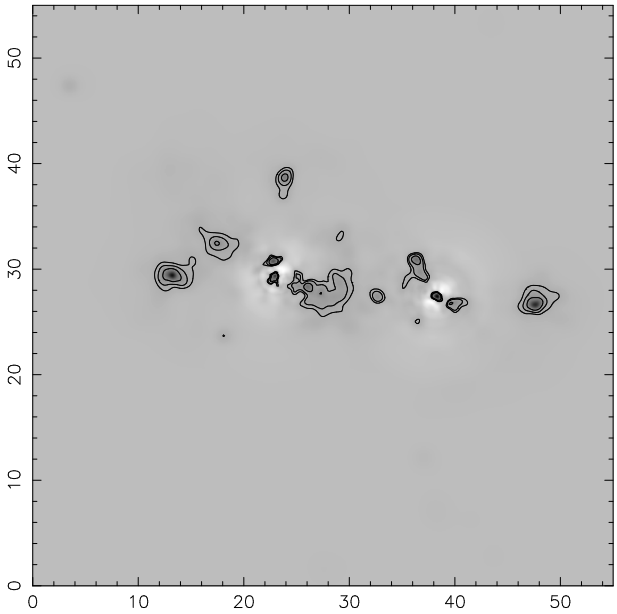

Figure 3.5: Difference image between the simulated data in Fig. 3.2 and the fit in the left panel. The contours are at the same level as in Fig. 3.2. Clearly visible is an excess in the surface mass density between the two clusters.

Figure 3.4 shows the fit of two elliptical King profiles to the simulated data displayed in Fig. 3.1. To reduce the computer time needed for the minimization, which is dominated by the repeated calculation of the integral (3.3), the data was smoothed on a 512×512 points grid instead of the 2048×2048 points grid which was used to calculate the lensing properties of the simulation. The weight function was chosen to be unity on the whole field.

Fig. 3.5 shows the difference between the simulated data in Fig. 3.2 and the fit to the simulation in Fig. 3.4. While the two clusters are not fitted perfectly – after all galaxy clusters are not perfect ellipses – most of the cluster mass is removed in the difference image. An overdensity of the surface mass density is visible between the two clusters, which supports the definition of the filament being the surface mass density that is in

excess of the elliptical cluster profiles.

However, the main problem in all fitting procedures is already visible here. Both clusters in the simulation have rather elliptical profiles. The orientation of the major axis of the left cluster is almost parallel to the 1–axis, while the major axis of the right cluster runs from the upper left to the lower right corner. Contrary to the simulation the fitted mass profiles are almost perfectly circular. Finding the right ellipticity and orientation seems to be the crucial difficulty in all fitting procedures.

3.3.2 Fitting Elliptical Profiles to the Reconstructed Surface Mass Density

While the fitting described in the previous section can be used as proof of concept that filaments can indeed be understood as mass that is in excess of elliptical profiles, the true surface mass density is not accessible in the case of observational data. If one wants to use the surface mass density to fit elliptical profiles, only the reconstruction is available.

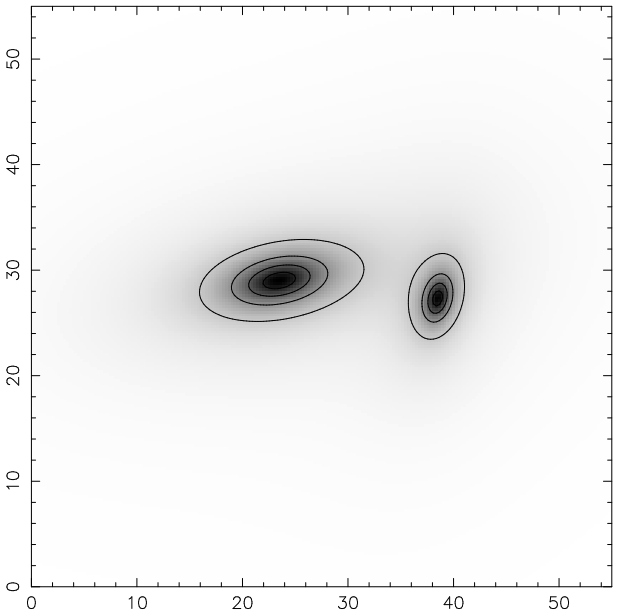

Figure 3.6: Fit of two elliptical King profiles to the reconstruction shown in Fig. 3.3. The contours are at the same level as in the reconstruction.

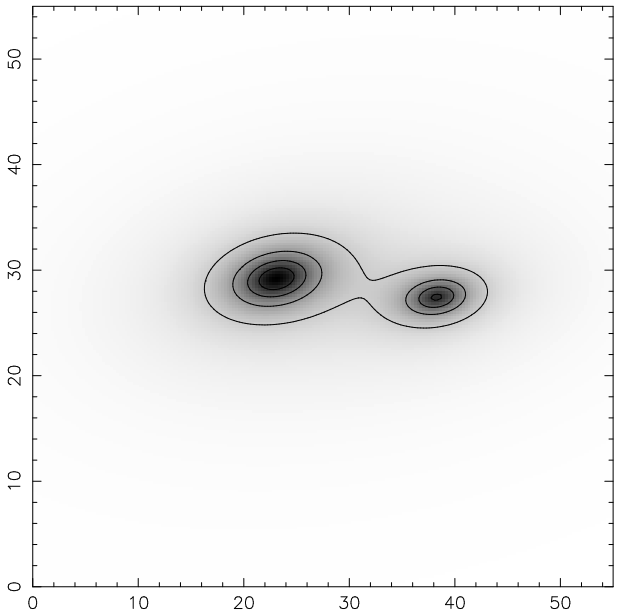

Figure 3.7: Same as Fig. 3.6 but with different starting value for the orientation of the right cluster.

Figures 3.6 and 3.7 show two such fits to the reconstruction displayed in Fig. 3.3. The only difference between both fits is the starting value for the orientation of the right cluster in the minimization procedure. Again, the weight function was chosen to be unity. One can clearly see the dependence of the orientation of the ellipses on the initial value. Even worse, although two completely different starting values were used, none of them lead to an orientation that is close to the actual orientation of the cluster.

I tried various weighting schemes in order to control this problem. E.g. only regions close to the cluster center were taken into account to reduce the influence of the noise further away from the clusters. None of this lead to more stable solutions. Also the attempt to use flexible radial profiles instead of the King profiles did not lead to positive results.

3.3.3 Fitting Non–Singular Isothermal Ellipses to the Shear

Although fitting elliptical profiles to the surface mass density seemed promising when done directly to the simulated data, it failed when reconstructed mass maps where used. Fitting directly to the ellipticities and avoiding the intermediate step of reconstructing the mass distribution may be a remedy for the problems described in the previous section.

An ellipsoidal density distribution for which the shear can be calculated analytically is that of a softened, oblate isothermal ellipse. Consider an oblate spheroid with axis ratio q_3. In projection this becomes an ellipsoidal density distribution with axis ratio $q = (q_3 \cos^2 i + \sin^2 i)^{1/2}$, i being the inclination angle with $i = 90°$ face–on and $i = 0°$ edge–on. If s is the core radius and $e = (1-q_3^2)^{1/2}$ is the eccentricity of the mass distribution, the density distribution for this model in cylindrical coordinates is

$$\rho = \frac{v_c^2}{4\pi G q_3} \frac{e}{\arcsin e} \frac{1}{s^2 + R^2 + z^2/q_3^2} \ , \tag{3.5}$$

(Keeton & Kochanek 1998). In the limit of $s = 0$ and $q_3 = 1$ this becomes the density distribution of a singular isothermal sphere (SIS). With $b_{\rm I} = (2\pi e D_{\rm ds} v_c^2)/(D_{\rm s} c^2 \arcsin e)$ the dimensionless surface mass density becomes

$$\kappa = \frac{b_{\rm I}}{2\sqrt{q^2(s^2 + \theta_1^2) + \theta_2^2}} \ . \tag{3.6}$$

Introducing the abbreviation $\Psi^2 = q^2(s^2 + \theta_1^2) + \theta_2^2$ the shear of this profile can be expressed as

$$\gamma_1 = k_1 \cos^2\phi - k_2 \sin^2\phi \ , \tag{3.7}$$

$$\gamma_2 = k_1 \sin^2\phi + k_2 \cos^2\phi \ , \tag{3.8}$$

where ϕ is the angle of the major axis of the ellipse with respect to the 1–axis and

$$k_1 = \frac{b_{\rm I}}{2\Psi}[\theta_2^2 - \theta_1^2 - (1-q^2)s^2]^2 \ , \tag{3.9}$$

$$k_2 = -\frac{b_{\rm i}}{\Psi}(\theta_1 \cos\phi + \theta_2 \sin\phi)(\theta_2 \cos\phi - \theta_1 \sin\phi) \ . \tag{3.10}$$

Unfortunately, it turned out that minimizing the quantity $\chi^2 = \sum_i |\varepsilon_i - \gamma(\vec{\theta}_i)|^2$ is extremely sensitive to the noise introduced by the random orientation of the FBG. While simulations based on catalogs with circular background galaxies gave reasonable results,

simulations based on the small value of $\sigma_\varepsilon = 0.2$ used here did not achieve reasonable fits and were extremely sensitive to the initial values.

Generally, a tendency to overfit the filament region, so that the difference image had negative surface mass density there, could be observed.

3.4 Using Aperture Multipole Moments to Quantify the Presence of a Filament

Aperture multipole moments (AMM) quantify the weighted surface mass density distribution in a circular aperture. If it is possible to find a characteristic mass distribution for filaments and express it in terms of multipole moments, AMM can be used to quantify the presence of a filament.

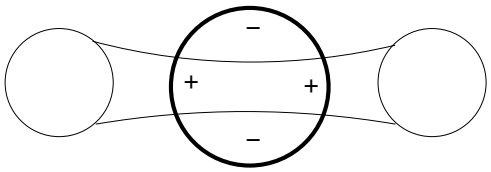

Figure 3.8: Simple toy model of two galaxy clusters connected by a filament. A quadrupole moment is present in the aperture centered on the filament.

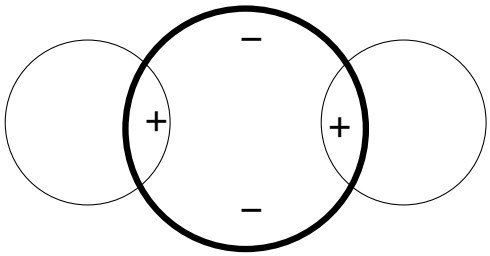

Figure 3.9: Toy model of two galaxy clusters without a filament, illustrating why it is important to choose the correct size of the aperture.

Fig. 3.8 illustrates with the help of a simple toy model of two galaxy clusters connected by a filament why one expects to find a quadrupole moment in an aperture centered on the filament. Fig. 3.9 illustrates that it is crucial not to choose the aperture too large. If the aperture also covers the clusters a quadrupole moment will be measured even if no filament is present.

Figures 3.10– 3.13 show quadrupole moment $|Q^{(2)}|$ maps calculated from simulated lensing data of the simulation shown in Fig. 3.2. The weight function was chosen to be

$$U(\theta) = \begin{cases} 1 - \left(\frac{\theta}{\theta_{\max}}\right)^2 & \theta \leq \theta_{\max} \ , \\ 0 & \text{else} \ . \end{cases} \tag{3.11}$$

While this weight function is clearly not ideal as it does not closely follow the mass profile of the simulated data, it is sufficient to identify all relevant features. In the quadrupole maps $\theta_{\max}$ increases from $2'$to $5'$. The maps were computed on 55×55 points grid, so that each grid point is $1' \times 1'$ big. Overlayed are the contours of the surface mass density of the reconstruction of Fig. 3.3.

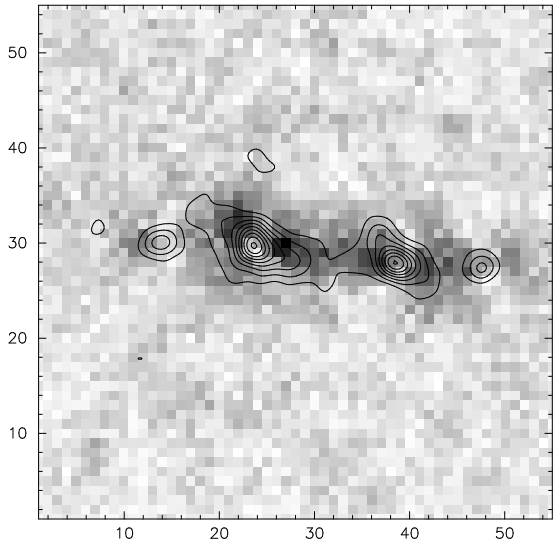

Figure 3.10: Quadrupole Moment of the simulation in Fig. 3.2 in a circle of $2'$ radius.

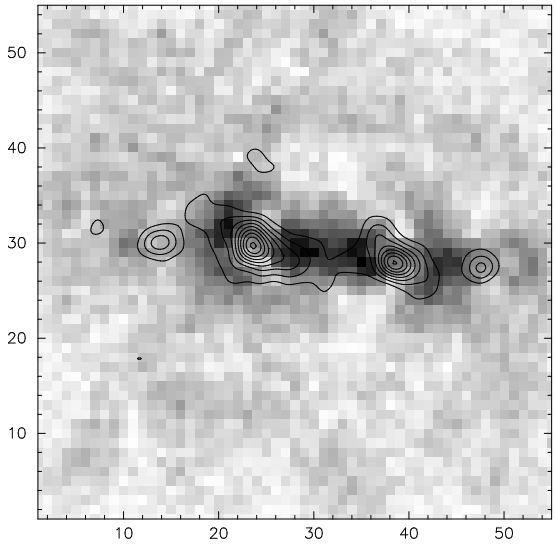

Figure 3.11: Same as Fig. 3.10 in a $3'$ radius circle.

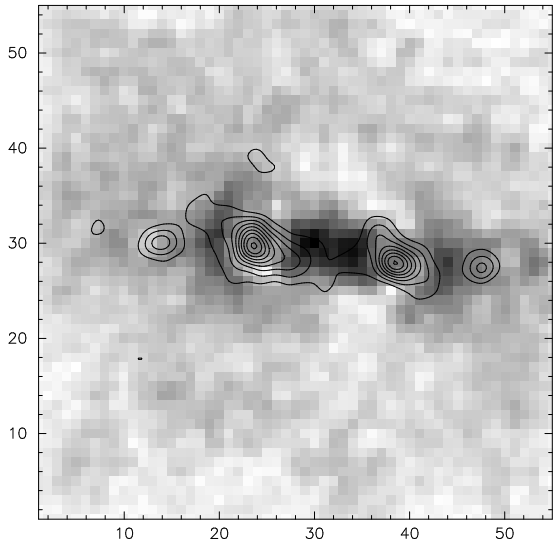

Figure 3.12: Same as Fig. 3.10 in a $4'$ radius circle.

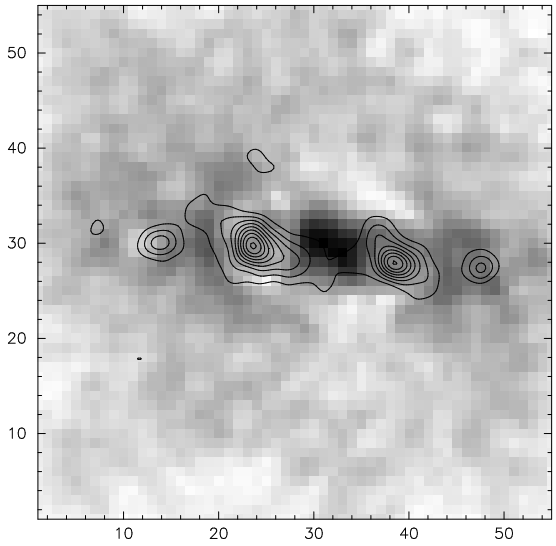

Figure 3.13: Same as Fig. 3.10 in a $5'$ radius circle.

One clearly sees that the quadrupole moment between the clusters increases as the size of the apertures increases. This is of course due to the growing portion of the clusters in the aperture, that with their large surface mass density dominate the mass distribution.

Most interesting for the quantification of filaments are the two maps in the top panel. The aperture quadrupole moment centered on the middle of the line connecting both clusters does not overlap with what one intuitively would call the galaxy clusters in these two maps. Noteworthy in Figs. 3.10 and 3.11 is also that they show a quadrupole moment on a ring–like structure around the cluster center. This is indeed to be expected for all galaxy clusters because there is a non–vanishing quadrupole moment if the aperture is not centered on the galaxy cluster, but somewhere on the slope of the mass distribution. This now raises the question how we should distinguish the quadrupole moment present around any cluster from that caused by a filamentary structure between the clusters.

The most obvious answer, that the quadrupole moment between the clusters has to exceed the quadrupole moment at the points having the same distance from the cluster center on the axis connecting both clusters outside the filament fails, due to the particular geometry of this simulation. The two small mass clumps to the left and the right of the clusters create a situation similar to that depicted in Fig. 3.9 and thus increase the quadrupole moment to the point where it is roughly equal to that in the filament center. Other simulations without this special geometry show no such behavior and the applicability of this criterion will be discussed below.

However, even in this special case there is evidence that the quadrupole signal in the center is caused by a filament and not by the clusters alone. This evidence is the asymmetry of the quadrupole moment around the galaxy clusters. An almost closed ring, on which the quadrupole moment is lower, is visible around the filament. This ring is easier is to spot in the maps generated from filter functions with larger radii. All aperture statistics act as bandpass filters on structure comparable in size to the filter radius. As the ring has a radius of $\sim 7'$ it is better visible in the maps generated from larger filters. Still, the asymmetry is well visible in Fig. 3.11 and less well visible but still present in Fig. 3.10. Thus, the quadrupole maps clearly indicate that the measured quadrupoles on the filament are not caused by a symmetric situation, that two galaxy clusters without filament would constitute.

The geometry of the simulation displayed in Fig. 3.14 is less peculiar than that of the previous simulation but poses other challenges to the quadrupole statistics. As can be seen in the figure, the surface mass density of the filament connecting both clusters is lower than that of the simulation in Fig. 3.2. A continuous filament is only visible because an additional contour line at $\kappa = 0.02$ was added. As a consequence only the small peak in the filament rising to $\kappa \simeq 0.03$ is visible in the reconstruction, but only at the level of the noise fluctuation, as we can infer from the spurious peaks in the lower left corner of Fig. 3.15.

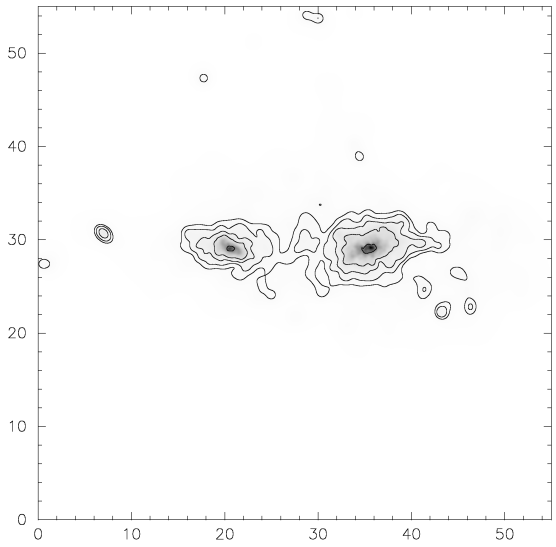

Figure 3.14: Smoothed surface mass density distribution of a second simulation. The projection parameters are the same as in Fig. 3.1. An additional contour line is drawn at $\kappa = 0.02$ because this filament is weaker.

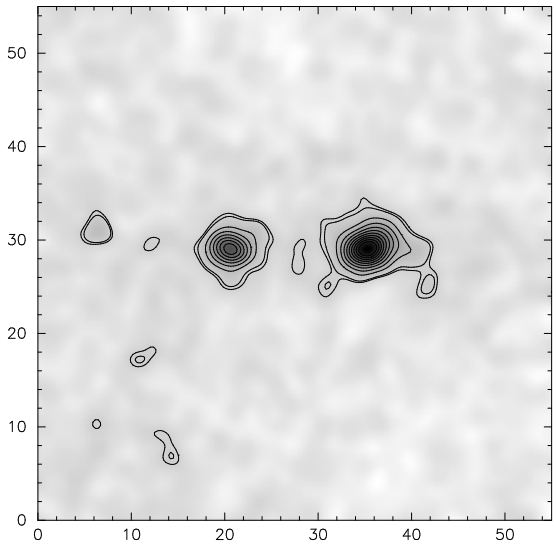

Figure 3.15: Same as Fig. 3.3 for the simulation in Fig. 3.14 with an additional contour at $\kappa = 0.02$.

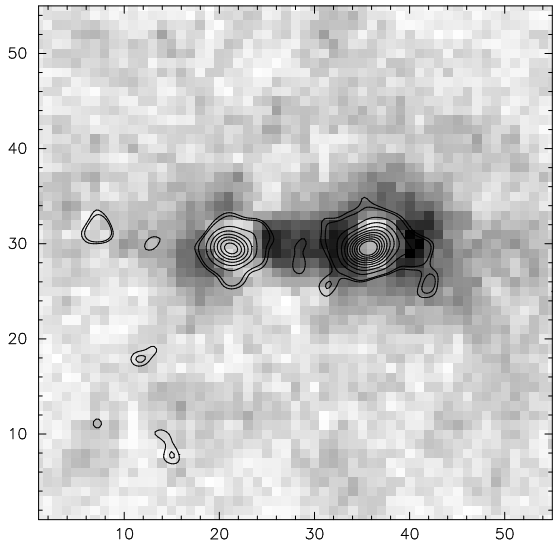

Figure 3.16: Aperture quadrupole moment in a $3'$ radius. Overlayed are the contours of Fig. 3.15.

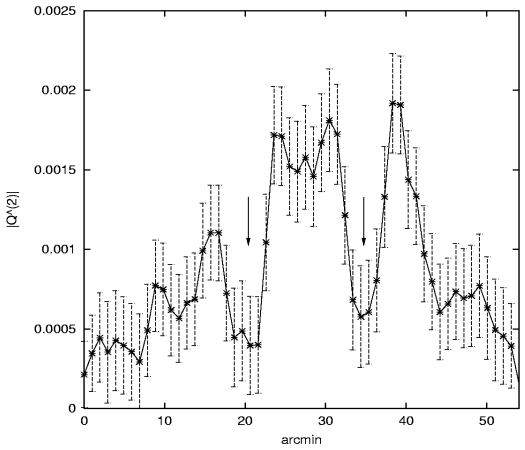

Figure 3.17: Absolute value of the aperture quadrupole moment along a line running through the centers of both clusters from the left edge to the right edge of Fig. 3.16. The arrows mark the cluster center.

Figure 3.16 shows a quadrupole map from simulated lens data for this simulation. The aperture quadrupole moment was computed in a $3'$ radius. Again the size of the aperture was chosen such that the aperture in the middle between both clusters does not cover what one intuitively would identify as part of the clusters. The two lowest contours, which are partly covered by the aperture in the filament center, do not belong to the region that obviously belongs to the cluster.

Again we see a quadrupole moment on the filament and around the galaxy clusters. As there are no small mass clumps on the connecting axis outside the clusters we can test the hypothesis that the quadrupole moment in the filament region exceeds the quadrupole moment on the corresponding point on the cluster slope. Fig. 3.17 shows the absolute value of the quadrupole moment in Fig. 3.16 along a line running through both cluster centers from the left edge of the image to the right. Points which are not exactly on a grid point were approximated by linear interpolation. The same was done for the error bars, which were calculated from 1000 randomizations of the galaxy orientations. The points are connected by straight lines.

Clearly visible is the broad central double peak on the filament bounded by the two minima of the cluster centers. The quadrupole moment on the slope of the left, less massive cluster is well below that of the filament. The center of the filament corresponds to the small minimum left of the little "bump" in the middle of the broad double peak (at $\sim 27'$). Although the maximum of the quadrupole moments is on the outer slope of the massive right cluster, the quadrupole moment having the same distance from the cluster center as the filament center is below the value in the filament center (at $\sim 43'$).

The double peak structure of the quadrupole moment on the filament is probably caused by the small mass concentration in the filament. The quadrupole moment in aperture centered on this peak will be lower than that of aperture which covers this peak and already part of the cluster and thus leads to a situation comparable to that of Fig. 3.9 with one cluster replaced by the small peak.

It is interesting to note that the quadrupole statistics gives a positive result if the reconstruction fails to show a filament. In fact, until now I have ignored the possibility that the clusters could have filamentary extensions that do not join. An observer not knowing

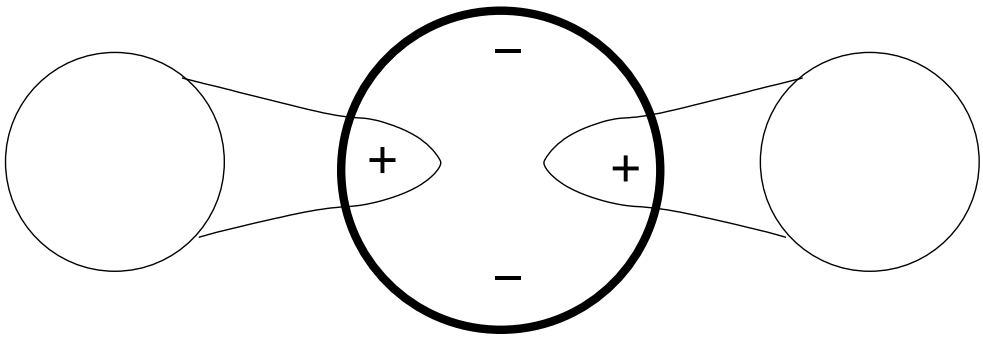

Figure 3.18: Quadrupole moment of filamentary extensions of cluster that do not join.

the true mass distribution of Fig. 3.14 would conclude to observe the case illustrated in Fig. 3.18. This example shows, that while the quadrupole moments can be used to quantify the significance of a filament by computing the significance of the quadrupole moment, measuring a quadrupole moment alone is not sufficient. Ideally, the filament is also visible (and significant) in a map of the aperture mass with the same filter radius.

3.4.1 Defining Cluster and Filament Regions

While in the (failed) attempt to separate the clusters and the filament by fitting elliptical profiles to the clusters, the filament was naturally defined as the surface mass density excess above the clusters, there is no criterion in the AMM statistics that defines cluster and filament regions. Much of the discussion of the quadrupole statistics in the last section was based upon "intuitive separation" of clusters and filament. That this can be problematic in many cases can be seen from the simulation in Fig. 3.14. While the contours show a continuous connection between the clusters, one could argue that the clusters in this simulation overlap. The cluster on the right in this simulation has a mass extension to the right, whose maximum spatial extension from the cluster center is comparable to the distance of the peak in the filament from the cluster center. The situation for the cluster on the left is approximately the same. This illustrates the need for a more objective criterion to separate the clusters from a possible filament, which I try to develop in this section.

Fig. 3.19 shows a simple one–dimensional toy model of the mass distribution of a cluster with a filamentary extension. The model consists of the following components: We assume a cluster with a King profile. This is the solid line in Fig. 3.19. In all simulations we see that the clusters are not circular but stretched and have their major axes oriented approximately towards each other. I attribute this to tidal stretching and account for it in the model by stretching the right half of the King profile (long dashed line) by a factor, which has to be determined. This factor will be called the "stretch factor". The contribution of the filament (dotted line) is added to the stretched King profile. The result is the observed surface mass density profile on the right–hand side (short dashed).

I tried to define the "start" of the filament and the "end" of the cluster by the following procedure: The unstretched King profile, observed on the left–hand side, is stretched by a factor, to model the influence of tidal stretching. By this step we try to obtain the (unobservable) cluster profile on the right side without the contribution of the filament. This stretched profile is then compared to the observed profile containing the contribution of the filament by computing the goodness of fit

$$\chi^2 = \sum_{i=i_0}^{N} \left(\frac{\kappa_{\mathrm{stretch}}(\theta_i) - \kappa_{\mathrm{true}}(\theta_i)}{\sigma_i} \right)^2 , \tag{3.12}$$

at sample points θ_i in the reconstruction along the main axis of the system. σ_i is the estimated error in κ at the ith point and the summation is carried out from the i_0th point to the Nth point. χ^2 is repeatedly computed for increasing values of N. Unless noted otherwise, $i_0 = 1$. We can define the end of the cluster and the start of the filament by the

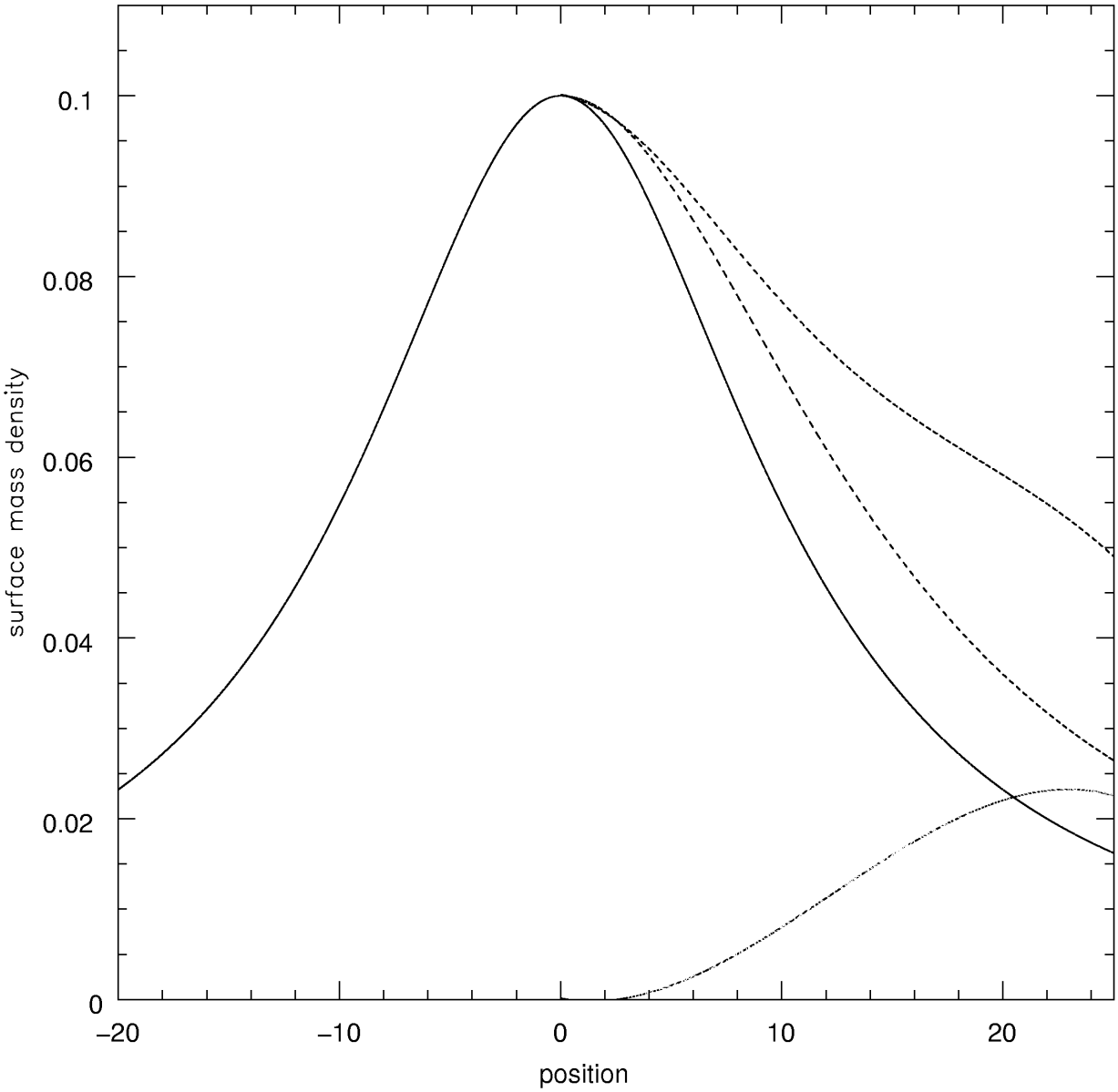

Figure 3.19: Simple model of the surface mass density distribution of an elliptical cluster and a filamentary extension along the main axis of the system. The axes are labeled in arbitrary units.

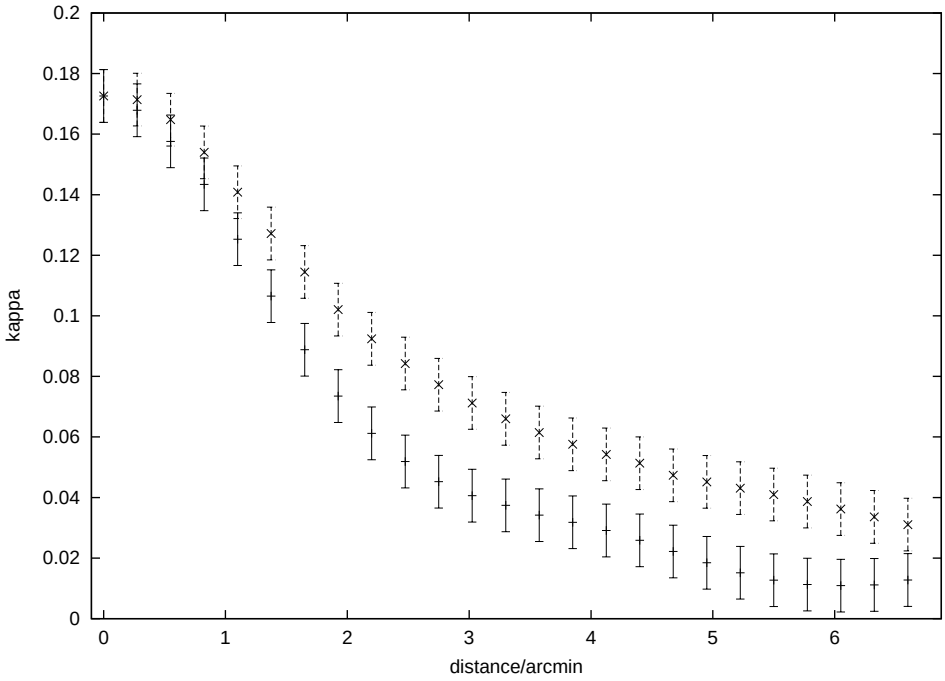

Figure 3.20: Surface mass density profiles of the cluster on the left in the reconstruction displayed Fig. 3.3 along the main axis of the system. The crosses mark the surface mass density in the filament part, the dashes the surface mass density on the lefthand side of the cluster. The x–axis denotes the distance from the cluster center in arcminutes.

point N, where the probability that $\kappa_{\rm stretch}$ is a good representation of $\kappa_{\rm true}$ falls below a predefined level ("cut–off confidence level").

We now have to find a way to determine the stretch factor. I assume that the inner portion of the observed profile on the right–hand side is a fair representation of the (unobservable) stretched profile. The stretch factor can then be determined by fitting the unstretched profile to the inner portion of the observed profile. This "stretch factor fit" was done using a χ^2 minimization with linear interpolation between the observed sample points. The size of the inner region to be used in the stretch factor fit was measured in units of the core radius of the unstretched profile. Its value is called the "cut–off parameter".

The cut-off parameter and the cut–off confidence level have to be determined from simulations. Figure 3.20 shows the mass profiles to the left and right of the center of the cluster on the left in the reconstruction displayed in Fig. 3.3 along the main axis of that system. For simplicity the error bars were assumed to be equal to the standard deviation of a reconstructed mass map of a randomized catalog of background galaxies.

I determined several combinations of the cut–off parameter and confidence level that match the visual impression of filament beginning and cluster end. However, if these were applied to other clusters, the separation point between cluster and filament was placed at non–sensical positions.

I also modified the starting value i_0 in the summation in eq. (3.12). First, I placed it at the point closest to the cut–off parameter of the stretch factor fit in order to exclude the central region, which by definition of this procedure has a small χ^2. Second, I calculated χ^2 in a moving window of fixed size and set the separation point between cluster and filament to the start of the window for which χ^2 fell below the cut–off confidence level. This was done for various window sizes and confidence levels. Again, parameters that worked well for one cluster failed horribly for others.

Chapter 4

Spectroscopy of the Abell 222 and Abell 223 System

Spectroscopy allows us to study the properties of the luminous part of galaxies and galaxy clusters more precisely than any other method. Multi–object spectroscopy (MOS) allows the simultaneous acquiration of large numbers of galaxy spectra. With extensive spectroscopic data at hand, it is possible to study the spatial and kinematic properties of the visible component of galaxy clusters.

In the following I will describe the spectroscopic and photometric data of Abell 222 and Abell 223, its reduction, and the spatial and kinematic properties we can derive from this data. Essentially this chapter is the same as Dietrich et al. (2002), section 4.2.4 was mainly written by Douglas Clowe and is reproduced here to provide the necessary information on the reduction of the wide field images and the photometry performed on them.

Throughout this chapter I assume a $\Omega_\Lambda = 0.7$, $\Omega_\mathrm{m} = 0.3$, $H_0 = 70\ h_{70}$ km s^{-1} Mpc^{-1} cosmology.

4.1 Overview of the Abell 222 and Abell 233 System

Abell 222 and Abell 223 are a close pair of two rich galaxy clusters, both having Abell richness class 3 (Abell 1958), separated by $18'$, which at the cluster redshift of ~ 0.21 corresponds to 2600 h_{70}^{-1} kpc. Their Bautz–Morgan (Bautz & Morgan 1970) types are II–III (A 222) and III (A 223). While these are optically selected clusters, they have been observed by ROSAT (Wang & Ulmer 1997; David et al. 1999) and are confirmed to be massive clusters. 9 spectra of galaxies in the cluster region, most of them being cluster members, were known (Sandage et al. 1976; Newberry et al. 1988) before Proust et al. (2000) published a list of 53 spectra and did a first kinematical study of this system. Proust et al. also found 4 galaxies at the cluster redshift in the region between the clusters (hereafter "intercluster region"), indicating a possible connection between the clusters.

4.2 Data and Data Reduction

Multi–object spectroscopy of the two clusters Abell 222 and Abell 223 was performed at the NTT on three consecutive nights in December 1999. The instrument used was EMMI with grism 2, which has a dispersion of 11.6 nm/mm. With the 2048x2048 CCD pixels of 24 μm this leads to a dispersion of 0.28 nm/pixel. With one exception two exposures of 2700 seconds each were taken for 6 fields, 3 on each cluster. For the field centered on A 222 in the second night only one exposure of 2700 seconds was available. The wavelength calibration was done using Helium–Argon lamps. The calibration frames were taken at the beginning of the night for the masks used during that night, before the science exposures were made.

4.2.1 Reduction of Spectroscopic Data

For the data reduction a semi-automated IRAF[1] package was written by me that cuts out the single spectra of the CCD frames and then processes these spectra using standard IRAF routines for single slit spectroscopy. To determine the wavelength–dependent detector response and correct for non–uniform sensitivity across the CCD, "flatfield" spectra of a uniformely illuminated plane in the telescope dome were taken.

All ground–based spectroscopic observations are superposed with the spectrum of the night sky. The sky spectrum was removed from all spectra using a linear fit with a 2σ rejection on measurements on each side of the galaxy spectrum where the position of the galaxy on the slit permitted it. Measurements from only one side of the spectrum were used otherwise. A 2σ rejection was used in the coaddition of the two frames to remove cosmic rays and hot pixels. Remaining hot pixels or cosmic rays in the sky spectrum introduced fake absorption features, while hot pixels or cosmic rays in the spectrum itself lead to fake emission features. These were removed by hand.

Because the sky spectrum removal was done column by column and no distortion correction was applied, some residual sky lines remained in the final spectra, most notably the strong [O I] emission at 5577 Å. At the typical redshift of the cluster members of $z \approx 0.21$ this line does not coincide with any important feature and thus does not cause any problems in the subsequent analysis.

4.2.2 Redshift Determination

The radial velocity determination was carried out using the cross-correlation method (Tonry & Davis 1979) implemented in the RVSAO package (Kurtz & Mink 1998). Spectra of late type stars and elliptical galaxies with known radial velocities were used as templates. The redshift determination was verified by visual inspection of identified absorption and emission features.

[1]IRAF is distributed by the National Optical Astronomy Observatories, which are operated by the Association of Universities for Research in Astronomy, Inc., under cooperative agreement with the National Science Foundation.

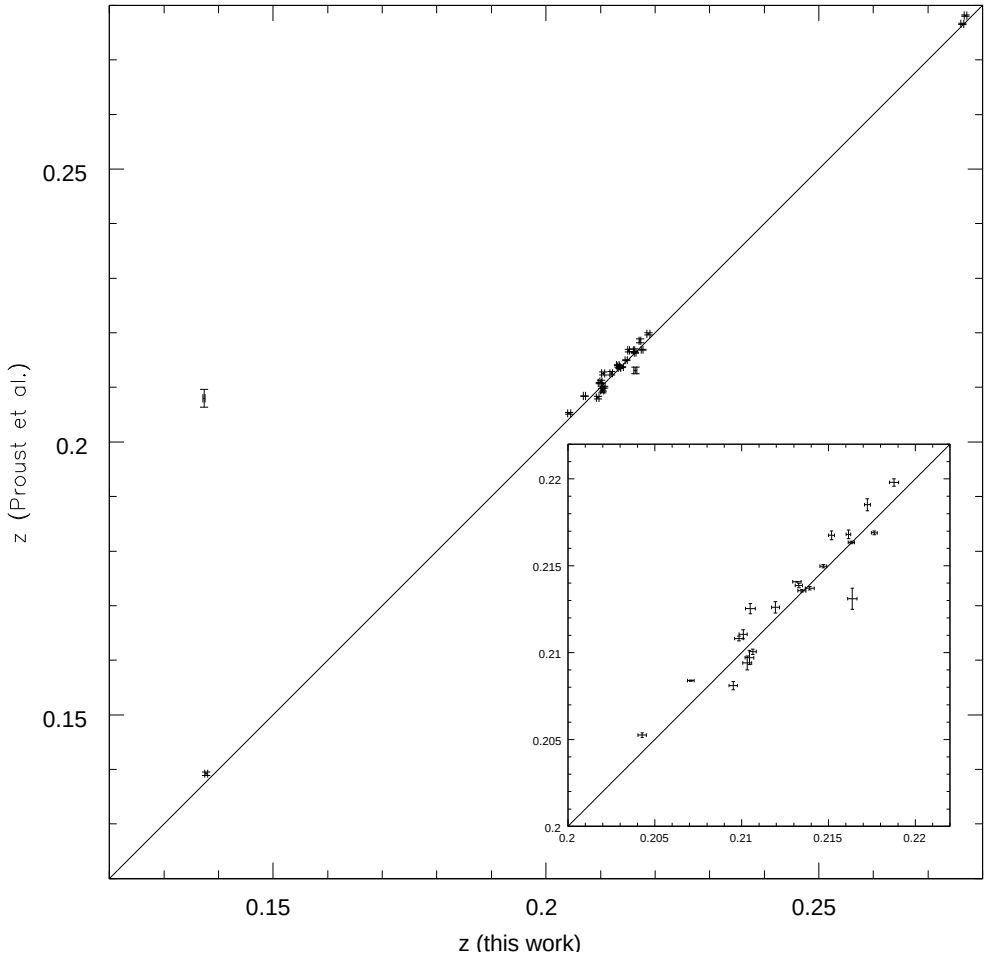

Figure 4.1: Comparison of redshift measurements for objects observed by us and with redshifts listed in PEL. The large panel shows the full sample, the inset is a blow up of the cluster region. See the text for details.

Fig. 4.1 shows a comparison of our redshift measurements and the redshifts listed by PEL. The obvious outlier in the large panel is from the sample of Sandage et al. (1976). Although the inset shows a broad agreement between our results and the values of PEL, only 3 out of 22 redshifts coincide within the 1σ error. Also, Student's t-test confirms the hypothesis of different sample means with same variance at higher than the 99% level for all their and our cluster members.

We ruled out the possibility that this discrepancy could have been caused by taking all calibration frames before the science exposures were taken. This could have introduced a shift of the zero point if the masks were not moved back to their original position for the science exposures. We confirmed that this is not the case by determining the radial velocity of the subtracted sky spectrum in the wavelength calibrated frames. We found that, if a zero point shift occurred, it must be smaller than 30 km s^{-1}. Clearly, this is not

enough to explain the differences with PEL which are up to 500 km s^{-1}.

4.2.3 Equivalent Widths

We measured equivalent widths for the [O II]λ3727, [O III]λ5007 emission lines, and Hβ and Hα emission and absorption lines. [O II] and Hα are important indicators of star formation rates (Kennicutt 1998).

To accurately determine the equivalent widths and in particular estimate their significance level we follow the definition of equivalent widths given by Czoske et al. (2001):

$$W_\lambda = \sum_{i=1}^{N_{\rm int}} \frac{f_i}{\bar{f}_{\rm c}} \Delta\lambda - N_{\rm int}\Delta\lambda, \tag{4.1}$$

where f_i is the flux in pixel i, $N_{\rm int}$ is the number of pixels in the integration ranges, $\bar{f}_{\rm c}$ is the continuum level estimated as the weighted mean of continuum regions on either side of the line, and $\Delta\lambda$ is the dispersion in Å/pixel. Note that with this definition emission lines have *positive* equivalent widths. The integration ranges for the features and the continuum were fixed by the values given in table 4.1, their meaning is illustrated in Fig. 4.2.

Table 4.1: Rest–frame wavelength ranges for equivalent widths measurement. All wavelengths are given in Å. The last column gives the continuum range that was used for estimating the signal–to–noise ratio.

Feature	$\lambda_{\rm cent}$	line	blue cont.	red cont.	SNR
[O II]	3727	3713 - 3741	3653 - 3713	3741 - 3801	3560 - 3680
[O III]	5007	4997 - 5017	4872 - 4932	5050 - 5120	4450 - 4750
Hβ	4861	4830 - 4890	4800 - 4830	4890 - 4920	4050 - 4250
Hα	6563	6556 - 6570	6400 - 6470	-	6300 - 6450

The significance of an equivalent width measurement is given by (Czoske et al. 2001)

$$\sigma^2_{W_\lambda} = \left(\frac{S}{N}\right)^{-2} \left[\left(W_\lambda + N_{\rm int}\Delta\lambda\right)\Delta\lambda + \frac{\left(W_\lambda + N_{\rm int}\Delta\lambda\right)^2}{N_{\rm c}} \right], \tag{4.2}$$

$S/N = \bar{f}_{\rm c}/\sigma_{\rm c}$ being the signal–to–noise ratio, where $\bar{f}_{\rm c}$ is the mean continuum in the $N_{\rm c}$ pixels in the SNR wavelength range given in table 4.1, and $\sigma_{\rm c}$ is the rms dispersion in that region.

All wavelengths are given in the restframe of the object. All spectra were normalized to a continuum fit before equivalent widths were measured. The catalog lists all [O II] and [O III] emission features and all Hβ and Hα emission and absorption features that were detected with a significance $> 2\sigma$.

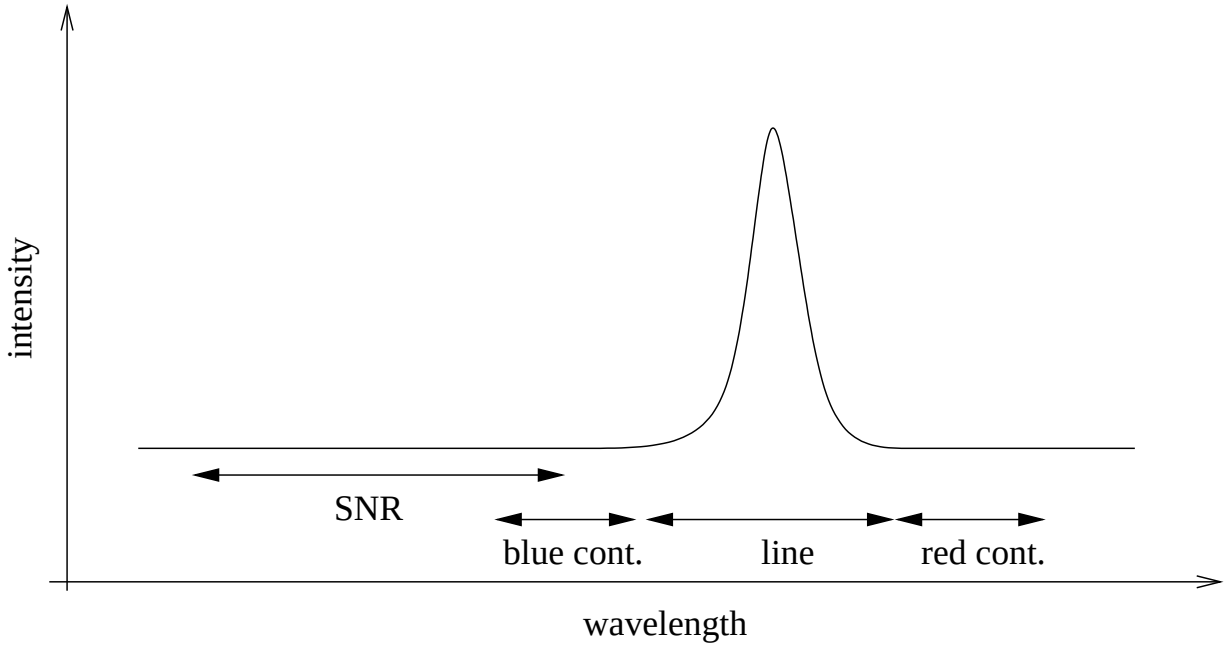

Figure 4.2: Illustration of the signal–to–noise, line, and continuum regions of Table 4.1.

4.2.4 Photometry

Wide-field imaging of the cluster pair was performed over two nights in December 1999 with the Wide Field Imager (WFI) on the ESO/MPG 2.2m on La Silla. The WFI is a mosaic CCD camera consisting of 8 CCD detectors with 2048×4096 pixels each in a 4×2 arranged in a 4×2 array. Eleven 900 second exposures in R-band and three 900 second exposures in V band were taken using a dithering pattern which filled the gaps between the CCDs in the mosaic in the coadded image. The reduction was carried out using a combination of self–written routines and routines which are part of the IMCAT software package written by Nick Kaiser (`http://www.ifa.hawaii.edu/~kaiser/imcat`). The images were flattened with medianed night-sky flatfields from all the R or V band long exposure images taken over the two nights. The images were aligned using a process which assumes each CCD in the mosaic can be translated to a common detector-plane coordinate system using a linear transformation of coordinates (a shift in both axes and rotation allowed) and that the detector-plane coordinates can then be transformed into sky coordinates using a two dimensional polynomial, in this case a bi-cubic polynomial. The linear transform from each CCD to the detector-plane is assumed to be constant for all the images whereas the transform from detector-plane to sky coordinates is determined separately for each image to allow for both the pointing offsets in the dithering pattern and any changes in the distortion pattern between images. By comparing the positions of stars among the individual images and to the positions in the USNO catalog[2] (Monet

[2]The USNO catalog is a catalog of astrometric standards containing positions of 526,230,881 objects.

et al. 1998), both systems of equations for coordinate transformations were solved using χ^2 minimization of the final stellar positions. The rms dispersion of the centroids of the stars used in the fitting were $0\farcs016$ among the input images and $0\farcs54$ between the input images and the USNO coordinates, with the average offset vector being consistent with zero in all regions of the image. Further details of this technique along with justifications for the linear translation between CCD and detector plane can be found in Clowe & Schneider (2001). The mapping of each input CCD was performed using a triangular method with linear interpolation which preserves surface brightness if the mapping changes the area of a pixel. The resulting images were then averaged using a 3σ clipping algorithm to remove cosmic rays and moving objects. The final R-band image can be found in Figure 4.8.

Objects were detected in the R-band image using SExtractor (Bertin & Arnouts 1996), and the V-band magnitudes for the objects were measured using SExtractor in two–image mode. The two–image mode of SExtractor performs parallel measurements on two images. Objects are detected in one image and their properties are determined separately in both images. The FWHM of bright but unsaturated stars in the coadded images are $0\farcs87$ for R and $1\farcs05$ in V. Zeropoints were measured from Landolt standard fields (Landolt 1992), but the V-band data is known to have been taken in non-photometric conditions. From isolating the red cluster galaxy sequence in a color-magnitude plot (Fig. 4.3), corrected for the $A_B = 0.086$ mag dust extinction (Schlegel et al. 1998) using the conversion factors from Cardelli et al. (1989), and comparing to predicted colors of cluster elliptical galaxies in a passive evolution model (Fukugita et al. 1995), a correction of -0.23 mag has been applied to the V magnitudes to correct for the additional atmospheric extinction. This correction also causes the stellar $V - R$ colors to have the theoretically expected values (Gunn & Stryker 1983). All magnitudes are isophotal magnitudes with the limiting isophote at 27.96 mag. We determine the completeness limit of the photometric catalog to be at $R = 24$ mag from the point where the number counts of objects stop following a power law.

The full catalog containing positions, R magnitudes and $V - R$ color, equivalent widths for the lines in table 4.1, and heliocentric redshifts is available in appendix A.

SExtrator also provides an algorithm to separate galaxies from stars. Each object is assigned a CLASS_STAR value, which is 1 for stars, 0 for galaxies, and lies in between for ambiguous objects.

4.3 Spatial Distribution and Kinematics

After removing some obvious background and foreground galaxies ($z > 0.3$ or $z < 0.1$), the mean and dispersion values of the tentative cluster members were calculated. Galaxies that were more than 3σ away from the mean were removed. This process was repeated until no more galaxies were deleted from the sample. We found 81 galaxies belonging to Abell 222 and 72 galaxies belonging to Abell 223 or the possible bridge connecting both clusters.

The mean redshift of the individual clusters are $z = 0.2126 \pm 0.0005$ and $z = 0.2079 \pm$

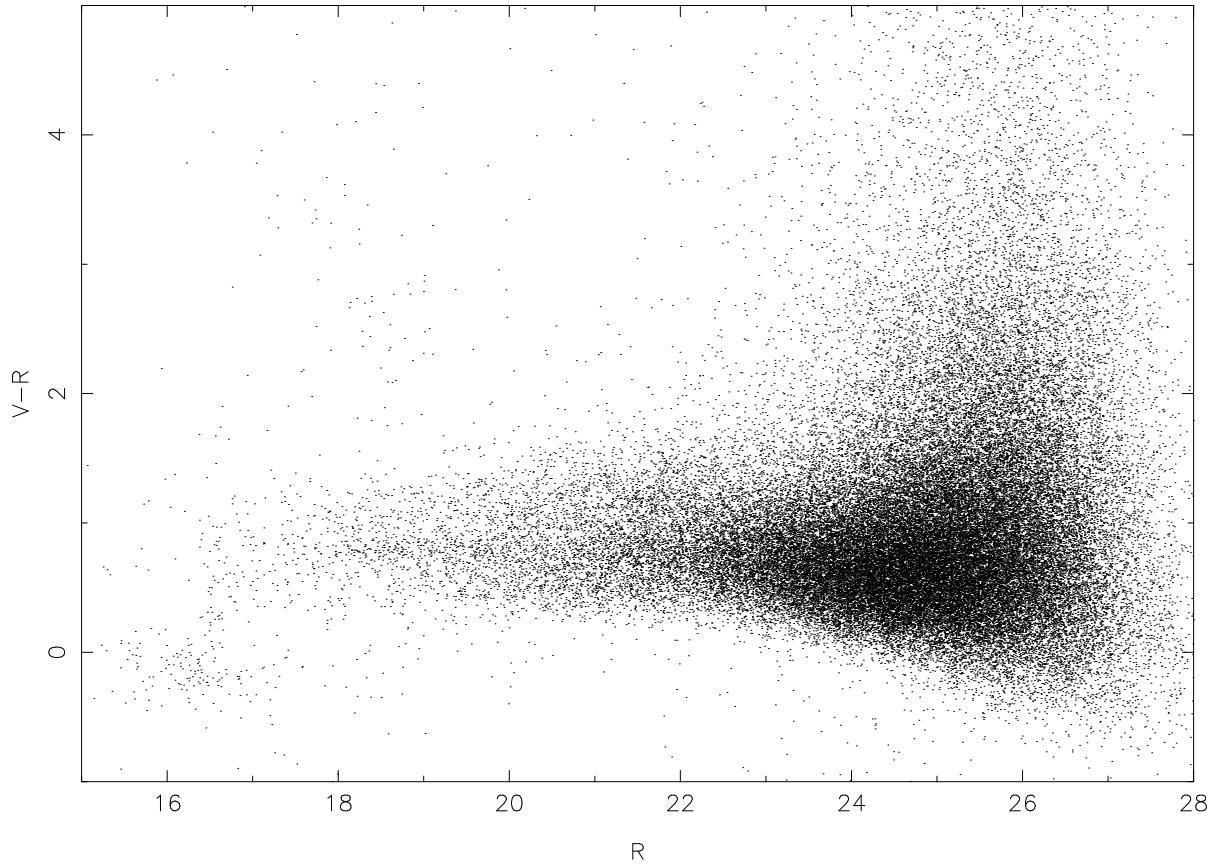

Figure 4.3: Color–magnitude plot with the already corrected V magnitudes. The red cluster sequence is centered around $V - R = 0.8$.

0.0005, for A 222 and A 223, respectively. The measured velocity dispersions have to be transformed to the restframe of the cluster according to the transformation law

$$\sigma_{\rm cor} = \frac{\sigma}{1+\overline{z}} \ , \tag{4.3}$$

(Harrison 1974). The rest–frame velocity dispersions for the individual clusters are $\sigma_{\rm cor} = 1014^{+90}_{-71}$ km s^{-1} and $\sigma_{\rm cor} = 1032^{+99}_{-76}$ km s^{-1}, for A 222 and A 223, respectively. The redshift and velocity dispersion for A 223 do not change significantly if the 3 galaxies we found in the intercluster region in our sample are removed. Figs. 4.4 to 4.7 show the corresponding radial velocity distributions of the individual samples.

These values for the velocity dispersion are somewhat higher than those derived from X–ray luminosities. David et al. (1999) report bolometric luminosities of $L_{\rm X} = 7.65 \times 10^{44}$ erg s^{-1} and $L_{\rm X} = 6.94 \times 10^{44}$ erg s^{-1} from ROSAT PSPC observations for A 222 and A 223, respectively, for $H_0 = 50$ km s^{-1} Mpc^{-1}. Using the $L_{\rm X}$–σ relationships of Wu et al. (1999) we get $\sigma_{\rm X} = 845 - 887$ km s^{-1} for A 222 and $\sigma_{\rm X} = 828 - 871$ km s^{-1} for A 223.

Together with the data of PEL we now have radial velocities for 6 galaxies in the

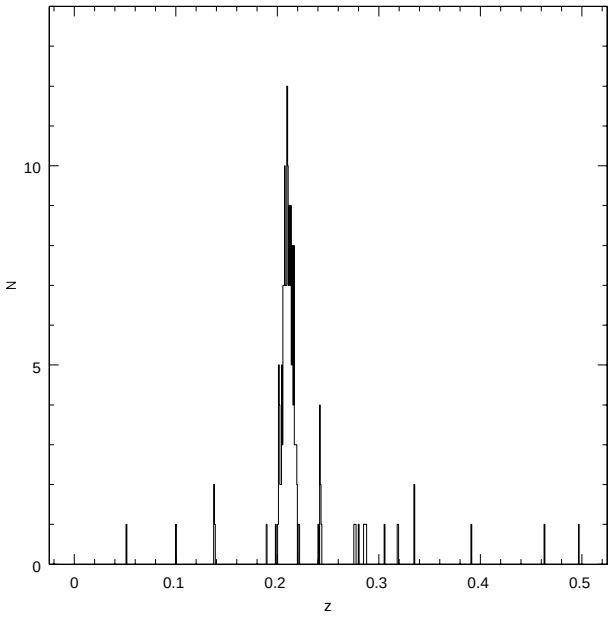

Figure 4.4: Radial velocity distribution of all galaxies in the sample. The main peak corresponds to the two Abell clusters.

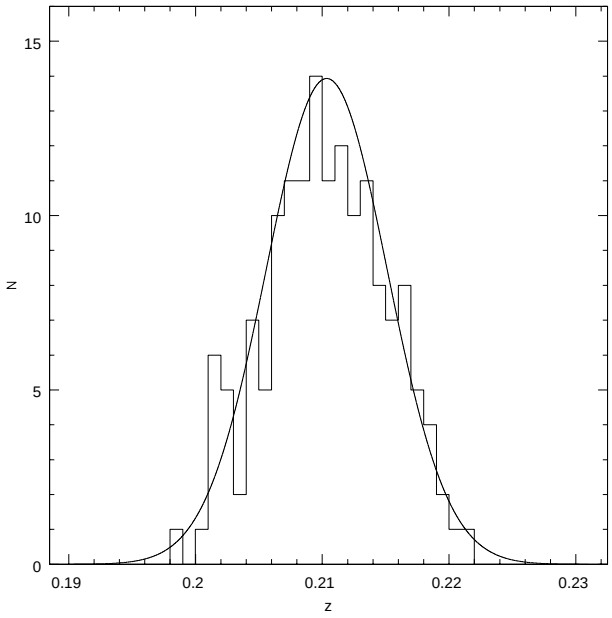

Figure 4.5: Radial velocity distribution of all cluster galaxies. The continuous line is a Gaussian with mean and dispersion value $z = 0.2104 \pm 0.0004$ and $\sigma = 1424^{+90}_{-75}$ km s^{-1}, corresponding to $\sigma_{\rm cor} = 1177^{+74}_{-62}$ km s^{-1}.

possible bridge connecting both clusters. With our new values for the radial velocity of A 223 the observation made by PEL that most of the bridge galaxies are in the low–velocity tail does not hold anymore. In fact they all appear to be close to the maximum or at higher redshift of the velocity histogram shown in figure 4.7. Because A 222 is the cluster at higher redshift, this is the expected behavior should these galaxies indeed belong to a bridge connecting both clusters

Although the difference in radial velocity determination between PEL and our data is significant, the decision about cluster membership of individual galaxies is unambiguous. Figure 4.8 displays a projected galaxy number density map generated with the adaptive kernel density estimate method described by Pisani (1996) for a color selected sample of 693 objects with $R < 21$ and $0.7 < V - R < 0.9$ and SExtractor CLASS_STAR < 0.1 from the WFI images. Overplotted are the positions of all spectroscopically identified cluster members. Fig. 4.8 clearly exhibits two density peaks in A 223. Both peaks are separated by $4\farcm8$ and are centered at (α=01:37:53.5, δ=−12:49:21.2) and (α=01:38:01.8, δ=−12:45:07.0). These peaks are also visible in the density distribution of the 181 spectroscopically identified cluster galaxies. Also visible is an overdensity of color selected objects in the intercluster region, hinting at a connection between both clusters.

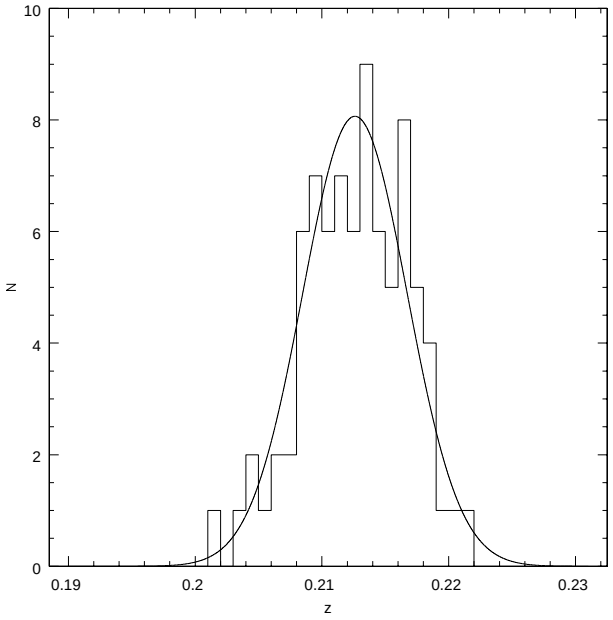

Figure 4.6: Same as Fig. 4.5 for A 222.

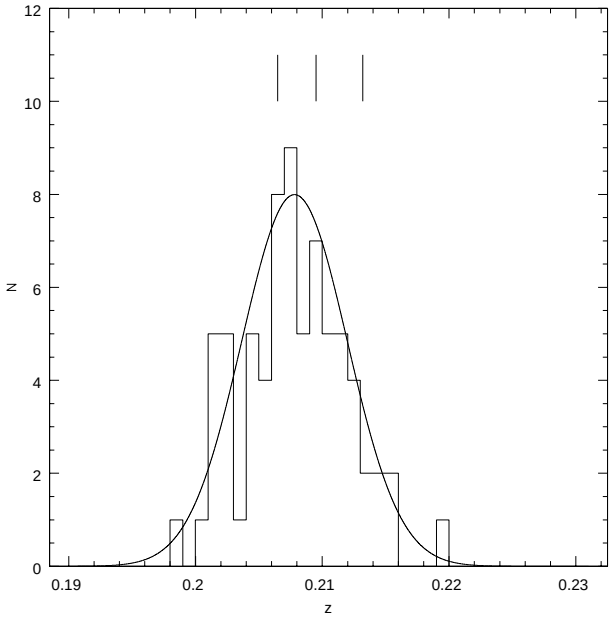

Figure 4.7: Same as Fig. 4.5 for A 223. The dashes denote the 3 galaxies in the bridge for which we measured radial velocities.

We applied the Dressler & Shectman (1988, DS) test for kinematic substructure in the projected galaxy distribution. The DS test aims at finding radial velocities and/or velocity dispersions that in a limited spatial region deviate significantly from the mean radial velocity and/or velocity dispersion of the whole cluster sample. The local values of the mean redshift and velocity dispersion are calculated for each of the N galaxies and its $n-1$ nearest neighbors and compared to the global values. The statistics used to quantify the presence of substructure is

$$\begin{aligned} \Delta &= \sum_{i=1}^{N} \delta_i \\ &= \sum_{i=1}^{N} \left\{ \frac{n}{\sigma^2_{\rm glob}} \left[(\bar{z}_{\rm glob} - \bar{z}_{{\rm loc}_i})^2 + (\sigma_{\rm glob} - \sigma_{{\rm loc}_i})^2 \right] \right\}^{\frac{1}{2}} , \end{aligned} \tag{4.4}$$

where $\overline{z}_{\rm glob}$ and $\sigma_{\rm glob}$ are the mean redshift and velocity dispersion of the whole sample, respectively, and $\overline{z}_{{\rm loc}_i}$ and $\sigma_{{\rm loc}_i}$ are the local values of the mean redshift and velocity dispersion of the ith galaxy and its $n-1$ nearest neighbors, respectively. For a Gaussian velocity distribution and only random local fluctuations $\Delta \sim N$. To decide whether a computed Δ indeed is due to kinematic substructure without making assumptions about the parent population, the Δ statistics is calibrated by randomly shuffling the radial ve-

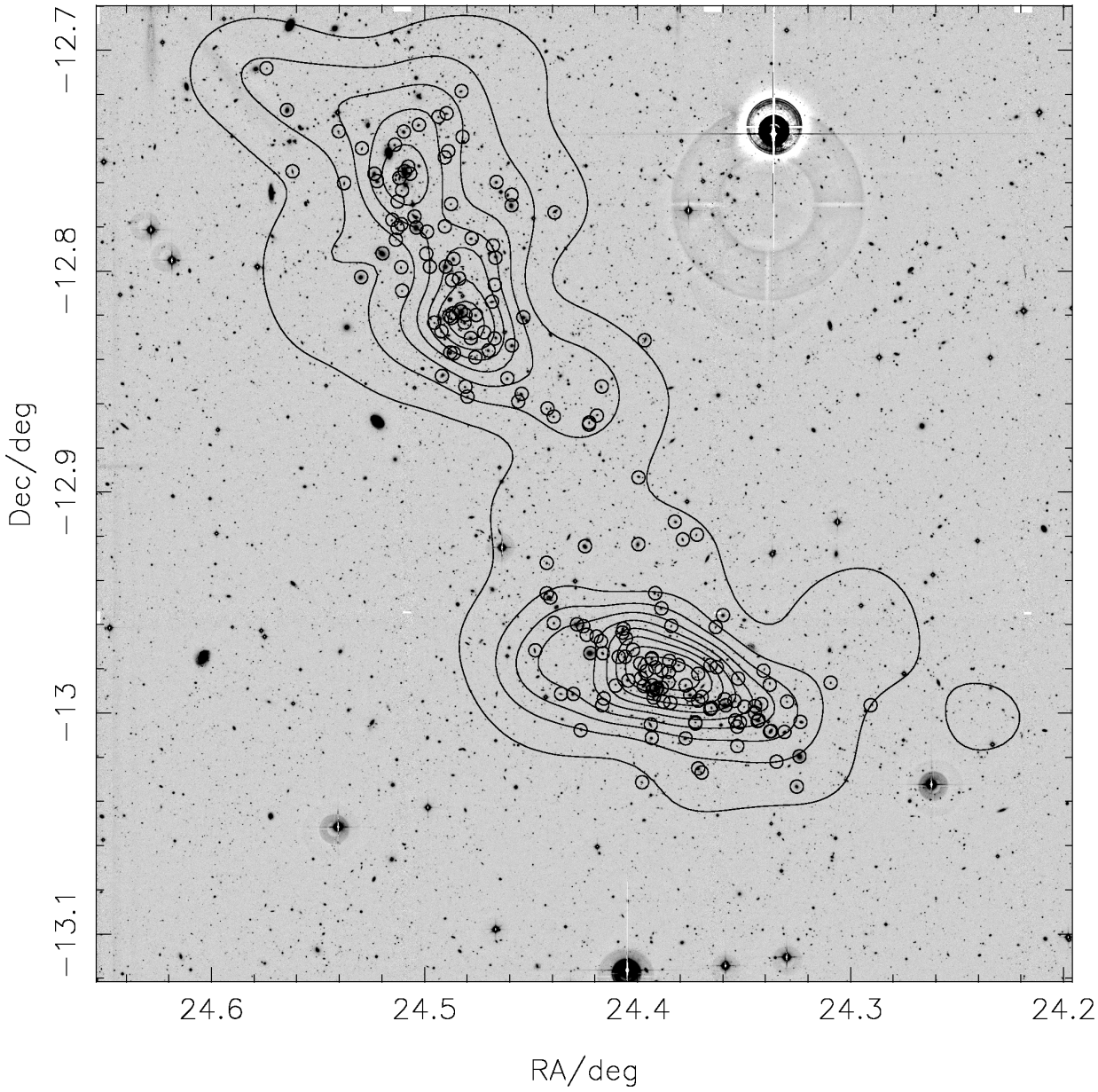

Figure 4.8: Deep R band image of A 222 and A 223. The galaxy density contours are generated from a color selected sample of 693 objects. See text for details. The small circles mark all spectroscopically identified cluster galaxies.

locities while keeping the observed galaxy positions fixed. The significance of the observed $\Delta_{\rm obs}$ is assessed by the fraction of simulations whose $\Delta_{\rm sim}$ is smaller than $\Delta_{\rm obs}$.

We find that, while the DS test is clearly able to separate both clusters at better than the 99.9% confidence level, it does not find any substructure in the individual clusters for values of $8 < n < 16$.

Also the DIP statistic (Hartigan & Hartigan 1985), which we calculated with the FORTRAN routine provided by Hartigan (1985), is not able to reject the null hypothesis of an unimodal distribution for any of the cluster samples. We tested for deviations from a normal Gaussian distribution by computing the skewness and kurtosis of both cluster samples. We found that we cannot reject a Gaussian parent population for both cluster samples at the 1σ level.

The wedge velocity diagrams in Fig. 4.9 clearly show the Abell system at $z \sim 0.21$. A small group of five galaxies can be seen behind A 223 at $z = 0.242$. We derive a velocity dispersion of $\sigma = 330$ km s^{-1}, confirming that it is not only close in the projected spatial distribution but also in redshift space.

4.4 Mass–to–light Ratio

To determine the luminosity of the clusters we applied the same cut on CLASS_STAR and color as above in a circle with 1.4 h_{70}^{-1} Mpc radius around the bright cD galaxy of A 222 and the center of the line connecting both density peaks in A 223.

The Schechter (1976) luminosity function,

$$n(L)\mathrm{d}L = n^*(L/L^*)^\alpha \exp(-L/L^*)\mathrm{d}(L/L^*) \ , \tag{4.5}$$

where L^* is the characteristic luminosity, α is the faint–end slope, and n^* is a normalization constant, gives the number of galaxies in the interval L to $L + \mathrm{d}L$. Written in terms of absolute magnitude eq. (4.5) becomes

$$\begin{aligned} N(M)\mathrm{d}M = kn^* \exp\{&[-k(\alpha+1)(M-M^*)] \\ &- \exp[-k(M-M^*)]\}\ \mathrm{d}M, \end{aligned} \tag{4.6}$$

where M^* is the absolute magnitude corresponding to L^* and $k = \ln 10/2.5$ (Kashikawa et al. 1995). For the Abell system $M_R = m_R - 5\log\left(\frac{d_{\rm l}}{\rm Mpc}\right) - 24.91$, $d_{\rm l}$ being the luminosity distance.

The fit of the luminosity function with parameters M^*, α, and n^* to the magnitude distribution of the selected objects is performed by binning the selected objects in bins of $\mathrm{d}M = 0.5$ mag and minimizing the quantity

$$\chi^2 = \sum \frac{[N(M_i) - N_f(M_i)]^2}{\sigma_i^2} \ , \tag{4.7}$$

with $N(M_i)$ and $N_f(M_i)$ being the observed and fitted number of galaxies in the ith magnitude bin. The variance of galaxies in each magnitude bin was assumed to be that of a Poissonian distribution.

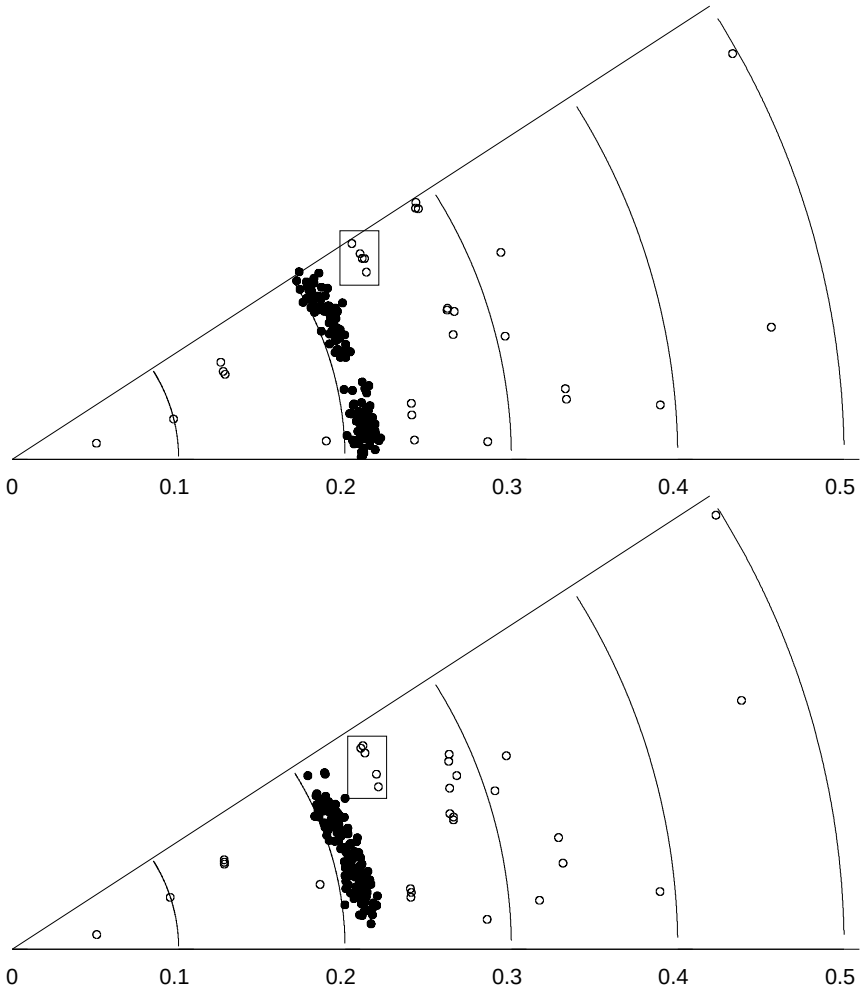

Figure 4.9: Declination (top) and right ascension (bottom) wedge redshift diagram. Cluster members a plotted as solid circles while background and foreground galaxies are displayed with open symbols. The rectangle highlights a small background group of galaxies. The opening angle is from $-13°2'24''$ to $-12°16'24''$ for the declination wedge and from 01:37:04.8 to 01:38:48.0 for the right ascension wedge.

The best–fit Schechter function for A 222 has $M^* = -22.1 \pm 0.2$, $\alpha = -1.04 \pm 0.12$, and $n^* = 31 \pm 11$. The χ^2 value for these parameters is 12.7 with 7 degrees of freedom. The best–fit parameters for A 223 are $M^* = -23.1 \pm 0.2$, $\alpha = -1.20 \pm 0.06$, and $n^* = 15 \pm 5$ with a minimum χ^2 value of 7.0, also for 7 degrees of freedom. From Figs. 4.10 and 4.11 we see, that the Schechter function is a good representation of the faint end, while it slightly underpredicts the number of bright galaxies.

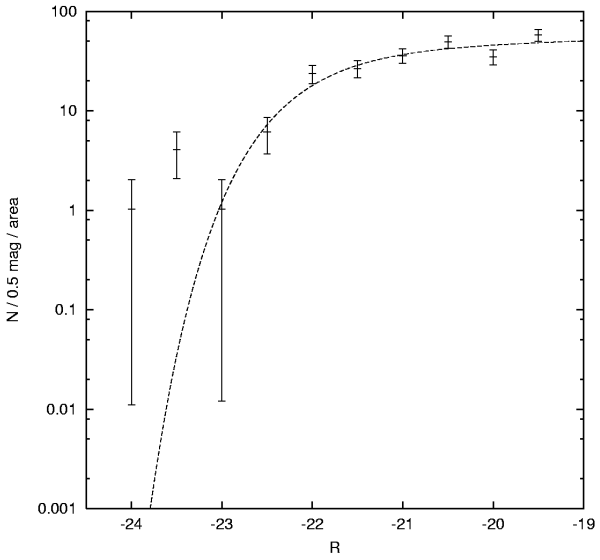

Figure 4.10: Differential R–band luminosity function for A 222. The points represent the objects selected by the criteria detailed in the text, while the dotted line is the best–fit Schechter function.

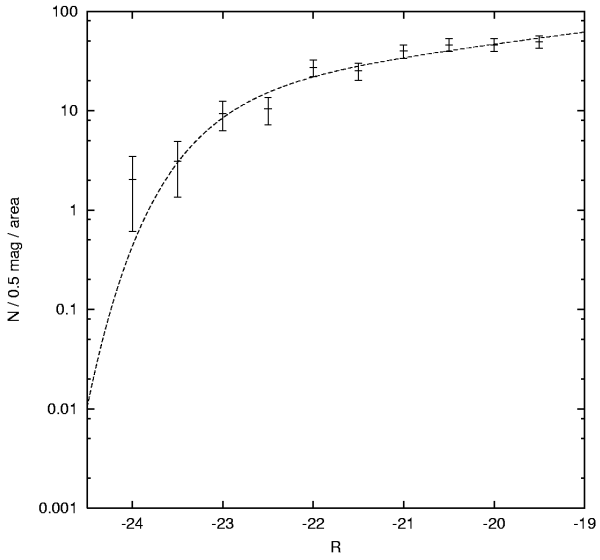

Figure 4.11: Same as Fig. 4.10 for A 223.

The total R–band luminosity of the red cluster sequence is determined by extrapolating the luminosity function. The observed fraction of the total luminosity is given by $\Gamma(\alpha + 2, L_{\rm lim}/L^*)/\Gamma(\alpha + 2)$, where $\Gamma(\cdot, \cdot)$ is the incomplete Gamma function, $L_{\rm lim}$ is the completeness limit, which in this case is given by the selection parameters, and L^* is the luminosity corresponding to the fitted M^* (Tustin et al. 2001). It follows from the chosen magnitude cut and the size of the bins, that in our case the limiting magnitude is $M_R = -19.0$. This implies that we observe 91.4% and 81.7% of the total light in A 222 and A 223, respectively. The total R–band luminosity of the red cluster sequence then is $L_R = (3.1 \pm 0.3) \times 10^{12}\ h_{70}^{-2}\ L_\odot$ for A 222 and $L_R = (4.4 \pm 0.4) \times 10^{12}\ h_{70}^{-2}\ L_\odot$ for A 223, where the errors reflect the uncertainty in the parameters of the luminosity function.

We compute mass–to–light ratios assuming an isothermal sphere model for both clusters with the velocity dispersion determined in section 4.3. The mass of an isothermal sphere

inside a radius r is given by

$$M(< r) = \frac{\pi \sigma_v^2}{G} r \ . \tag{4.8}$$

We get the following mass–to–light ratios for the red–cluster sequence inside a 1.4 h_{70}^{-1} Mpc radius:

$$\begin{aligned} \text{A 222}: \ (M/L)_R &= (343 \pm 60)\ h_{70}\ M_\odot/L_\odot \ , \\ \text{A 223}: \ (M/L)_R &= (253 \pm 47)\ h_{70}\ M_\odot/L_\odot \ . \end{aligned}$$

By selecting only the red cluster sequence we miss a significant part of the cluster luminosity. Folkes et al. (1999) found a ratio between the luminosity of their "type 1" galaxies (E/S0) and the total luminosity of 0.59 ± 0.07 in the fields of the 2dF survey. Using this correction factor we arrive at the final result:

$$\begin{aligned} \text{A 222}: \ (M/L)_R &= (202 \pm 43)\ h_{70}\ M_\odot/L_\odot \ , \\ \text{A 223}: \ (M/L)_R &= (149 \pm 33)\ h_{70}\ M_\odot/L_\odot \ . \end{aligned}$$

These values reported here slightly overestimate the true mass–to–light ratio because the use of isophotal magnitudes cuts off part of the galaxy luminosity and the intracluster light.

If we use the velocity dispersion derived from X–ray measurement instead of the spectroscopically determined velocity dispersion we arrive at mass–to–light ratios that are lower by $\sim 20\%$ but still agree within the 1σ error with the values quoted above.

Dressler (1978) gave a range of $140 - 420\ h_{70}\ M_\odot/L_\odot$ in a study of 12 rich clusters. Typical values for virial mass–to–light ratios are somewhat lower at values of $(M/L) \sim 210\ h_{70}\ M_\odot/L_\odot$ (Carlberg et al. 1996). Values of (M/L) ratios derived from X–ray masses tend to be somewhat lower than those from virial masses. Hradecky et al. (2000) find a median value of $(M/L)_V \sim 140\ h_{70}\ M_\odot/L_\odot$ in a study of eight nearby clusters and groups.

We cannot exclude the possibility that the values we report here are biased towards higher values by using an isothermal sphere model. Both cluster geometries clearly deviate from circular symmetric profiles. More robust mass estimates may thus lead to lower (M/L) ratios.

Chapter 5

Gravitational Lensing Study of Abell 222 and Abell 223

In this chapter I present preliminary results from the weak lensing analysis of the WFI data described in section 4.2.4. Again I assume a $\Omega_\Lambda = 0.7,\ \Omega_\mathrm{m} = 0.3,\ H_0 = 70\,h_{70}$ km s^{-1} Mpc^{-1} cosmology. The mean redshift of the FBG is assumed to be $\overline{z}_\mathrm{FBG} = 1$.

5.1 Catalog Production

The catalogs for the weak lensing analysis were produced from the images described in section 4.2.4. As in chapter 4, objects were detected using SExtractor (Bertin & Arnouts 1996); for the weak lensing analysis the deep R–band image was used. A list of candidate objects was made consisting of objects which had at least 3 contiguous pixels with fluxes above the signal–to–noise of the sky. The SExtractor catalog was used as input for Nick Kaiser's `IMCAT` software. Objects in the catalog were convolved with Gaussians of increasing FWHM to determine the smoothing radius r_g at which objects had a maximal signal–to–noise against the sky. New positions of the centers of all objects were computed as the point where the first–order brightness moments with a Gaussian weight function with radius r_g vanished. At this position also a new smoothing radius and signal–to–noise were determined. This was repeated until the new object position did not move by more than a 1/20th of pixel from the previous one, or the object was deleted from the catalog if its position deviated by more than 1 pixel from the original SExtractor value or its signal–to–noise fell below 5.

The second–order brightness moments Q_{ij}, eq. (2.38), were calculated with a Gaussian weight function of radius r_g and converted to ellipticities according to eq. (2.39). In addition to Q_{ij}, the flux and and the fourth–order brightness moments were measured on all surviving objects to compute the shear and smear polarizability tensors of Kaiser et al. (1995, hereafter KSB, corrections in Hoekstra et al. 1998), which define how the object reacts to an applied shear or convolution with a small anisotropic kernel. The corrections of KSB were applied as described in Clowe & Schneider (2001) to obtain the reduced shear

g. A radius r_h containing 50% of the flux of an object was also computed.

Objects with an ellipticity larger than 1, $R \leq 21$, $r_g \geq 1''.2$, $r_g \leq 0''.34$, or SExtractor CLASS_STAR ≥ 0.8 were removed from the catalog, as well as all objects that had neighbors closer than $2''$, or were not detected in the V band image. Stars were identified and removed in a plot of r_h versus isophotal R magnitude.

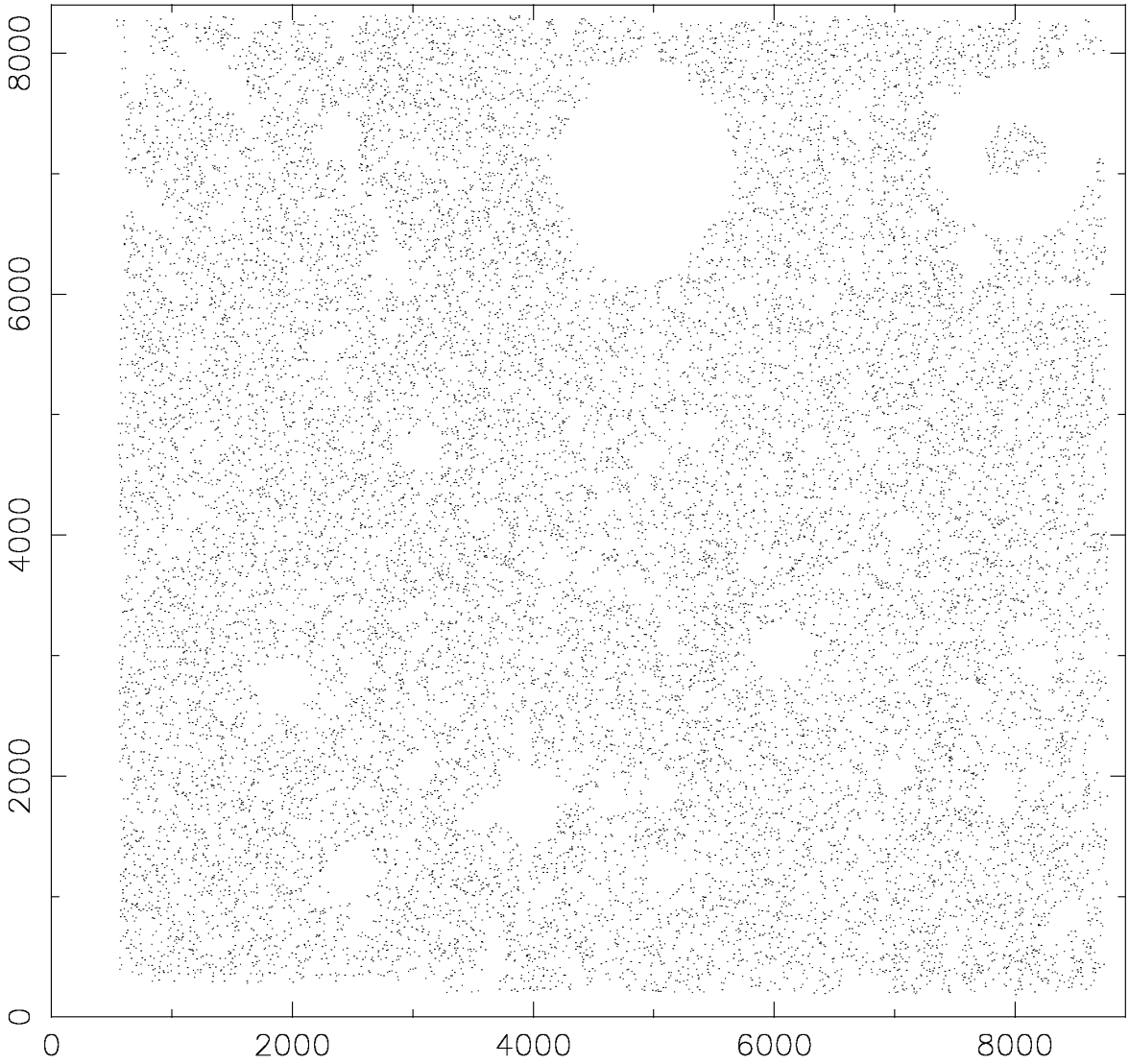

Figure 5.1: Object distribution in the final catalog. The scale of the axes is in pixels.

Stellar reflection rings are a prominent "feature" of the WFI and occur around every saturated star with blooming in the core. All objects lying in reflection rings were cut out by hand. Finally, the catalog was verified by visual inspection. The resulting catalog has 20.3 galaxies/arcmin^2. The distribution of objects on the field is shown in Fig. 5.1. The regions without objects on the left and the bottom are due to an offset between the V and

R band images.

After production of the catalog it turned out that using a Gaussian filter to convolve the objects, instead of the Mexican–hat filter used in Clowe & Schneider (2001), lead to r_g values that are too large. As a consequence the computation of the ellipticities and shear and smear tensors weighs regions away from the object center too much. These regions contain more noise and thus also the reduced shear has more noise than necessary.

5.2 Mass Reconstruction of the Abell 222/223 System

Figure 5.2 shows a reconstruction obtained from the catalog described in the previous section with an additional cut, that selected only objects with CLASS_STAR < 0.1. The number density of this catalog is $15.5/\mathrm{arcmin}^2$. The reconstruction was done on a 207×200 points grid with the algorithm of SAS described in section 2.3.1. The smoothing scale was set to $2\farcm5$. The mass–sheet degeneracy was fixed by setting the average κ of the left edge and bottom of the field to zero to avoid regions which have true mass concentrations extending beyond the edges of the field. This is especially important for the upper edge of the field where Abell 223 is cut off by the field boundary.

Both clusters, as well as a possible filamentary connection between them, are well visible in the reconstruction. Although the galaxy number density contours and the mass reconstruction show a filamentary connection between the clusters, they are not in good agreement in the intercluster region. The overdensity of color–selected objects approximately coincides with the region in which we obtained spectroscopy, while the filament in the mass reconstruction lies more to the east. This does not necessarily mean that the light does not follow the dark matter distribution, if we assume that the observed filamentary structures between both clusters indeed constitute a filament. We have to keep in mind that the color selection was done to select the E/S0 galaxies that constitute the red–cluster sequence. There is no a priori argument why a red–cluster sequence should be present outside the clusters in a possible filament. In fact, we expect early–type galaxies to be concentrated towards the cluster centers. The discrepancy in the filament shape may thus be due to the selection of an unsuitable tracer population in the color cut. On the other hand, there is no obvious argument why E/S0 galaxies in a filament should have different photometric properties than those in the clusters at the same redshift.

It is interesting to note that a reconstruction method designed to avoid edge effects, shows clear mass concentrations in three of the four corners of the field. In fact, the surface mass density in the corners in the SAS reconstruction is higher than that obtained from a KS93 reconstruction of the same field. While this may seem surprising at first, one has to keep in mind that SAS and KS93 have completely different properties at the edges, although in this case they show similar behavior. KS93 on the one hand invents shear data outside the observed field. The consequence is a systematic overestimation of the surface mass density at the edges, and especially in the corners. The noise level in the corners is low, due to the invented error–free data. SAS on the other hand does not use non–existent data from outside the observed field. The consequence is that no systematic

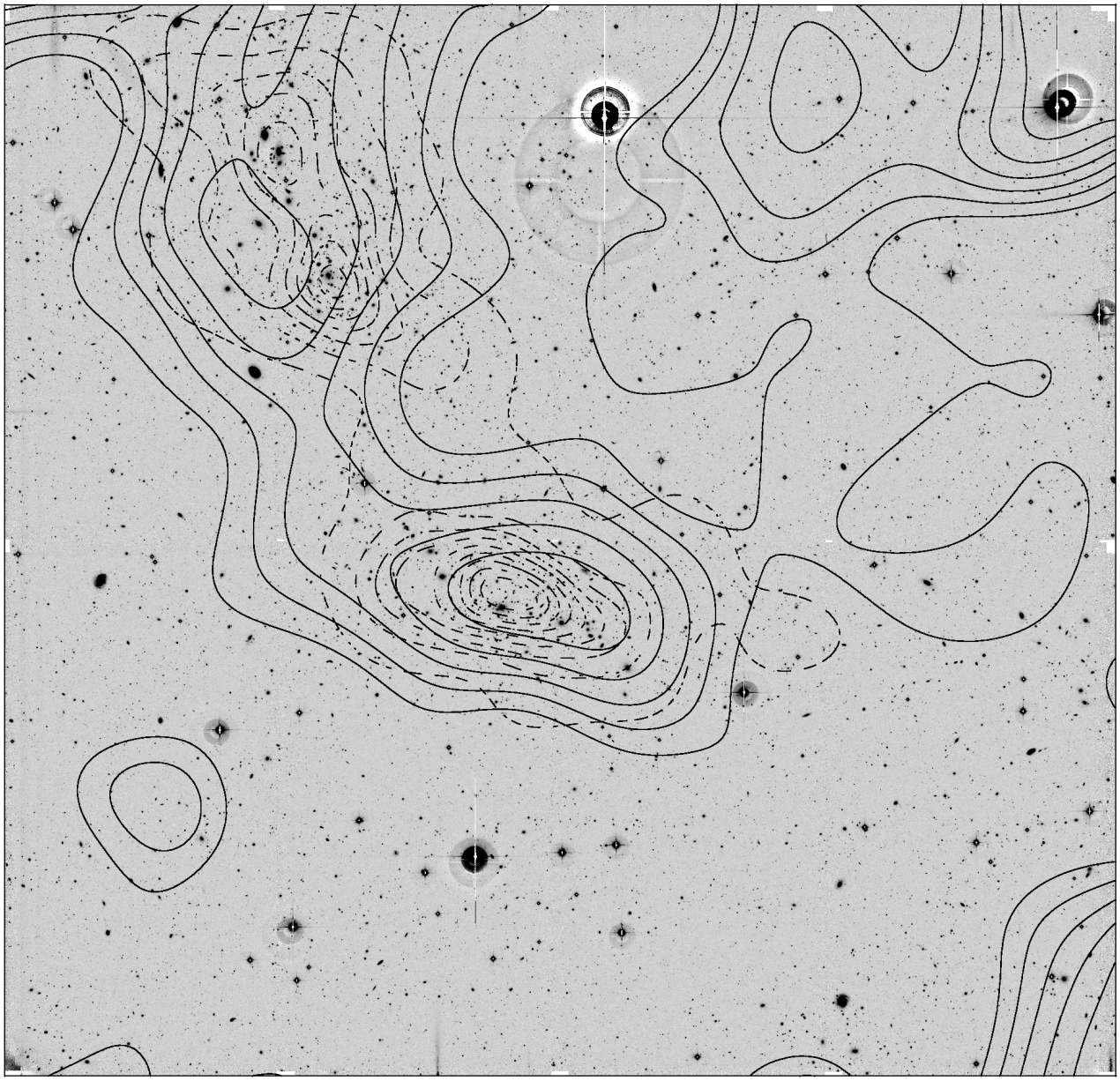

Figure 5.2: Above is a $34\farcm5 \times 33\farcm2$ deep R–band image of A 222/223 overlayed with the contours of a weak lensing mass reconstruction (solid lines) and the red–cluster sequence galaxy number density of Fig. 4.8 (dashed lines). The surface mass density contours rise in steps of 0.01 ($\sim 3.2 \times 10^{13}\ h_{70}\ M_{\odot}\ \mathrm{Mpc}^{-2}$, assuming $\overline{z}_{\mathrm{FBG}} = 1$) above the mean of the left and bottom edge of the field.

deviation in the corners is present, but the noise increases as the number of FBG in the corners decrease. Thus we can suspect that the reconstructed surface mass density in the corners is due to a few very deviant objects and not significant. This assumption will receive more support in the discussion of the aperture mass statistics on this field in the following section. Also, one should notice that the mass density in the upper left corner is dominated by A 223 and that due to a reflection ring the number density of objects in the upper right corner is too low to yield reasonable results.

The small mass peak to the ESE of A 222 corresponds to an overdensity of color selected objects with $0.8 < V - R < 1.0$ and $R < 21$. Assuming a redshift of $z \simeq 0.3$ for this galaxy concentration and using the shear between 50 and 1250 pixels ($53 - 1335\ h_{70}^{-1}$ kpc) distance from the center of the mass peak, the best fit SIS model has a velocity dispersion of $\sigma = 446^{+84}_{-109}$ km s^{-1} and a significance of 2.3σ.

The clusters themselves cannot be well fit with an SIS. This is probably due to their deviation from a circular geometry and their small projected separation, as well as the influence of the observed filamentary structure, which makes it difficult to find a reasonable outer limit for the fit.

I give lower bounds for the masses of the Abell clusters computed from the tangential component of the shear with respect to the cluster center using Kaiser's ζ statistics (Kaiser 1995, see section 2.4).

For Abell 222 the mean κ in a circle of 1.4 h_{70}^{-1} Mpc centered on the brightest cluster galaxy (BCG) minus the mean κ in a ring between 1690 h_{70}^{-1} kpc and 1850 h_{70}^{-1} kpc centered on the BCG is $\overline{\kappa} = 0.03 \pm 0.01$. This corresponds to a lower bound of $(5.7 \pm 2.0) \times 10^{14}\ M_\odot$ for the mass of A 222 in that radius. Using the total luminosity within the same radius determined in section 4.4, we get a mass–to–light ratio of $(M/L)_R \sim 110\ h_{70}\ M_\odot/L_\odot$.

The same for A 223 in a circle centered between the density peaks of the galaxy cluster yields $\overline{\kappa} = 0.02 \pm 0.01$, corresponding to a lower mass limit of $(4.1 \pm 2.0) \times 10^{14}\ M_\odot$ and a mass–to–light ratio of $(M/L)_R \sim 56\ h_{70}\ M_\odot/L_\odot$. Clearly, the values for the mass–to–light ratios are too low and can only serve as lower limits for the actual values.

5.3 Aperture Mass Maps of the Abell 222/223 Clusters

To asses the significance of various structures seen in the reconstruction of the previous section, I calculated the $M_{\rm ap}$ statistics for different filter scales. Eq. (2.77) with $l = 1$ was used as weighting function, the filter scale was increased from 0.′8 to 9.′6 in steps of 0.′8. The signal–to–noise ratio was computed from 1000 randomizations of the catalog objects. Figures 5.3 to 5.6 show four $M_{\rm ap}$–maps overlayed with the contours of the signal–to–noise ratio on the same field as in Fig. 5.2, for which interesting structures have maximal signal–to–noise. The differences in the various $M_{\rm ap}$–maps are also a nice illustration of the bandpass nature of the aperture mass statistics.

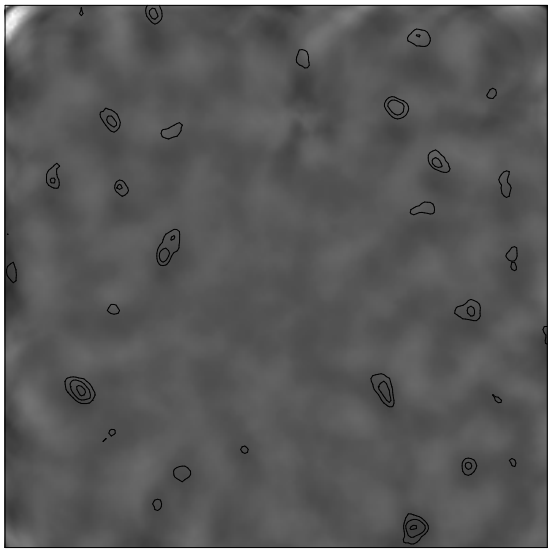

Figure 5.3: Grayscale image of the $M_{\rm ap}$ statistics in a 3.′2 filter radius overlayed with signal–to–noise contours rising from 2.0 in steps of 0.5.

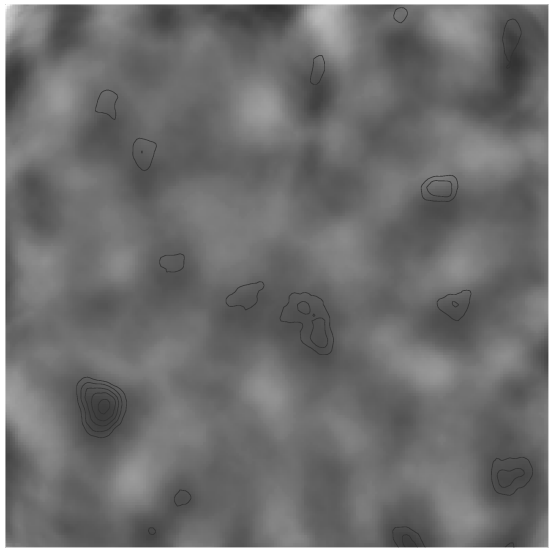

Figure 5.4: Same as Fig. 5.3 with a 4.′8 filter radius.

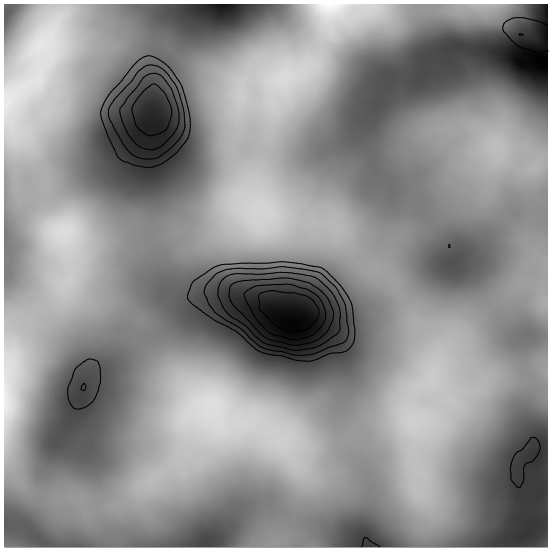

Figure 5.5: Same as Fig. 5.3 with a 8.′8 filter radius.

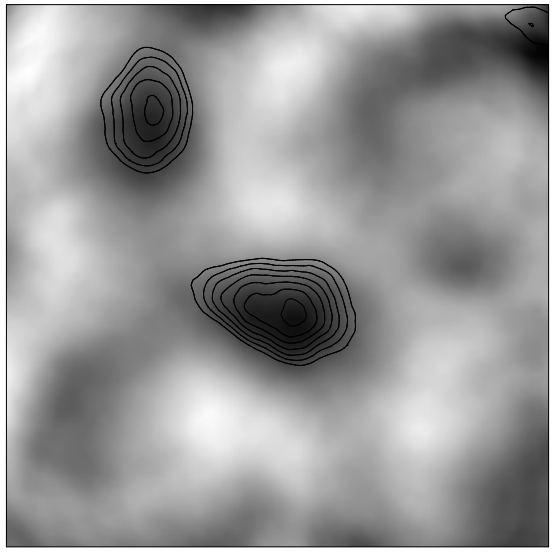

Figure 5.6: Same as Fig. 5.3 in a 9.′6 filter radius.

Although mostly dominated by noise, Fig. 5.3 displays the $M_{\rm ap}$–map for which the filament region has the highest signal–to–noise. The signal–to–noise is 3.0 in the center of the peak on the filament candidate.

Fig. 5.4, generated with a filter scale of $4\farcm8$, has the highest signal–to–noise ratio for the small mass clump to the SE of A 222. Its signal–to–noise ratio is 4.2.

On larger scales the big clusters in the field become dominant. A 222 has a signal–to–noise in the aperture mass statistics that reaches a maximum of 5.3 for a filter radius of $8\farcm8$, while the extended cluster A 223 without a clear central peak attains its maximal signal–to–noise in the largest computed filter scale of $9\farcm6$ with a value of 4.2.

Similar to the reconstruction in Fig. 5.2, the $M_{\rm ap}$ statistics show higher values in the corners of the field on larger scales. However, the randomizations show that these, with a possible exception in the upper right corner, are not significant. This supports the hypothesis that the rising κ values in the corner are due to a few deviant galaxies.

The additional cut on CLASS_STAR made in the previous section has two consequences:

1. The reconstructed κ and the $M_{\rm ap}$ statistics have higher values.

2. The noise also increases.

This is due to the removal of many circular or almost circular objects. These objects decreased the shear signal but also did not contribute to variation of the shear if their orientation was randomized. Also, the signal–to–noise is proportional to the inverse of the number density. It is also likely that we introduced a small bias to higher masses by deleting (almost) circular objects that were not stars.

5.4 Quadrupole Statistics in the Abell 222/223 System

The only method of quantifying a filament tested in chapter 3 that gave some reasons for optimism regarding its applicability to real data was the quadrupole moment statistics. Even if fitting ellipses to clusters had been successful in the simulations, the noisy region around A 223 would make any such fit on this field impossible. Thus, I try to apply the quadrupole statistics to the Abell system.

Figure 5.7 shows a map of the quadrupole moment $|Q^{(2)}|$ and its signal–to–noise contours from 1000 randomizations of the orientation of the catalog objects. The quadrupole moment was calculated inside an aperture with $3\farcm2$ radius, i.e. the radius for which the filament region in the $M_{\rm ap}$ statistics attained its highest signal to noise. Similar to the $M_{\rm ap}$ statistics the $|Q^{(2)}|$–map is dominated by noise on this scale. The small peak in the filament region with a significance of $\sim 2.7\sigma$ is in the center of an aperture that already begins to overlap the southern tip of A 223. Right between the clusters, where the simulation exhibited the strongest quadrupole signal, no significant quadrupole moment is found.

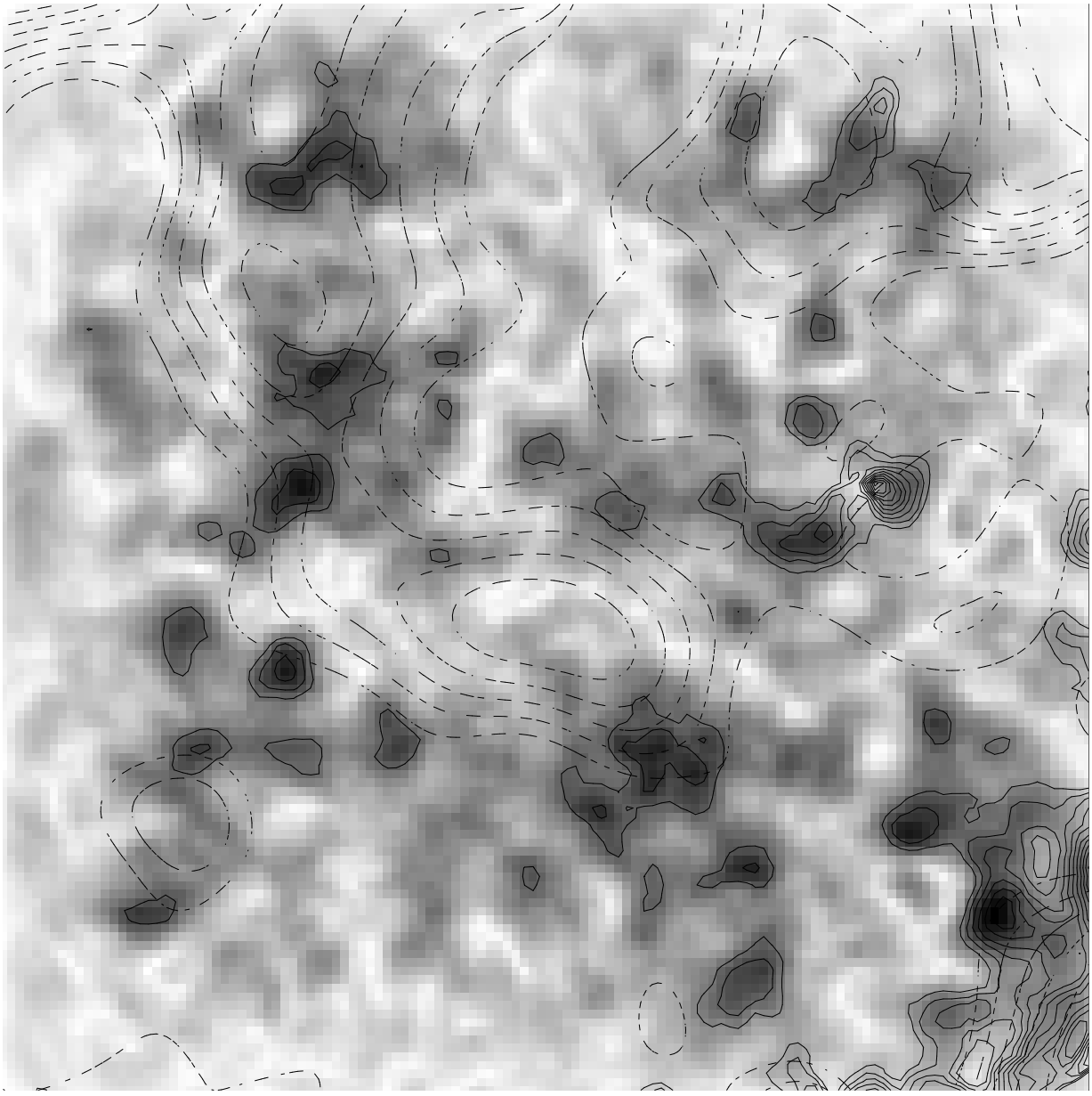

Figure 5.7: $|Q^{(2)}|$ map with a filter radius of 3′.2 of the Abell system. Overlayed are the signal–to–noise contours (solid lines) from 1000 randomizations rising in steps of 0.5 from 2.0 and the mass reconstruction (dashed lines).

5.5 Strong Lensing Features in Abell 222

Already in 1991 Smail et al. (1991, hereafter SEF) found two candidate arclets in the center of A 222. We also see two possible arclets in the center of A 222 displayed in Fig. 5.8. Arclet 1 is the same as found by SEF and labeled A222–1. Unfortunately, SEF's second candidate is not marked on the plate in their paper, and as SEF give only distances from the cluster center and no position angle we do not know whether their second candidate corresponds to ours. A comparison of the arclet candidate properties between SEF and our candidates is given in table 5.1. The distance measurements for A 222–1 and arclet 1 are

Table 5.1: Arclet candidate properties from SEF and our data. The column entries are distance from the center of the cD galaxy, axis ratio, and position angle measured clockwise from the north direction in Fig. 5.8.

Arc ID	d/arcsec	A	pos. angle
SEF			
A 222–1	12.2	4.7	-
A 222–2	14.1	2.6	-
this work			
arclet 1	12.7	2.8	42°
arclet 2	10.8	3.0	140°

in good agreement but the values for the axis ratio show a clear deviation. The difference may be due to the comparably poor image quality in the work of SEF and blending with the nearby object to the South–West of arclet 1. However, it must also be mentioned that the determination of the axial ratio is relatively uncertain and I estimate its error from repeated measurements to be of the order $\simeq 0.6$.

Given the discrepancy between the distance measurements for A 222–2 and arclet 2 it is unlikely that these are the same objects.

Unfortunately, the V band image is not deep enough to show the candidate arclets, so that no color information is available.

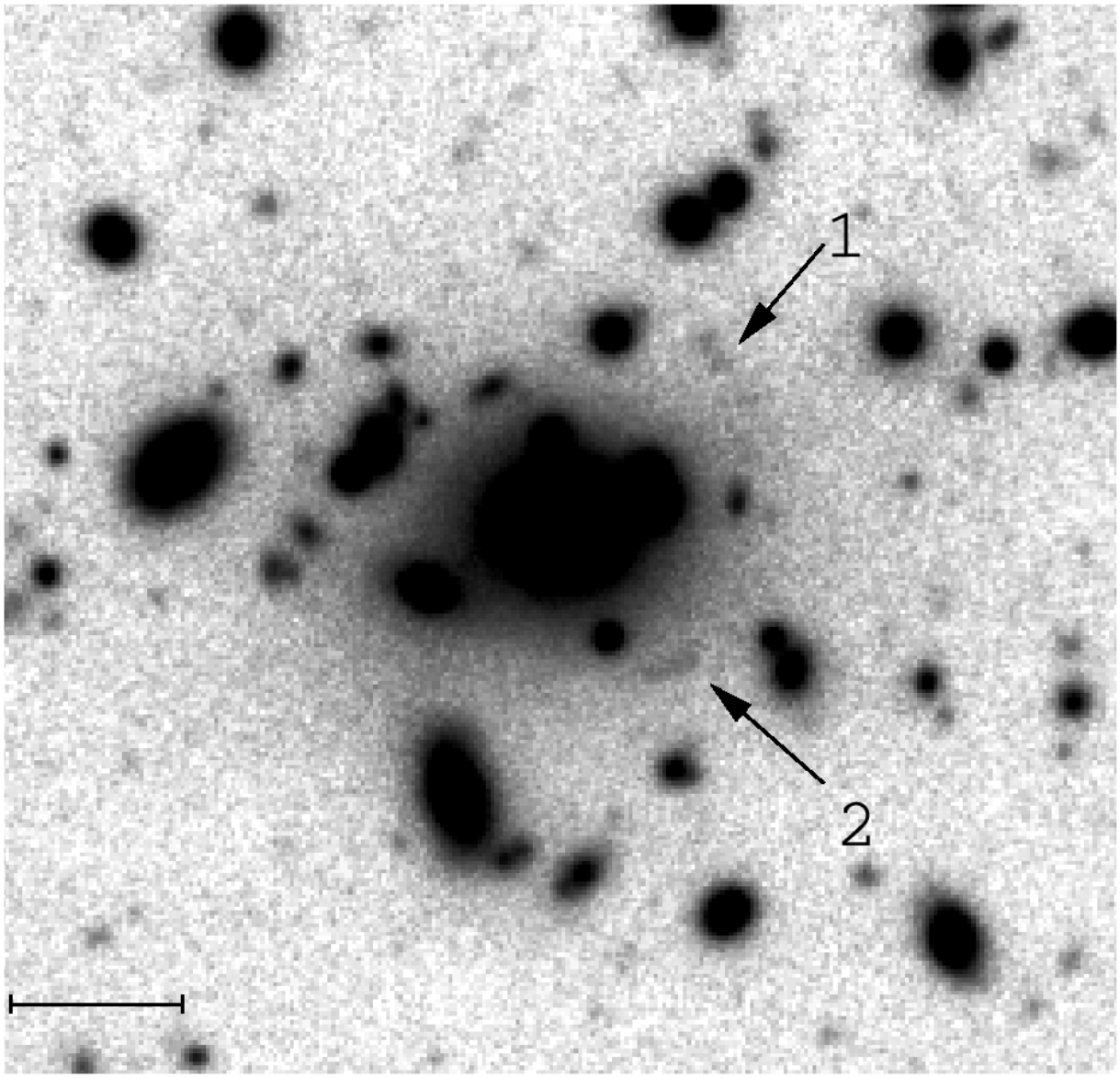

Figure 5.8: Arclet candidates around the cD galaxy in A 222. North is up and East is to the left. The scale is 10″ long.

Chapter 6

Discussion and Outlook

In this work I investigated how to quantify the presence of a filamentary structure between close pairs of galaxy clusters. I used the results of n–body simulations in an attempt to develop a statistics that allows one to assess the significance of a possible filament detection. This turned out to be a much more challenging task than anticipated. First, it was very difficult for Emilio Romano–Díaz to produce simulations that had strong enough filaments. The two results of simulations displayed in chapter 3 are the ones with the strongest filaments out of a total of eight simulations whose results Emilio gave me. I do not know how many other simulations he just threw away. Second, it was amazing to see how numerical methods failed to reproduce what is obvious upon visual inspection of the simulated data. Even for mass distributions that were known beforehand, it was not possible to fit elliptical profiles to the clusters. Parameters like the orientation of the major cluster axis, which are almost immediately obvious to the observer, could not even approximately be yielded from any fitting procedure (sections 3.3.1 to 3.3.3). The attempt to find an objective criterion to separate cluster and filament region failed even in the case of the simulation with the strongest filament (section 3.4.1).

Consequently, the possibility to apply any of the methods of chapter 3 to the available observations of A 222/223 was very limited. The $|Q^{(2)}|$–map on the Abell field does not show a significant quadrupole moment centered on the possible filament seen in the weak lensing reconstruction. In fact, the quadrupole moment is in some regions of the filament candidate as low as in the center of A 222. There are a couple of arguments speaking for and against a filament extending between Abell 222 and Abell 223.

Arguments hinting at a mass bridge between the clusters are: The filament is seen not only in the mass reconstruction but also in the $M_{\rm ap}$–maps on many filter scales. The $M_{\rm ap}$ statistics gives only a low significance level for the filament, but that is to be expected. A circular aperture is clearly not ideal to detect something as non–circular as a filament. Depending on the filter scale, either parts of the filament or parts of the more massive clusters lie in the negative portion of the weighting function. Also in favor of a bridge between both clusters is the fact that we observe a connection in color–selected objects.

However, as noted in the previous chapter, the bridge in the light distribution and the bridge in the mass reconstruction are not aligned. While possible arguments to explain this

were already discussed in section 5.2, this raises some doubt. Although one does not expect a high significance of the $M_{\rm ap}$ statistics on a filament for reasons detailed in the previous paragraph, the maximum significance of the filament candidate does not exceed that of noise peaks at the same filter scale. The strongest argument against a filament between A 222 and A 223 is probably the absence of a quadrupole moment on the filament.

Much of the discussion in chapter 3 was devoted to answering the question "What is a filament?". Assuming that the mass bridge between the Abell clusters is not a noise artifact, should we call this a filament? The possible filament extends to the North from the Eastern tip of A 222, whose major axis is oriented along the East–West direction. This is not a symmetric situation like in Fig. 3.14, so that we probably can exclude the possibility of overlapping clusters. Unless further observations show that A 223 extends as far to the North as the candidate filament extends to the South from the center of A 223, this structure – if real – should be called a filament.

Spectroscopic observations were carried out to identify galaxies between the clusters at the cluster redshift. Unfortunately, the spectra were observed along a line connecting the centers of both clusters. As a consequence spectroscopic data is only available at the western edge of the color–selected filament candidate. Indeed, we found a couple of galaxies at the cluster redshift in that region. No data is available in the central part of the color–selected bridge or in the filament candidate from the weak lensing reconstruction.

Currently there is not enough data available to make a definite decision whether a filament extends between both clusters or not. Certainly the A 222/223 system is an interesting candidate for detecting such a filamentary structure and deserves a more detailed analysis.

New WFI data centered on A 223 was observed in the past observing period but has not yet been made available to us. This data should increase the signal–to–noise not only in A 223 but also in other regions, including the intercluster region, on the field. Also, convolving the objects with the usual Mexican–hat filter instead of a Gaussian should give significantly better signal–to–noise, so that hopefully we will be able to decide whether a filament connects A 222 and A 223 in the not too distant future.

Although the weak lensing data is noisy, both clusters are significantly detected in the reconstruction. Mass determinations of the clusters have been difficult due to the noise in the data and the geometry of the clusters, so that I only gave lower limits for the cluster masses in chapter 5. In addition, a mass peak SE of A 222 was discovered at the 4.2σ significance level with the $M_{\rm ap}$ statistics.

Finally, a few differences between the results of the simulations used in this thesis and the observed filament candidates must be pointed out. The simulation always had a straight filament between the clusters. This is not necessarily the case as other simulations (Bond et al. 1996), the "banana" shape of the Abell system, and the possible filament detected by Gray et al. (2002) show. However, this is the simplest geometry and any method developed to identify filaments should at least work in the case of a straight filament. More important is the difference in density contrast $(\kappa_{\rm cluster} - \kappa_{\rm filament})/\kappa_{\rm filament}$ between the simulations and observed filament candidates measured in the center of the clusters and the filament. While the filament candidates of Kaiser et al. (1998), Gray et al. (2002), and this work all suggest

a density contrast of $1 - 2$, the density contrast in the reconstructions of the simulated data never fell below 5, if the same smoothing scale as for the observational data in chapter 5 was used. It remains to be investigated whether the simulations systematically predict filaments of too low surface mass density, or whether the observers reporting these possible filaments just have been lucky to find such massive filaments. I expect that the method of separating clusters and filaments of section 3.4.1 gives much better results, if the density contrast is indeed as low as observations suggest it.

Appendix A

Spectroscopic Catalog of Abell 222 and Abell 223

This appendix lists the full spectroscopic catalog of Abell 222 and Abell 223 as described in chapter 4. The column entries are:

1. Object No.
2. right ascension (hour:minute:second)
3. declination (degree:minute:second)
4. R band magnitude
5. $V - R$ color

6-9. observed equivalent widths of [O II], [O III], Hβ, and Hα as defined in eq. (4.1)

10 & 11 heliocentric redshift and error

12. R-value of Tonry & Davis (1979)

13. Notes, **p**: Proust et al. (2000), **n**: Newberry et al. (1988), **s**: Sandage et al. (1976), **em**, radial velocity derived from emission line template, **1**: measured on [O II], Hβ, Hα, **2**: 0.05126 ± 0.00013 from [O II], [O III], Hβ, **3**: 0.21759 ± 0.00017 from Hα Hα, **4**: 0.21605 ± 0.00026 from [O II], [O III], Hβ, Hα, [N II], **5**: 0.21788 ± 0.00009 from Hα, [N II], **6**: 0.20777 ± 0.00020 from [O II], [O III], Hβ, Hα, **7**: 0.20694 ± 0.00038 from [O II], [O III], Hβ, **8**: 0.13738 ± 0.00027 from [O II], [O III], Hβ, Hα, **9**: 0.20739 ± 0.00057 from [O II], Hβ, Hα, **10**: 0.20459 ± 0.00009 from [O III], [N II], **11**: 0.21281 ± 0.00015 from [O II], [O III], Hβ, Hα, **12**: 0.24231 ± 0.00041 from [O II], [O III], Hβ, Hα, **13**: 0.24178 ± 0.00025 from [O II], [O III], Hβ, Hα.

Object No.	RA (2000)	Dec (2000)	R	$V-R$	[O II]/Å	[O III]/Å	Hβ/Å	Hα/Å	$z_{\rm hel}$	$\sigma_{z_{\rm hel}}$	R	Notes
ABELL 222												
1	01:37:13.43	−13:01:07.6	19.26	0.60	4.3 ± 1.7	-	-17.6 ± 7.8	-	0.28598	0.00019	6.12	
2	01:37:13.56	−13:00:19.1	17.92	0.26					star			
3	01:37:14.46	−12:59:19.8	19.23	0.77	-	-	-4.4 ± 1.8	-	0.21616	0.00013	8.59	
									0.21681	0.00025		p
4	01:37:17.02	−12:59:31.4	20.92	0.89	15.9 ± 7.0	-	5.7 ± 2.0	-	0.39091	0.00036	2.99	
5	01:37:17.46	−13:03:16.0	19.16	1.03	1.2 ± 0.5	-	-4.6 ± 1.8	2.8 ± 1.3	0.31828	0.00019	5.63	
6	01:37:17.89	−13:00:55.8	18.85	1.22					star			
7	01:37:17.76	−13:00:24.3	18.43	0.63	-	-	-8.1 ± 1.2	9.0 ± 1.7	0.21749	0.00024	4.49	
8	01:37:17.97	−13:01:20.7	17.03	0.83	-	-	-7.5 ± 1.7	-	0.21132	0.00011	11.30	
9	01:37:18.29	−13:02:10.3	18.06	0.83	-	-	-3.2 ± 1.2	-	0.20977	0.00010	11.58	
10	01:37:19.37	−12:59:50.9	19.79	0.79	-	-	-	-	0.21263	0.00027	3.98	
11	01:37:19.67	−13:00:40.6	18.15	0.79	-	-	-7.9 ± 1.5	-	0.21518	0.00017	6.57	
									0.21676	0.00026		p
12	01:37:20.62	−13:01:29.5	19.30	0.59	2.7 ± 1.1	-	-	-	0.21821	0.00011	6.14	
13	01:37:21.21	−13:00:39.2	17.74	0.81	-	-	-5.9 ± 1.3	-	0.22067	0.00020	5.97	
14	01:37:21.49	−13:00:23.5	16.51	0.08					star			
15	01:37:22.31	−12:59:54.7	18.60	0.82	-	-	-	-	0.21879	0.00020	5.77	
16	01:37:22.65	−13:00:21.3	17.60	0.76	-	-	4.9 ± 1.4	-	0.21161	0.00019	6.13	
17	01:37:22.56	−12:58:36.1	19.16	0.63	11.4 ± 4.3	-	-11.4 ± 4.8	-	0.24162	0.00034	3.28	
18	01:37:23.01	−13:00:09.6	18.16	0.79	-	-	-3.9 ± 1.4	-	0.21398	0.00018	6.37	
19	01:37:23.05	−12:59:57.9	18.30	0.66	-	-	-8.6 ± 1.5	-	0.20167	0.00016	6.62	
20	01:37:24.18	−12:57:36.5	18.16	0.97	-	-	-5.3 ± 1.9	-2.6 ± 1.0	0.24223	0.00020	5.67	
21	01:37:24.20	−12:59:59.2	20.44	0.79	-	-	-	-	0.21175	0.00034	4.68	
22	01:37:24.3	−12:57:04.8	20.03	0.58					star			
23	01:37:24.69	−13:00:25.0	20.78	0.37	-	-	-	-	0.22176	0.00035	2.97	
24	01:37:24.86	−12:59:13.1	19.52	0.81	-	-	-	-	0.21455	0.00022	4.93	
25	01:37:24.98	−13:00:31.8	19.60	0.57	-	-	-	8.7 ± 2.4	0.20757	0.00019	4.72	

26	01:37:25.00	−13:01:03.7	20.62	0.69	-	-	-	-	0.21503	0.00020	5.06	
27	01:37:25.28	−12:59:49.4	19.02	0.62	-	-	-	5.3 ± 1.9	0.20958	0.00019	5.11	
28	01:37:25.46	−13:00:45.6	21.18	0.54	-	-	-	22.7 ± 6.2	0.24206	0.00041		1
29	01:37:26.07	−12:58:41.4	19.44	0.91	-	-	-5.9 ± 1.8	-	0.33507	0.00018	6.29	
30	01:37:26.34	−12:59:56.9	16.97	0.83	-	-	-7.0 ± 1.4	-	0.21347	0.00023	5.34	
									0.21356	0.00007		p
31	01:37:26.45	−12:59:47.0	19.19	0.85	-	-	-7.9 ± 1.9	-	0.21172	0.00021	5.39	
32	01:37:26.57	−12:57:28.9	18.02	1.04	-	-	-6.3 ± 1.6	-	0.21605	0.00020	6.19	
33	01:37:26.80	−13:00:28.9	16.69	-0.17					star			
34	01:37:27.31	−12:58:54.4	19.77	0.80	-	-	-	-	0.21138	0.00017	6.19	
35	01:37:27.39	−12:57:48.3	19.51	0.98	-	-	-5.8 ± 2.0	-	0.20609	0.00017	6.58	
36	01:37:27.73	−12:58:27.8	18.11	0.82					star			
37	01:37:27.86	−13:00:01.0	19.02	0.85	-	-	-6.5 ± 2.5	-	0.21489	0.00020	6.00	
38	01:37:28.04	−12:58:51.2	18.59	0.77	-	-	-3.2 ± 1.4	-	0.20993	0.00021	5.37	
39	01:37:28.32	−12:55:55.7	17.77	0.66	-	15.7 ± 0.5	9.3 ± 1.2	42.6 ± 0.7	0.05147	0.00023	4.35	2
40	01:37:28.51	−12:56:36.2	16.79	0.39					star			
41	01:37:29.02	−13:01:47.1	19.24	0.81	-	-	-9.5 ± 3.0	-	0.21134	0.00022	3.66	
42	01:37:29.03	−12:59:43.0	18.52	0.78	-	2.9 ± 0.8	-5.5 ± 1.9	-	0.21342	0.00023	5.20	
43	01:37:29.38	−13:01:40.5	18.08	0.86	-	-	-4.9 ± 1.6	-	0.20997	0.00020	5.39	
44	01:37:29.39	−12:59:04.9	19.74	0.82	-	-	-	-	0.21909	0.00020	5.86	
45	01:37:29.43	−12:59:49.1	19.08	0.77	-	-	-6.1 ± 1.7	-1.6 ± 0.4	0.21724	0.00017	6.52	
									0.21852	0.00035		p
46	01:37:29.55	−12:55:16.5	19.91	0.79	-	-	-6.3 ± 2.3	-	0.20379	0.00017	5.18	
47	01:37:29.66	−13:00:24.6	19.75	0.84	-	-	-	-	0.21101	0.00025	4.24	
48	01:37:30.14	−13:00:14.2	17.74	0.84					star			
49	01:37:30.27	−12:59:39.6	18.10	0.86	-	-	-7.4 ± 1.3	-1.9 ± 0.7	0.21405	0.00017	6.66	
50	01:37:30.77	−12:59:23.9	18.76	0.87	-	-	-8.1 ± 1.8	-	0.21632	0.00017	6.66	
									0.21635	0.00007		p
									0.21667	0.00008		p
									0.21631	0.00070		n

Object No.	RA (2000)	Dec (2000)	R	$V-R$	[O II]/Å	[O III]/Å	Hβ/Å	Hα/Å	$z_{\rm hel}$	$\sigma_{z_{\rm hel}}$	R	Notes
51	01:37:30.80	−13:00:51.2	18.10	0.82	-	-	-4.0 ± 1.5	-	0.20559	0.00026	4.86	
52	01:37:31.09	−12:55:24.4	18.74	0.86	-	-	-5.4 ± 2.4	-	0.21888	0.00020	5.74	
53	01:37:31.56	−12:58:50.7	18.97	0.83	-	-	-	-	0.21764	0.00017	6.58	
									0.21690	0.00011		p
54	01:37:31.89	−12:54:55.1	18.70	0.80	-	-	-6.9 ± 2.1	-1.3 ± 0.6	0.21539	0.00018	6.62	
55	01:37:32.38	−12:57:46.3	19.74	0.73	-	-	-5.2 ± 2.5	-	0.20465	0.00013	9.10	
56	01:37:32.46	−12:59:52.2	19.31	0.85	-	-	-6.4 ± 2.3	-	0.21234	0.00021	5.59	
57	01:37:32.73	−13:01:51.9	19.67	1.19					star			
58	01:37:32.47	−12:59:01.6	20.05	0.52	23.0 ± 5.8	5.5 ± 1.9	-	29.4 ± 2.0	0.21602	0.00032	2.24	
59	01:37:32.45	−13:02:31.5	19.63	1.21					star			
60	01:37:32.50	−12:58:02.3	19.72	0.80	12.6 ± 2.7	-	-4.3 ± 1.9	21.3 ± 2.7	0.33515	0.00024	4.18	
61	01:37:33.27	−13:00:23.9	18.82	0.81	-	-	-6.0 ± 1.6	-	0.18903	0.00021	4.81	
62	01:37:33.34	−12:59:50.7	19.63	0.90	-	-	-6.2 ± 2.4	-	0.21061	0.00024	4.67	
63	01:37:33.48	−12:58:59.2	19.58	0.78	-	-	-	-14.3 ± 3.6	0.21471	0.00020	5.02	
									0.21498	0.00009		p
64	01:37:33.52	−12:57:17.4	19.08	0.77	-	-	-	-	0.21741	0.00023	4.43	
65	01:37:34.01	−12:59:28.6	17.00	0.89	-	-	-7.7 ± 1.6	-	0.21329	0.00021	6.11	
									0.21387	0.00012		p
66	01:37:34.13	−13:01:52.4	18.18	0.91					star			
67	01:37:34.22	−12:58:54.3	20.69	0.62	-	1.5 ± 0.5	-	3.4 ± 1.0	0.21489	0.00020	6.00	3
68	01:37:34.24	−12:56:52.8	17.44	1.01					star			
69	01:37:34.2	−12:56:52.7	17.44	1.01	-	-	-6.8 ± 1.9	-	0.20809	0.00028	4.05	
70	01:37:34.41	−12:59:43.9	18.22	0.87	-	-	-8.1 ± 1.7	-	0.21878	0.00027	4.36	
									0.21980	0.00022		p
71	01:37:34.52	−12:59:32.1	18.94	0.86	-	-	-8.1 ± 1.5	-3.4 ± 1.1	0.21331	0.00022	4.71	
72	01:37:34.56	−12:58:39.6	18.54	0.83	-	-	-	-	0.20921	0.00018	6.13	
73	01:37:34.61	−13:00:50.4	18.68	0.47	-	-	-7.6 ± 1.7	-	0.20841	0.00031	3.12	
74	01:37:34.69	−13:02:23.9	16.94	1.07					star			

75	01:37:34.74	−13:00:28.2	18.10	0.83	-	-	-	-	0.20480	0.00020	5.56	
76	01:37:35.25	−12:59:00.6	19.39	0.90	3.3 ± 1.4	-	-7.6 ± 1.7	-	0.21179	0.00020	4.97	
77	01:37:35.51	−12:59:25.0	18.31	0.75	-	-	-8.6 ± 1.6	-	0.21022	0.00017	6.08	
78	01:37:35.69	−13:02:03.0	19.42	0.72	7.8 ± 3.2	-	-6.2 ± 2.1	-	0.21064	0.00021	4.67	
									0.21006	0.00015		p
									0.20931	0.00050		n
79	01:37:35.76	−12:59:12.0	19.65	0.87	-	-	-5.6 ± 2.7	-3.1 ± 1.4	0.21270	0.00022	5.49	
80	01:37:35.87	−12:58:47.9	19.74	0.87	-	-	-5.5 ± 2.0	-	0.21233	0.00027	4.00	
81	01:37:36.13	−12:55:32.2	18.04	0.71	-	-	-3.8 ± 1.3	-	0.20858	0.00014	7.28	
82	01:37:36.65	−12:58:25.6	19.43	0.84	-	-	-3.2 ± 1.5	-	0.21446	0.00016	6.68	
83	01:37:37.27	−12:59:15.0	18.87	0.43	18.9 ± 2.5	-	5.5 ± 1.9	19.9 ± 3.5	0.21514	0.00031	3.30	em
									0.21441	0.00020		n
84	01:37:37.53	−12:58:06.6	19.17	0.77	-	-	-	-	0.21010	0.00017	6.09	
85	01:37:37.62	−12:58:37.0	18.68	0.86	-	-	-10.2 ± 2.0	-	0.21629	0.00016	7.12	
86	01:37:37.82	−12:57:51.0	18.51	0.81	-	-	-	-	0.20604	0.00019	7.00	
87	01:37:37.93	−12:57:57.4	19.96	0.82	-	-	-	-	0.20841	0.00024	3.97	
88	01:37:38.32	−12:58:37.1	19.60	0.86	-	-	-10.8 ± 2.4	-	0.20808	0.00018	5.55	
89	01:37:40.04	−12:59:45.5	19.38	0.81	-	-	-8.7 ± 1.9	-	0.21078	0.00015	6.90	
90	01:37:40.09	−12:58:31.1	18.63	0.64	4.6 ± 1.8	-	-3.0 ± 1.4	27.3 ± 1.4	0.21637	0.00027	4.08	4
									0.21310	0.00060		n
91	01:37:40.27	−12:58:11.3	19.57	0.86	-	-	-5.3 ± 2.4	-	0.20934	0.00021	5.04	
92	01:37:40.78	−12:58:03.8	21.11	0.58	15.9 ± 5.8	-	-	11.3 ± 3.4	0.21329	0.00021	6.11	
93	01:37:41.54	−12:58:30.8	16.91	0.89	-	-	-4.0 ± 1.6	-	0.21318	0.00024	4.14	
									0.21409	0.00022		p
94	01:37:41.92	−12:58:00.9	21.49	0.86	-	-	-6.0 ± 2.9	-	0.21309	0.00036	2.80	
95	01:37:42.08	−12:55:35.5	17.96	0.75	-	1.9 ± 0.9	-3.4 ± 1.3	-	0.21612	0.00019	5.87	
96	01:37:42.30	−12:57:46.8	18.53	0.83	-	-	-6.6 ± 2.2	-	0.21585	0.00021	5.08	
97	01:37:43.03	−12:57:43.7	17.41	0.84	-	-	-6.7 ± 1.6	-	0.21392	0.00026	4.86	
									0.21371	0.00010		n
98	01:37:43.12	−12:56:43.8	17.44	0.38					star			
99	01:37:43.44	−12:59:38.1	18.52	0.86	-	-	-3.7 ± 1.4	-	0.20908	0.00017	6.69	

Object No.	RA (2000)	Dec (2000)	R	$V-R$	[O II]/Å	[O III]/Å	Hβ/Å	Hα/Å	$z_{\rm hel}$	$\sigma_{z_{\rm hel}}$	R	Notes
100	01:37:44.79	−12:59:37.7	18.87	0.85	-	-	-6.1 ± 2.5	-	0.20837	0.00018	6.03	
101	01:37:45.56	−12:57:41.4	18.94	0.81	-	-	-4.9 ± 2.0	-	0.21033	0.00021	5.27	
102	01:37:46.00	−12:56:59.6	18.07	0.52	8.6 ± 1.1	-	-	21.6 ± 2.6	0.20740	0.00035	3.08	
103	01:37:46.35	−12:56:02.7	19.38	0.69	-	-	-	2.5 ± 0.8	0.21368	0.00023	4.64	
104	01:37:46.41	−12:56:52.6	18.68	0.66	6.9 ± 2.7	-	-5.7 ± 1.9	6.9 ± 1.2	0.21265	0.00020	4.91	
105	01:37:47.71	−12:58:26.2	18.74	0.64	17.3 ± 0.8	1.0 ± 0.5	-	0.7 ± 0.3	0.21794	0.00032	2.96	5
106	01:37:48.38	−12:53:59.3	19.86	0.96	-	-	5.2 ± 2.6	-1.1 ± 0.4	0.09986	0.00053	2.15	
107	01:37:50.00	−12:56:28.6	20.61	1.22	-	-	-4.7 ± 1.9	-	0.46314	0.00028	6.46	
ABELL 223												
108	01:37:40.24	−12:51:13.1	18.77	0.75	7.4 ± 3.7	-	-5.1 ± 2.2	-	0.20641	0.00022	4.40	
109	01:37:41.58	−12:52:12.3	19.07	0.79	-	-	-3.3 ± 1.5	-	0.20952	0.00024	4.32	
									0.20810	0.00024		p
110	01:37:43.96	−12:51:02.3	19.73	0.78	-	-	-4.3 ± 1.6	-	0.27632	0.00027	4.10	
									0.27659	0.00012		p
111	01:37:44.82	−12:50:55.2	18.55	0.96	-	-	-5.9 ± 1.7	-	0.27686	0.00023	4.64	
									0.27812	0.00013		p
112	01:37:45.58	−12:52:02.2	19.67	0.75	-	-	-8.8 ± 4.1	4.8 ± 2.1	0.20647	0.00024	4.90	
113	01:37:46.12	−12:52:55.6	18.44	0.93	-	-	-5.7 ± 2.0	0.8 ± 0.4	0.27538	0.00031	3.13	
114	01:37:46.34	−12:51:48.9	19.93	0.60	-	-	-5.1 ± 1.9	12.9 ± 2.5	0.21319	0.00036	2.94	
115	01:37:48.38	−12:53:59.3	19.86	0.96	-	-	-	-3.5 ± 0.8	0.30536	0.00032	2.85	
116	01:37:48.99	−12:49:19.3	17.58	0.76	-	-	-5.1 ± 1.4	-	0.20676	0.00018	6.37	
117	01:37:49.21	−12:51:25.0	18.47	0.77	-	-	-	-	0.20437	0.00026	4.29	
118	01:37:50.27	−12:50:05.4	18.18	0.77	-	-	-4.7 ± 1.5	-	0.21334	0.00013	6.96	
119	01:37:50.32	−12:46:15.4	17.36	0.75	-	-	-3.5 ± 1.4	-	0.20132	0.00018	6.66	
120	01:37:50.71	−12:45:58.3	18.75	0.80	-	-	-4.0 ± 1.9	-	0.20875	0.00019	5.61	
121	01:37:50.78	−12:50:59.5	19.00	0.79	-	-	-7.1 ± 3.3	-	0.21195	0.00022	4.83	
									0.21261	0.00033		p
122	01:37:52.00	−12:45:36.9	18.47	0.74	-	-	-7.1 ± 2.1	-	0.20875	0.00018	6.38	
123	01:37:52.15	−12:48:25.8	20.84	0.54	5.8 ± 1.2	-	-	45.0 ± 8.3	0.20737	0.00032	3.30	
124	01:37:52.41	−12:47:21.3	19.60	0.75	-	-	-4.3 ± 2.0	-2.3 ± 0.9	0.21441	0.00020	5.30	

125	01:37:52.50	−12:48:53.5	18.09	0.75	-	-	-	-	0.20104	0.00018	6.26	
126	01:37:52.92	−12:50:13.5	18.71	0.76	-	-	-7.0 ± 2.6	-	0.20979	0.00023	5.37	
127	01:37:53.30	−12:51:18.3	19.38	0.88	-	-	-5.6 ± 2.1	1.9 ± 0.4	0.28012	0.00019	5.43	
128	01:37:53.36	−12:49:43.9	19.89	0.65	-	-	-8.8 ± 2.1	3.3 ± 1.6	0.20837	0.00025	3.25	
129	01:37:53.62	−12:44:38.3	17.34	0.99					star			
130	01:37:54.33	−12:49:15.5	18.96	0.78	-	-	-7.2 ± 2.8	-	0.20761	0.00019	5.43	
131	01:37:54.39	−12:50:25.0	19.30	0.72	-	-	-	-	0.20291	0.00017	5.70	
132	01:37:54.81	−12:47:09.6	19.04	0.67	-	-	-5.6 ± 1.3	9.5 ± 3.0	0.20748	0.00032	3.43	
133	01:37:54.89	−12:49:53.2	18.47	0.72	-	-	-	-	0.21009	0.00023	4.62	
									0.21106	0.00026		p
134	01:37:55.27	−12:51:29.5	18.70	0.76	-	-	-4.9 ± 1.4	-	0.20984	0.00025	4.39	
									0.21081	0.00014		p
135	01:37:55.45	−12:49:15.2	19.15	0.80	-	-	-6.2 ± 3.2	-	0.20880	0.00019	5.43	
136	01:37:55.53	−12:51:13.2	19.14	0.78	-	-	-5.6 ± 2.1	-	0.20610	0.00023	5.04	
137	01:37:55.57	−12:49:27.9	18.25	0.77	-	-	-7.7 ± 2.0	-	0.20500	0.00020	5.90	
138	01:37:55.68	−12:44:30.2	18.75	0.75	-	-	-8.6 ± 2.0	-	0.20678	0.00014	8.16	
139	01:37:55.90	−12:43:07.7	18.66	0.80	-	-	-7.2 ± 2.1	-	0.20175	0.00024	4.68	
140	01:37:56.02	−12:49:09.8	17.12	0.84	-	-	-6.7 ± 1.9	-	0.21050	0.00028	4.34	
									0.21253	0.00030		p
141	01:37:56.06	−12:43:23.7	20.13	0.67	17.2 ± 5.5	-	-7.5 ± 1.8	6.7 ± 2.1	0.28680	0.00034	3.17	
142	01:37:56.08	−12:48:37.8	18.93	0.72	5.5 ± 1.7	-	-	6.3 ± 1.8	0.31892	0.00031	3.42	
143	01:37:56.16	−12:48:15.4	17.61	0.82	-	-	-7.7 ± 2.3	-3.9 ± 0.9	0.21032	0.00025	4.95	
									0.20941	0.00040		n
144	01:37:56.76	−12:50:18.2	21.28	0.63	17.6 ± 1.4	3.7 ± 0.3	1.6 ± 0.7	32.1 ± 3.0	0.20765	0.00026	4.67	6
145	01:37:56.83	−12:47:43.3	18.12	0.80	-	-	-5.6 ± 1.7	-	0.21468	0.00020	6.26	
146	01:37:56.97	−12:48:18.0	19.12	0.79	-	-	-	-	0.21211	0.00023	5.21	
147	01:37:57.07	−12:49:19.9	18.99	0.83	-	-	-7.2 ± 1.7	-	0.21007	0.00022	5.73	
148	01:37:57.10	−12:46:12.9	19.85	0.69	-	-	-	-	0.20201	0.00019	5.09	
149	01:37:57.22	−12:50:17.1	17.40	0.68	36.9 ± 3.4	15.8 ± 0.8	-	14.0 ± 2.4	0.20707	0.00019	6.67	7
									0.20839	0.00004		p

Object No.	RA (2000)	Dec (2000)	R	$V-R$	[O II]/Å	[O III]/Å	Hβ/Å	Hα/Å	$z_{\rm hel}$	$\sigma_{z_{\rm hel}}$	R	Notes
150	01:37:57.23	−12:48:49.7	18.00	0.42	14.8 ± 3.9	6.0 ± 0.6	-	-	0.13734	0.00022	4.04	8
									0.20800	0.00167		s
151	01:37:57.28	−12:49:16.9	19.86	0.49	25.6 ± 3.5	4.2 ± 1.1	4.3 ± 2.0	36.1 ± 3.3	0.20701	0.00025	5.92	9
152	01:37:57.39	−12:44:46.4	19.65	0.75	-	-	-	-	0.20635	0.00015	5.91	
153	01:37:57.61	−12:43:44.2	18.85	0.74	-	-	-7.9 ± 1.5	-	0.20640	0.00017	6.34	
154	01:37:57.74	−12:47:55.8	17.41	0.83	-	-	-7.7 ± 1.7	-	0.21045	0.00025	4.82	
									0.20971	0.00040		n
155	01:37:57.77	−12:44:56.7	19.66	0.71	-	-	-3.7 ± 1.5	-	0.21268	0.00016	6.54	
					-	-	-4.0 ± 1.7	-	0.21310	0.00020	5.10	
156	01:37:57.79	−12:46:50.0	20.21	0.73	-	-	-5.9 ± 2.9	-	0.20204	0.00019	4.46	
157	01:37:58.20	−12:49:42.2	18.75	0.78	-	-	-3.3 ± 1.3	-	0.20731	0.00019	5.09	
158	01:37:58.34	−12:49:20.7	17.71	0.61	-	1.4 ± 0.7	-6.3 ± 1.3	-2.4 ± 0.6	0.13772	0.00025	4.09	
									0.13920	0.00030		n
159	01:37:58.49	−12:43:49.8	19.61	0.75	-	-	-	-4.7 ± 2.1	0.21135	0.00024	4.54	
160	01:37:58.95	−12:49:27.9	19.79	0.78	-	-	-6.1 ± 2.8	-	0.21194	0.00019	5.12	
161	01:37:59.47	−12:47:56.1	19.33	0.79	-	-	-8.8 ± 2.9	-	0.20953	0.00024	4.32	
162	01:37:59.72	−12:47:25.6	20.43	0.35	69.0 ± 7.5	37.3 ± 2.0	10.5 ± 3.4	68.1 ± 5.0	0.13823	0.00028	4.23	
163	01:37:59.84	−12:46:58.7	20.15	0.70	-	-	-	7.2 ± 3.4	0.21168	0.00026	3.28	
164	01:38:0.48	−12:47:19.5	19.71	0.76					star			
165	01:38:00.73	−12:43:15.3	18.06	0.94	-	-	-5.1 ± 2.1	-3.5 ± 0.8	0.28558	0.00024	5.12	
166	01:38:00.74	−12:44:03.2	18.28	0.77	-	-	-4.4 ± 1.5	-	0.20082	0.00017	6.54	
167	01:38:01.02	−12:46:51.6	17.00	0.79	-	-	-4.6 ± 1.6	-	0.21118	0.00024	5.14	
168	01:38:01.17	−12:46:33.6	17.87	0.82	-	-	-3.8 ± 1.8	-	0.20737	0.00019	5.23	
169	01:38:01.37	−12:46:13.4	16.85	-0.33					star			
170	01:38:01.71	−12:45:23.2	18.32	0.76	-	-	-	-	0.19857	0.00021	4.83	
171	01:38:01.87	−12:45:11.8	18.38	0.80	-	-	-7.1 ± 1.7	-	0.20148	0.00024	4.52	
172	01:38:02.19	−12:45:41.1	17.34	0.91	-	-	-7.3 ± 1.7	-0.8 ± 0.3	0.24074	0.00023	5.68	
173	01:38:02.30	−12:45:19.5	16.58	0.83	4.6 ± 1.9	3.2 ± 2.0	-3.5 ± 1.6	-	0.20427	0.00025	4.55	10
									0.20525	0.00013		p
									0.20506	0.00031		p
									0.20600	0.00167		s
174	01:38:02.40	−12:44:14.2	18.36	0.80	-	-	-3.5 ± 1.4	-	0.20996	0.00017	6.54	

175	01:38:02.49	−12:42:54.9	19.73	1.06	-	-	-8.5 ± 2.7	-	0.28755	0.00021	6.29	
176	01:38:02.59	−12:48:35.5	20.07	0.77	-	-	-	-	0.20880	0.00028	3.75	
177	01:38:02.64	−12:45:50.5	20.11	0.71	11.5 ± 5.3	-	-	14.9 ± 3.1	0.21219	0.00019	5.54	
178	01:38:02.72	−12:47:56.8	19.32	0.58	22.9 ± 3.9	8.4 ± 2.6	-	37.0 ± 2.4	0.21288	0.00026	4.07	11
179	01:38:02.73	−12:46:46.2	19.81	0.57	8.5 ± 2.4	-	-	18.0 ± 5.4	0.20434	0.00033	3.01	
180	01:38:02.88	−12:45:30.3	18.31	0.82	-	-	-3.3 ± 1.3	-	0.20785	0.00017	6.36	
181	01:38:03.01	−12:45:14.2	18.78	0.80	-	-	-4.0 ± 1.2	-	0.20153	0.00022	4.70	
182	01:38:03.10	−12:46:52.4	19.15	0.72	-	-	-5.7 ± 1.9	-	0.20341	0.00024	4.38	
183	01:38:03.31	−12:47:11.7	21.32	0.79	-	2.4 ± 1.1	-	-	0.21960	0.00089	2.08	
184	01:38:03.42	−12:44:35.8	18.83	0.84	-	-	-8.3 ± 1.7	-	0.20518	0.00023	5.08	
185	01:38:03.74	−12:46:39.1	19.87	0.74	-	-	-6.5 ± 2.3	-	0.20216	0.00021	5.00	
186	01:38:04.83	−12:47:34.0	16.88	0.83	-	-	-4.7 ± 2.1	-	0.20972	0.00025	5.07	
187	01:38:05.04	−12:48:02.6	18.78	0.87					star			
188	01:38:05.39	−12:45:35.5	17.97	0.82	-	-	-3.5 ± 1.7	-	0.20697	0.00022	4.75	
189	01:38:05.73	−12:45:23.3	17.77	0.78	-	-	-3.1 ± 1.3	-	0.20261	0.00021	5.30	
190	01:38:06.39	−12:44:02.4	17.50	0.68	12.4 ± 1.1	2.8 ± 1.4	-	13.8 ± 1.4	0.24284	0.00033	3.69	10
191	01:38:06.95	−12:43:54.7	19.18	0.53					star			
192	01:38:07.09	−12:44:41.6	19.09	0.85	-	-	-6.2 ± 2.0	-	0.20576	0.00020	5.39	
193	01:38:07.25	−12:48:13.0	17.36	0.87	-	-	-4.4 ± 1.5	-	0.20957	0.00028	4.44	
194	01:38:09.08	−12:45:38.6	19.35	0.83	-	-	-	-	0.20453	0.00031	2.98	
195	01:38:09.72	−12:44:13.5	19.17	0.82	-	-	-	-	0.20553	0.00023	4.87	
196	01:38:14.62	−12:44:29.2	18.40	0.96	-	-	-6.8 ± 2.2	-1.0 ± 0.5	0.24255	0.00025	4.81	
197	01:38:14.89	−12:45:19.1	18.44	0.89	-	-	-6.0 ± 1.8	-	0.21551	0.00025	4.35	
198	01:38:15.49	−12:43:38.4	17.48	0.80	-	-	-5.2 ± 1.2	3.9 ± 0.9	0.21560	0.00023	4.69	
199	01:38:16.67	−12:42:56.5	20.05	0.60	16.9 ± 4.4	-	6.4 ± 1.8	41.5 ± 2.8	0.24180	0.00034	2.96	13

Object No.	RA (2000)	Dec (2000)	R	$V-R$	[O II]/Å	[O III]/Å	Hβ/Å	Hα/Å	$z_{\rm hel}$	$\sigma_{z_{\rm hel}}$	R	Notes
200	01:38:17.10	−12:44:35.4	18.94	0.88	-	-	-6.0 ± 1.7	-1.7 ± 0.4	0.24365	0.00022	4.61	
201	01:38:17.76	−12:42:29.8	20.20	0.83	-	-	-6.8 ± 2.0	-	0.20598	0.00037	2.69	
202	01:38:20.81	−12:44:46.2	19.82	1.61	-	-	-5.2 ± 1.8	-	0.49693	0.00024	4.57	

Bibliography

Abell, G. O. 1958, ApJS, 3, 211

Bartelmann, M. 1995, A&A, 303, 643

Bartelmann, M. & Schneider, P. 2001, Physics Report, 340, 291

Bautz, L. P. & Morgan, W. W. 1970, ApJ, 162, L149

Bertin, E. & Arnouts, S. 1996, A&AS, 117, 393

Blandford, R. D., Saust, A. B., Brainerd, T. G., & Villumsen, J. V. 1991, MNRAS, 251, 600

Bond, H., Kofman, L., & Pogosyan, D. 1996, Nature, 380, 603

Bonnet, H. & Mellier, Y. 1995, A&A, 303, 331

Cardelli, J. A., Clayton, G. C., & Mathis, J. S. 1989, ApJ, 345, 245

Carlberg, R. G., Yee, H. K. C., Ellingson, E., et al. 1996, ApJ, 462, 32

Clowe, D., Luppino, G. A., Kaiser, N., Henry, J. P., & Gioia, I. M. 1998, ApJ, 497, L61

Clowe, D. & Schneider, P. 2001, A&A, 379, 384

Czoske, O., Kneib, J.-P., Soucail, G., et al. 2001, A&A, 372, 391

David, L. P., Forman, W., & Jones, C. 1999, ApJ, 519, 533

Dietrich, J. P., Clowe, D. I., & Soucail, G. 2002, in preparation

Dressler, A. 1978, ApJ, 226, 55

Dressler, A. & Shectman, S. A. 1988, AJ, 95, 985

Dyson, F., Eddington, A., & Davidson, C. 1920, Mem. R. Astron. Soc., 62, 291

Folkes, S., Ronen, S., Price, I., et al. 1999, MNRAS, 308, 459

Fukugita, M., Shimasaku, K., & Ichikawa, T. 1995, PASP, 107, 945

Gray, M. E., Taylor, A. N., Meisenheimer, K., et al. 2002, ApJ, 568, 141

Gunn, J. E. & Stryker, L. L. 1983, ApJS, 52, 121

Harrison, E. R. 1974, ApJ, 191, L51

Hartigan, J. A. & Hartigan, P. M. 1985, Annals of Statistics, 13, 70

Hartigan, P. M. 1985, Applied Statistics, 34, 320

Hoekstra, H., Franx, M., Kuijken, K., & Squires, G. 1998, ApJ, 504, 636

Hradecky, V., Jones, C., Donnelly, R. H., et al. 2000, ApJ, 543, 521

Jain, B., Seljak, U., & White, S. 2000, ApJ, 530, 547

Jenkins, A., Frenk, C. S., Pearce, F. R., et al. 1998, ApJ, 499, 20

Kaiser, N. 1995, ApJ, 439, L1

Kaiser, N. & Squires, G. 1993, ApJ, 404, 441

Kaiser, N., Squires, G., & Broadhurst, T. 1995, ApJ, 449, 460

Kaiser, N., Wilson, G., Luppino, G., et al. 1998, astro-ph/9809268

Kashikawa, N., Shimasaku, K., Yagi, M., et al. 1995, ApJ, 452, L99

Kauffmann, G., Colberg, J. M., Diaferio, A., & White, S. D. M. 1999, MNRAS, 303, 188

Keeton, C. R. & Kochanek, C. S. 1998, ApJ, 495, 157

Kennicutt, R. C. 1998, ARA&A, 36, 189

Kurtz, M. J. & Mink, D. J. 1998, PASP, 110, 934

Landolt, A. U. 1992, AJ, 104, 340

Lombardi, M., Schneider, P., & Morales-Merino, C. 2002, A&A, 382, 769

Möller, P. & Fynbo, J. U. 2001, A&A, 372, L57

Monet, D., Bird A., Canzian, B., et al. 1998, The USNO-A2.0 Catalogue (U.S. Naval Observatory, Washington DC)

Newberry, M. V., Kirshner, R. P., & Boroson, T. A. 1988, ApJ, 335, 629

Peacock, J. A. 1999, Cosmological physics (Cosmological physics. Publisher: Cambridge, UK: Cambridge University Press, 1999. ISBN: 0521422701)

Pisani, A. 1993, MNRAS, 265, 706

—. 1996, MNRAS, 278, 697

Pogosyan, D., Bond, J. R., Kofman, L., & Wadsley, J. 1998, in Wide Field Surveys in Cosmology, 14th IAP meeting held May 26-30, 1998, Paris. Publisher: Editions Frontieres. ISBN: 2-8 6332-241-9, p. 61., 61

Press, W. H., Teukolsky, S. A., Vetterling, W. T., & Flannery, B. P. 1992a, Numerical recipes in C. The art of scientific computing (Cambridge: University Press, 2nd ed.)

—. 1992b, Numerical recipes in FORTRAN. The art of scientific computing (Cambridge: University Press, 2nd ed.)

Proust, D., Cuevas, H., Capelato, H. V., et al. 2000, A&A, 355, 443

Sandage, A., Kristian, J., & Westphal, J. A. 1976, ApJ, 205, 688

Schechter, P. 1976, ApJ, 203, 297

Schlegel, D. J., Finkbeiner, D. P., & Davis, M. 1998, ApJ, 500, 525

Schneider, P. 1995, A&A, 302, 639

Schneider, P. & Bartelmann, M. 1997, MNRAS, 286, 696

Schneider, P., Ehlers, J. ., & Falco, E. E. 1992, Gravitational Lenses (Gravitational Lenses, XIV, 560 pp. 112 figs.. Springer-Verlag Berlin Heidelberg New York. Also Astronomy and Astrophysics Library)

Schneider, P., van Waerbeke, L., Jain, B., & Kruse, G. 1998, MNRAS, 296, 873

Seitz, C. & Schneider, P. 1995, A&A, 297, 287

—. 1997, A&A, 318, 687

Seitz, S. & Schneider, P. 1996, A&A, 305, 383

—. 2001, A&A, 374, 740

Smail, I., Ellis, R. S., Fitchett, M. J., & Edge, A. C. 1995, MNRAS, 273, 277

Smail, I., Ellis, R. S., Fitchett, M. J., et al. 1991, MNRAS, 252, 19

Squires, G. & Kaiser, N. 1996, ApJ, 473, 65

Tonry, J. & Davis, M. 1979, AJ, 84, 1511

Tully, R. B. & Shaya, E. J. 1998, astro-ph/9810298

Tustin, A. W., Geller, M. J., Kenyon, S. J., & Diaferio, A. 2001, AJ, 122, 1289

van Waerbeke, L. 2000, MNRAS, 313, 524

Vogeley, M. S., Park, C., Geller, M. J., Huchra, J. P., & Gott, J. R. I. 1994, ApJ, 420, 525

Walsh, D., Carswell, R. F., & Weymann, R. J. 1979, Nature, 279, 381

Wang, Q. D. & Ulmer, M. P. 1997, MNRAS, 292, 920

Wu, X., Xue, Y., & Fang, L. 1999, ApJ, 524, 22

Acknowledgment

A work like this cannot be done without the help of many people. I would like to thank Peter Schneider who offered this thesis topic to me. His door was always open to help me and answer my questions. I have to thank him especially for many helpful comments on the draft version of this thesis.

Douglas Clowe supervised the observational part of this thesis, he reduced the WFI frames, produced the catalogs for the weak lensing analysis, and provided help and many answers concerning not only image reduction and `IMCAT`.

Lindsay King was always there to answer my countless questions when Peter or Doug were not around. I have to thank her especially for her moral and nutritive support in the stressful final phase.

I thank my collaborators Emilio Romano–Díaz for providing the simulation data and his unbreakable enthusiasm when I requested another simulation with "a stronger filament and the clusters closer together", and Geneviève Soucail for the fruitful and instructive discussions during my stay in Toulouse.

I would like to thank Martin Altmann for introducing me to the mysteries IRAF, Martina Kleinheinrich and later also Martin Kilbinger for being such nice roommates and all the tea, Joan–Marc Miralles for many interesting discussions during lunchtime.

Everybody else in the lensing group and the Sternwarte be thanked for creating a unique atmosphere.

Nils Benter, Richard Willmann, Matthias Frink, and Lucas Platter have been my friends all through my studies. Thanks for the wonderful time we had together and the help that was provided by all of them.

I have to thank my parents for their support of my interest in astronomy over many, many years, and of course for the financial support during my studies.

Last, but not least I wish to thank Stefanie for her continuous attempts to keep me from working at least on the weekends, and her patience and understanding when she was not successful.
Thank you!

This work was supported by the TMR Network "Gravitational Lensing: New Constraints on Cosmology and the Distribution of Dark Matter" of the EC under contract No. ERBFMRX-CT97-0172.

And it shall be,
when thou hast made an end of reading this book,
that thou shalt bind a stone to it,
and cast it into the midst of Euphrates.

Jer. 51, 63